Effect of precipitation and winds on sea surface elevation and storm surges

PHD THESIS

Benjamin Wong

Imperial College London

Department of Physics

Space and Atmospheric Physics Group

Thesis submitted for the degree of
Doctor of Philosophy of Imperial College London

December 2015

Supervisor:

Professor Ralf Toumi

Examiners:

Professor Kevin Horsburgh

Dr. Helen Brindley

Statement of originality

I declare that this thesis is my own work, except where work by others has been properly referenced.

Publications

The research presented in this thesis has been submitted for publication:

Wong, B. and R. Toumi, 2015: Model study of the asymmetry in tropical cyclone-induced positive and negative surges, submitted to Atmospheric Science Letters.

Wong, B. and R. Toumi, 2015: Effect of extreme ocean precipitation on sea surface elevation and storm surges, submitted to Quarterly Journal of the Royal Meteorological Society.

Copyright

The copyright of this thesis rests with the author and is made available under a Creative Commons Attribution Non-Commercial No Derivatives licence. Researchers are free to copy, distribute or transmit the thesis on the condition that they attribute it, that they do not use it for commercial purposes and that they do not alter, transform or build upon it. For any reuse or redistribution, researchers must make clear to others the licence terms of this work.

Abstract

Ocean circulation and storm surge models have neglected mass contributions from precipitation and can have a systematic bias in sea surface height (SSH). Here, a new rainfall scheme has been set up in the ocean circulation model Regional Ocean Modelling System (ROMS) to incorporate the effects of precipitation mass. When precipitation is added to the sea surface, it spreads out via surface gravity waves that increase in propagation speed with increasing water depth. Over several days, the increase in SSH due to the precipitation mass added created a geostrophic adjustment, generating clockwise-rotating geostrophic currents around the SSH increase. The transfer of momentum from precipitation to the sea surface, or rain stress, is investigated in ROMS. An error in the existing implementation of rain stress has been uncovered and corrected. The existing ROMS code generated an error in the direction of rain stress by up to 45° and systematically overestimated its magnitude by 41%.

The SSH response to wind stress is examined. Positive and negative surges are generally generated by onshore and offshore winds respectively. While positive surges are widely studied, negative surges are less well understood. Negative surges are larger in magnitude and extend further across the coastline than positive surges. It is shown for the first time that the alongshore component of the wind stress is the main contributor to the asymmetrical surge response. Without this component, the ratio of negative to positive surge can decrease by more than half. This asymmetry also increases with increasing latitude and decreasing depth.

In the case study of a real tropical cyclone, Monica, the effect of incorporating precipitation mass is compared with other processes affecting storm surge: surface wind, inverse barometer effect and rain stress. The maximum SSH response is 170.6 cm for the wind effect, 61.5 cm for the inverse barometer effect, 7.5 cm for the effect of rain stress and 6.4 cm for the effect of rain mass. Each process has been shown to have different spatial influences. The effect of rain mass has a strong remote influence compared to the inverse barometer effect and the effect of rain stress. This is particularly seen in semi-enclosed bays.

Contents

Contents 9

List of Figures 12

List of Tables 17

Acronyms 18

1 Introduction 21

1.1 Background 21

1.2 Storm surges generated by tropical cyclones 25

1.2.1 Bay of Bengal 25

1.2.2 Gulf of Mexico 26

1.2.3 Southwest Pacific 27

1.3 Storm surges generated by extratropical cyclones 28

1.3.1 North Sea 28

1.3.2 Southwest Atlantic 29

1.4 Processes contributing to storm surges 31

1.4.1 Wind stress 31

1.4.2 Pressure effect 36

1.4.3 Surface wave effect 38
1.4.4 Rain mass 39
1.4.5 Rain stress 41
1.5 Thesis plan 45
2 Model description 47
2.1 COAWST model 47
2.2 ROMS model 47
2.2.1 Set-up of the new rainfall scheme in ROMS to introduce rain mass 53
2.2.2 Set-up of the idealized ocean model 57
2.2.3 Set-up of the real-case ocean model 59
2.3 WRF model 61
2.3.1 Set-up of the idealized cyclone model 64
2.3.2 Set-up of the real-case atmosphere model 66
3 The effect of precipitation mass and momentum 69
3.1 Introduction 69
3.2 Short term response to rain mass 70
3.3 Longer term response to rain mass 71
3.4 Impact of rain mass on temperature and salinity 78
3.5 Corrections to ROMS' implementation of rain stress 82
3.6 Point source response to rain stress 83
3.7 Effect of rain stress on storm surges 85

3.8 Discussion 86

3.9 Conclusion 93

4 Asymmetry in positive and negative surges 97

4.1 Introduction 97

4.2 Results 98

4.3 Discussion 111

4.4 Conclusion 121

5 Effect of precipitation on storm surges: Cyclone Monica 123

5.1 Introduction 123

5.2 Model validation 126

5.3 Results 130

5.3.1 Wind and ocean currents 132

5.3.2 Sea surface height response 135

5.4 Discussion 138

5.5 Conclusion 148

6 Summary and final conclusions 151

7 Biblography 159

List of Figures

Figure 1.1: Ocean response to the alongshore wind stress at the coast. Extracted from *Pugh* [1987]. 33

Figure 1.2: Changes in the water level (η) in the Meghna estuary after doubling the moving speed of the cyclone. Extracted from *AsSalek* [1997]. 35

Figure 1.3: Ekman pumping driven by the rotating winds. Extracted from *Colling* [2001].... 36

Figure 1.4: Sub-tidal variations in sea level height at various locations around the Celtic Sea, compared against the atmospheric pressure at St. Mary's. Extracted from *Pugh* [1987]. 37

Figure 1.5: Relationship between surface stress and wind speed at 10 m. Extracted from *Van Dorn* [1953]..... 42

Figure 1.6: Gravity and drag forces acting on a raindrop (left) and the horizontal and vertical velocities of a raindrop (right) [*Caldwell and Elliott*, 1970]. 43

Figure 2.1: Arakawa-C grid staggering of the ROMS grid showing the horizontal velocity points (*u* and *v*) and density (ρ). 52

Figure 2.2: Vertical coordinate system of the ROMS grid showing the horizontal velocity points (*u* and *v*), vertical velocity points (*w*) and density points (ρ)..... 53

Figure 2.3: Domain of the idealized model. 58

Figure 2.4: Domain of the real-case simulation..... 59

Figure 2.5: Arakawa C-grid staggering in WRF, showing the horizontal velocity points (*U* and *V*) and temperature (θ). A portion of a nested grid with 1:3 grid size ratio is shown with the solid lines denoting coarse-grid cell boundaries and the dashed lines denoting fine-grid cell boundaries. 63

Figure 3.1: SSH response to a drop of rain on a single surface grid cell after 2 hours (left) and 9 hours (right).....71
Figure 3.2: Cumulative rainfall of the idealized tropical cyclone over 8 days. 72
Figure 3.3: SSH and sea surface current response to the rain mass added to the ocean with (a) 100 m depth and (b) 1000 m depth. The reference vector is 0.01 m s^{-1}.....73
Figure 3.4: SSH response to rain mass against latitude along the coast at 170th hour for the ocean set-up with 100 m depth. 73
Figure 3.5: u-momentum terms through the ocean depth at the point 20 °N 141 °E. 74
Figure 3.6: Surface momentum terms (vector field) superimposed onto SSH, showing (a) pressure gradient term (b) Coriolis term. The reference vector is 1 x 10^{-6} m s^{-1}. .75
Figure 3.7: Bottom momentum terms (vector field) superimposed onto SSH, showing (a) pressure gradient term (b) Coriolis term. The reference vector is 1 x 10^{-6} m s^{-1}. .76
Figure 3.8: Rain input at the 160th hour; cyclone making landfall at 140°E. 77
Figure 3.9: SSH response from introducing a single burst of rainfall at t = 160 h. Different time-frames show (left) t = 166 h and (right) t = 169 h. 77
Figure 3.10: SSH response from introducing a single burst of rainfall at t = 160 h. Different time-frames show (left) t = 166 h and (right) t = 169 h. Here, the Coriolis parameter has been set to zero. 78
Figure 3.11: SST for (a) the existing implementation with rain forcing but without rain point sources (min SST = 24.03 °C) and (b) the point source implementation of rain without rain forcing (min SST = 25.23 °C). 80
Figure 3.12: SSS for (a) the existing implementation with rain forcing but without rain point sources (min SSS = 33.15 psu) and (b) the point source implementation of rain without rain forcing (min SSS = 34.90 psu). 80

Figure 3.13: Sea surface currents superimposed onto SSH for (a) the existing implementation with rain forcing but without rain point sources (max SSH = 0.4 cm) and (b) the point source implementation of rain without rain forcing (max SSH = 5.8 cm). Different scales have been used in (a) and (b). The reference vector is 0.01 m s^{-1}. 81

Figure 3.14: Sea surface height at 10 hours after introducing a rain stress perturbation for (a) the existing implementation of rain stress in ROMS and (b) the corrected implementation of rain stress in ROMS. The black dot in the centre of the domain (20°N 150°E) denotes the initial position of perturbation. 84

Figure 3.15: Response of SSH and sea surface currents to rain stress at t = 163 h. 86

Figure 3.16: Wind direction scenarios illustrating the errors that would arise when using the existing ROMS implementation of rain stress. 92

Figure 4.1: Surface stress (N/m^2) response to the total wind stress at 105 hours. 100

Figure 4.2: Surface stress (N m^{-2}) response (at 105 hours) to only the cross-shore wind stress (left) and only the alongshore wind stress (right). The reference vector for the surface stress is in 50 N m^{-2}. 101

Figure 4.3: SSH response to (a) Case A and (b) Case B at 105 hours into the simulation. The reference vector for the sea surface currents is 1 m/s. 102

Figure 4.4: Sea surface height response to (a) Case C and to (b) Case D at 105 hours into the simulation. The reference vector for the sea surface currents is 1 m/s. 103

Figure 4.5: SSH response to (a) Case E and to (b) Case F at 105 hours into the simulation. The reference vector for the sea surface currents is 1 m/s. 104

Figure 4.6: SSH along the coastline at 140°E. (a) Plot of temporal maximum SSH against latitude (b) Plot of temporal minimum SSH against latitude. 105

Figure 4.7: Surface u-momentum stress along the coastline at 140°E (t = 106 hours). 107

Figure 4.8: Time-series of surface momentum stress at 21°N 140°E, showing the u-momentum stress (left) and v-momentum stress (right). 108

Figure 4.9: SSH response at the points 21°N 140°E (left) and 19°N 140°E (right) for the control case, forced with the total wind field (solid lines) and with only the cross-shore wind component (dashed lines). 109

Figure 4.10: SSH response at the points 21°N 140°E (left) and 19°N 140°E (right) in the control case (solid lines) and the higher latitude case (dashed lines). Both cases are forced with the complete wind field. 110

Figure 4.11: SSH response at the points 21°N 140°E (left) and 19°N 140°E (right) in the control case (solid lines) and the sloping bathymetry case (dashed lines). Both cases are forced with the complete wind field. 111

Figure 4.12: Map of Bay of Bengal showing the contours of sea surface heights generated 30 min after the storm made landfall at the Orissa coast. Extracted from *Pugh* [1987]. 113

Figure 4.13: SSH response to Case A (left) and Case B (right) at 105 hours into the simulation, with a constant Coriolis parameter corresponding to 20°N. The reference vector for the sea surface currents is 1 m/s. 116

Figure 4.14: Illustration showing how SSH is affected by the southward alongshore wind component (a) and the northward alongshore wind component (b). 119

Figure 4.15: Depth averaged momentum terms at 95 h, showing alongshore advection (left) cross-shore Coriolis term (right). 121

Figure 5.1: Map of northern Australia showing the geographical landmarks referred to in this case study (Map reproduced with permission from Geoscience Australia http://www.australia.gov.au/topics/science-and-technology/maps-and-mapping). 125

Figure 5.2: Cyclone path of WRF (solid line) and observations from BOM cyclone report (dashed line). Filled circles are positions every 24 hours from 0000 UTC 20 April 2006 (open circle). Location of the Groote Elyandt weather station is indicated with an 'X'. 127

Figure 5.3: 5-Day cumulative rainfall output from 20 April 2006 for (a) WRF and (b) TRMM. 128

Figure 5.4: Comparison between the storm surge generated in ROMS with tidal gauge measurements (detided) at Groote Elyandt weather station obtained from ABSLMP, with the location indicated with an 'X' on Figure 5.1. 130

Figure 5.5: 2-m winds from 21 April 2006 to 23 April 2006. 133

Figure 5.6: Ocean surface currents from 21 April 2006 to 23 April 2006..... 134

Figure 5.7: Bottom currents from 21 April 2006 to 23 April 2006. 135

Figure 5.8: SSH response to the effect of wind, from 21 April 2006 to 23 April 2006. 136

Figure 5.9: SSH response to the inverted barometer effect, from 21 April 2006 to 23 April 2006..... 136

Figure 5.10: Additional SSH response to the effect of rain stress, from 21 April 2006 to 23 April 2006. 137

Figure 5.11: Additional SSH response due to rain mass addition, from 21 April 2006 to 23 April 2006. 138

Figure 5.12: Bathymetry at the Gulf of Carpentaria. 139

Figure 5.13: Map of northern Australia (from Figure 5.1) showing the coastline (in red) analysed for coastal impact. 146

Figure 5.14: Comparison of the SSH change due to various physical effects, along the coastline highlighted in red in Figure 5.13. 147

List of Tables

Table 1.1: Characteristics of tropical and extratropical cyclones, with the storm surges generated [*Gönnert et al*., 2001]. 22

Table 1.2: Examples of storm surge modelling systems used and their challenges. 30

Table 2.1: Variables required in ROMS to set up a point source. 55

Table 4.1: Cases set up with different wind and ocean conditions. 99

Table 5.1: Cases set up with different wind and ROMS model options. 131

Table 5.2: SSH plots isolating different effects, obtained by differencing plots from different cases. 132

Table 5.3: Broad comparison of the error in the peak storm surge differences, associated with various parameters affecting storm surges. Parameters 1 to 7 are from the case study of Cyclone Sidr [*Lewis et al*., 2014], parameters 8 – 11 are from the case study of Cyclone Monica in Chapter 5 within this thesis. 144

Acronyms

ABSLMP	Australian Baseline Sea Level Monitoring Project
ADCIRC	ADvanced CIRCulation model
AFWA	Air Force Weather Agency
ARW	Advanced Research WRF
BOM	Bureau of Meteorology (Australia)
CFSR	Climate Forecast System Reanalysis
CH3D	Curvilinear-grid Hydrodynamics 3D model
CIMSS	Cooperative Institute for Meteorological Satellite Studies (UWM)
CMEPS	Coastal Marine Environment Prediction System (NCSU)
COARE	Coupled Ocean-Atmosphere Response Experiment
COAWST	Coupled Ocean–Atmosphere–Wave–Sediment Transport
CSTM	Community Sediment Transport Model
DTC	Developmental Testbed Center
FAA	Federal Aviation Administration
FVCOM	Finite Volume Community Ocean Model
GLS	Generic Length Scale
HAT	Highest Astronomical Height
HYCOM	HYbrid Coordinate Ocean Model
IIT	Indian Institute of Technology
MCT	Model Coupling Toolkit
MM5	Mesoscale Model 5
MMM	Mesoscale and Microscale Meteorology Division (NCAR)

MOGREPS	Met Office Global and Regional Ensemble Prediction System
MPDATA	Multidimensional Positive Definite Advection Transport Algorithm
NCAR	National Center for Atmospheric Research
NCEP	National Center for Environmental Prediction
NCL	NCAR Command Language
NCODA	Navy Coupled Data Assimilation system
NCSU	North Carolina State University
NetCDF	Network Common Data Form
NHC	National Hurricane Center
NMM	Non-hydrostatic Mesoscale Model (WRF)
NOAA	National Oceanic and Atmospheric Administration
NRL	Naval Research Laboratory
NWP	Numerical Weather Prediction
NWS	National Weather Service
OSU	Oregon State University
POM	Princeton Ocean Model
ROMS	Regional Ocean Modelling System
SCRIP	Spherical Coordinate Remapping Interpolation Package
SLOSH	Sea, Lake and Overland Surges from Hurricanes
SSH	Sea surface height
SSHWS	Saffir-Simpson Hurricane Wind Scale
SSMS	Storm Surge Modelling System
SSS	Sea surface salinity
SST	Sea surface temperature
SWAN	Simulating WAves Nearshore

TCWC	Tropical Cyclone Warning Centre
TC-LAPS	Tropical Cyclone Limited Area Prediction System
TKE	Turbulent Kinetic Energy
TRMM	Tropical Rainfall Measuring Mission
UTC	Coordinated Universal Time
UWM	University of Wisconsin-Madison
WMO	World Meteorological Organization
WRF	Weather, Research and Forecasting model

1 Introduction

1.1 Background

Tropical and extratropical cyclones (Table 1.1, [*Gönnert et al*., 2001]) are known to cause one of the most common and devastating natural disasters, leading to high fatality rates and large economic losses. With a fast growing population in the world's coastal regions, the devastation that severe storms can bring to coastal communities is becoming more pronounced [*Henderson-Sellers et al.*, 1998]. From the review of historical hurricane cases in the US by the National Hurricane Center (NHC) [*Blake et al.*, 2011], there has been 284 strikes from tropical cyclones between 1851 and 2010, of which 96 were severe storms at Category 3 and higher on the Saffir-Simpson Hurricane Wind Scale (SSHWS). This is equivalent to 1.8 hurricane strikes per year with two severe hurricanes striking every three years. The largest death tolls within this period resulted from hurricanes that produced exceptionally high storm surges. A storm surge is an abnormal rise in sea level generated during a storm and is considered over and above the level of astronomical tides. Unlike tides, storm surges are difficult to predict and can lead to catastrophic levels of destruction if coastal communities are unprepared. The same review also emphasized that future loss of lives is inevitable unless coastal communities begin to understand the impacts of storm surges. Hurricane Katrina is a model example of the devastation and damage that storm surges can cause [*Dodla et al.*, 2011]. In 2005, Katrina led to an estimated death toll of 1200, with many deaths resulting from storm surges. When Katrina made landfall in Florida, a surge height of about 10 m was generated along the Mississippi coastline [*Fritz et al.*, 2007]. Inundation resulting from the storm surge caused severe damage to the coastal infrastructure along the Mississippi, Louisiana and Alabama coastlines [*Robertson et al.*, 2007]. Areas in

the vicinity of the storm experienced surge heights ranging from 2.2 m (west of Lake Pontchartrain) to 4.9 m (St. Bernard) [*van Heerden et al.*, 2007]. Katrina became the costliest hurricane in the United States to date, estimated at a damage cost of US$105 billion (adjusted to 2010 US dollars) [*Blake et al.*, 2011].

Parameter	**Tropical cyclones**	**Extratropical cyclones**
Spatial scale of storm	500 ± 200 km	1000 ± 500 km
Storm geometry	Compact and nearly symmetrical	Sprawling geometry
Surge amplitude	Larger: Hurricane Camille (1969) generated a surge of 7.5 m	Smaller: Surges of 5 m are infrequent
Surge duration	Several hours to half a day	2 – 5 days
Length of coastline affected by the surge	< 200 km	Several hundred kilometres

Table 1.1: Characteristics of tropical and extratropical cyclones, with the storm surges generated [*Gönnert et al*., 2001].

Compared to tropical cyclones, extratropical cyclones have a larger spatial extent but the magnitude of storm surges generated are smaller. The North Sea flood in 2007 [*Parker and Foden*, 2009] was predicted to generate the largest storm surge in the east coast of England since 1953, with a combination of strong winds and high tides forecasted. The storm was referred to Cyclone Tilo in the UK and was expected to affect the coastlines of UK, Norway, Netherlands, Germany, Denmark and Belgium. The east coast of England had been prone to floods historically, owing to the shallow nature of the North Sea and the geometry of The Wash (between Norfolk and Lincolnshire) forming a semi-enclosed funnel [*Baxter*, 2005].

The Environment Agency was alerted after the Met Office forecasted wind speeds of up to 28 m/s and surges of up to 3 m in the East Anglia and Thames Estuary area, 50 – 90 cm above the alert levels set by the Environment Agency. However during the actual event, the winds were largely offshore, resulting in wave heights that were lower than expected. The actual storm surge was 20 – 30 cm lower than the predicted values. The highest sea level was observed at Lowestoft, at 71 cm above the alert level. The highest sea level recorded in and around Great Yarmouth was just 10 cm from overtopping the sea walls. Overall there were no casualties, but there were some damages to properties reported (http://www.metoffice.gov.uk/about-us/who/how/case-studies/floods-2007).

Despite having a small margin of error in the prediction of storm surges, many storm surge models only incorporate two primary effects that contribute to storm surges, namely wind and atmospheric pressure [*Pugh*, 1987]. Other effects such as sea surface waves and precipitation are often neglected [*Harris*, 1963]. While there are several studies on the effect of waves on storm surges (e.g. *Brown* [2010] and *Mastenbroek et al.* [1993]), research on the contribution of rainfall to storm surges is sparse. Rainfall can contribute to storm surges through its mass and momentum, but these effects are implicitly thought to be negligible. For highly precipitating storm systems such as tropical and extratropical cyclones, the contribution of rain mass may be substantial. For instance, Typhoon Morakot holds the record for the highest rainfall produced, reported to be up to 74 cm/day [*Wu*, 2013]. This is potentially adding up to 74 cm/day of freshwater to the ocean, which can potentially increase the storm surge levels substantially. The transfer of momentum from raindrops to the sea surface, also referred to as rain stress, is another under-studied process. Although the effect of rain stress is incorporated into many ocean circulation models (e.g. ROMS), its isolated effect and contribution to storm surges is not known.

In Sections 1.2 and 1.3, the international landscape of storm surge modelling and forecasting is reviewed to highlight the key challenges faced by various storm surge modelling systems. The models and methodologies used internationally is highly diverse, employing different approaches and varying levels of physics representation. For example, the deterministic approach employs a scenario based on a single set of environmental conditions to simulate the storm surge at a region. However, small changes in the storm characteristics and environmental conditions can have huge impacts to the predicted storm surge. The probabilistic approach produces ensemble runs using historical statistics where storm surge data is generated and tied to a probability of occurrence [*Tablazon et al.*, 2015]. The composite approach simulates tens of thousands of hypothetical storms to generate potential storm surge data for assessment [*Zachry et al.*, 2015]. Different models also vary in levels of complexity, incorporating different levels of physics representation. Section 1.4 then provides a background of the different effects mentioned in these studies that can contribute to storm surges, namely wind, atmospheric pressure, waves and precipitation.

This thesis addresses the gap in existing ocean circulation and storm surge models where the contributions of precipitation to storm surges are ignored. This has direct impact to many storm surge prediction approaches since ocean circulation and storm surge models are often the basic tools used. In order to investigate and understand the isolated effects of rain mass and rain stress, an idealized model is set up using the Weather, Research and Forecasting (WRF) model and ROMS. The contribution of rain mass and rain stress to storm surges is first examined in different idealized set-ups. The effect of rain is then quantified and compared with established processes, namely the wind-driven effect and pressure-driven effect in a real case study. Cyclone Monica [*Durden*, 2010] has been chosen as a case study

here for her high wind speed, low system pressure and high rainfall, which are the key storm surge effects investigated here.

1.2 Storm surges generated by tropical cyclones

1.2.1 Bay of Bengal

The Bay of Bengal is one the regions in the world most affected by storm surges. In November 1970, 300 000 people were killed in one of the most severe tropical storms in Bangladesh and about 140 000 lives were lost in the Chittagong cyclone of April 1991 [*Murty et al*., 1986]. There has since been much success in providing storm surge warnings using the surge model from the Indian Institute of Technology (IIT). *Dube et al*. [1997] provided numerous successful case studies using the surge model. In the study of the Andhra cyclone (1977), the simulated peak surge of 5 m at a grid cell near Divi Island was in agreement with the observed sea level of about 5 m in the same region. For the Orissa cyclone in 1982, the modelled peak surge and its location was also consistent with the observed peak sea level elevation of 3 m at Dharma port. Several shortfalls of the storm surge modelling system were also mentioned. Firstly, it was often uncertain if the cyclone models used would provide accurate estimates of the cyclone wind field, which was essential in forcing the surge model. Secondly, there were significant uncertainties in the input data required by the ocean model such as bathymetry, coastal geometry, inshore current and tidal data. Lastly, it was noted that hydrological processes (such as rivers and rainfall) might have significant contributions to storm surges but were not incorporated into the existing model. Only preliminary work from river-ocean coupled models had since been carried out, showing that fresh water from rivers could modify the storm surge [*Dube et al*., 1986].

1.2.2 Gulf of Mexico

There are two main storm surge models used operationally in the United States: Sea, Lake and Overland Surges from Hurricanes (SLOSH) [*Jarvinen and Lawrence*, 1985] and ADvanced CIRCulation model (ADCIRC) [*Westerink et al.*, 1992]. SLOSH is a widely-used storm surge model developed by the US National Weather Service (NWS) and is run by the NHC to deliver storm surges forecasts (http://www.nhc.noaa.gov/surge/slosh.php). The model is capable of evaluating inland flooding and overtopping of barrier systems, levees and roads. It can also estimate storm surges based on historical, hypothetical and predicted hurricanes. The strength of the model lies in it being computationally efficient and ideal for operational needs. However, the grid resolution used in SLOSH is often too coarse to resolve small features. Being a regional model, SLOSH also has a limited accuracy in specifying open boundaries. ADCIRC is a hydrodynamic circulation model jointly developed by several institutions, including University of North Carolina and University of Notre Dame. It can be run in 2D or 3D, both solving the depth-integrated continuity equation. ADCIRC has been widely used in the prediction of storm surge and floods, modelling of tides, wind-driven circulation, larval transport, near-shore marine operations and studies in dredging and material disposal. The effect of waves and hydrology have been noted to be absent in both models.

Lin et al. [2010] conducted a risk assessment on the hurricane storm surge in New York City using both SLOSH and ADCIRC. ADCIRC was based on an unstructured grid the resolution of the grid could be refined from 70 km to 10 m in this case. SLOSH was based on a structured grid and there is limited capability to perform grid refinement (actual grid resolution not specified). With a simplified physics representation and a relatively coarse grid, 7555 synthetic tracks were simulated with SLOSH in two days on a regular computer.

The computational time required by ADCIRC was much longer, with a more comprehensive physics representation and a finer grid resolution compared to SLOSH. As a result, only 9 out of the 7555 cases simulated by SLOSH (with the highest storm surge) were evaluated by ADCIRC. Most of the maximum surges predicted were in agreement between the two models. However, one of the SLOSH cases predicted the maximum surge to be 1 m lower than ADCIRC at an inlet to the south of New Jersey. The coarse resolution of the SLOSH grid was likely to be the reason since small features such as bays and inlets were less well-resolved.

1.2.3 Southwest Pacific

The operational storm surge modelling system in Northern Australia is based on the SEAtide model [*Harper et al*., 1978] and has been in use since 2004. This system empirically predicts the magnitude, location and duration of storm surges by simulating many runs using a range of cyclone intensity, size, speed and track. However, using permutations of different cyclone parameters to create different hypothetical cyclone scenarios can inevitably generate unrealistic scenarios. One of the challenges faced in using this system is the difficulty in constraining these cyclone scenarios to a realistic range. [*Horsburgh et al.* 2011]

In Western Australia, the Perth Tropical Cyclone Warning Centre (TCWC) uses a surge model based on *Hubbert et al.* [1990]. The surge model is a depth-integrated ocean model that simulates sea surface currents and elevation. It includes the non-linear advective terms and the equations of motion are solved using a split-explicit finite difference scheme. The surge model is forced using the cyclone parameters predicted by the Tropical Cyclone Limited Area Prediction System (TC-LAPS) [*Davidson and Weber*, 2000]. *Horsburgh et al.* [2011] described the application of this system in the case of Tropical Cyclone Chris (2002).

The cyclone pressure was initially under-predicted by about 28 hPa. Using the Dvorak technique [*Dvorak,* 1984], it was found that the under-prediction in pressure resulted from an under-prediction of the winds by a factor of 1.25. This was corrected in the surge model and a maximum surge of 3.4 m was predicted, which was in good comparison with observations of 3 - 3.5 m in the same area.

1.3 Storm surges generated by extratropical cyclones

1.3.1 North Sea

The North Sea flood in 2007 [*Parker and Foden*, 2009] was predicted to generate the largest storm surge in the east coast of England since 1953, with a combination of strong winds and high tides forecasted. The storm was referred to Cyclone Tilo in the UK and was expected to affect the coastlines of UK, Norway, Netherlands, Germany, Denmark and Belgium. The Environment Agency was alerted after the Met Office forecasted wind speeds of up to 28 m/s and surges of up to 3 m in the East Anglia and Thames Estuary area, 50 – 90 cm above the alert levels set by the Environment Agency. However during the actual event, the winds were largely offshore and resulted in wave heights that were lower than expected. The actual storm surge was 20 – 30 cm lower than predicted values. The highest sea level was observed at Lowestoft, at 71 cm above the alert level. The highest sea level recorded in and around Great Yarmouth was just 10 cm from overtopping the sea walls. Overall there were no casualties, but damages to properties were reported (http://www.metoffice.gov.uk/about-us/who/how/case-studies/floods-2007). The difference in centimetres between the surge barriers in place and the actual storm surge can lead to devastating consequences. When sea

defences hold, the damage resulting from an intense storm can be minimal. When surge barriers are breached, there can be severe damage to properties and even loss of lives.

The 2007 North Sea Flood has been forecasted in the UK using the Met Office Global and Regional Ensemble Prediction System (MOGREPS) with good results [*Bowler et al.* 2008]. Initially developed for extratropical storm forecasting, ensemble prediction systems are noted as one of the best benchmarks for forecasting uncertainties in weather systems [*Froude et al*., 2007]. A single deterministic forecast, while consistent with the initial state of the environment, can miss an extreme event resulting from a different combination of initial conditions [*Flowerdew et al.*, 2010]. This is crucial in forecasting extreme events such as storm surges that are strongly driven by uncertainties in the weather system such as the track of the storm, the strength and structure of the surface pressure and winds, and the relative timing of the tides [*Horsburgh et al.*, 2011].

1.3.2 Southwest Atlantic

The coastline of Argentina is highly susceptible to storm surges, with Rio de la Plata and the Bahia Blanca estuary gathering much interest due to the dense population and high port activity respectively (e.g. *Fiore et al*. [2009] and *Seeliger and Kjerfve* [2001]). Three 2-dimensional depth-integrated (2DDI) models had been optimized for this region and was used to simulate a storm surge event in May 2000 [*Horsburgh et al.* 2011]. The simulation results compared well with observations after calibrating the bottom friction with the Chèzy coefficient. Bahia Blanca consisted of a short estuary with deep channels which was strongly affected by strong ebb currents in the channel enhancing the surge modification of tidal wetting and drying patterns. Calibration for the wetting and drying process was required in this area. The coastal geometry of Rio de la Plata was wider and allowed stronger surge-wave

interactions. In this region, the surge model had to be coupled with a wave model to improve the growth of the storm surge at its early stage.Table 1.2 summarizes the different surge modelling systems used in the regions discussed previously. One of the common challenges faced is the need for reliable and high resolution data from the predicted cyclone and coastal features. Even with high confidence in the predictive skill of surge models, setting up the model with low resolution information of the coastal features or providing cyclone data that are not well-represented can greatly impact the modelled storm surge. Incorporation of hydrology information (such as rivers and rainfall) is an area where several authors have noted to require more work (e.g. *Dube et al*. [1997] and *Lin et al.* [2010]), since the data is available but many models do not have the capability to incorporate it.

Region	**Model**	**Challenges faced**
Bay of Bengal	IIT surge model	Grid resolution, wind field, bathymetry, coastal geometry, inshore current, tides, rivers, precipitation.
Gulf of Mexico	SLOSH	Grid resolution, ocean bottom stress, tides, rivers, precipitation.
	ADCIRC	Grid resolution, ocean bottom stress, tides, rivers, precipitation.
Southwest Pacific	Surge model forced by TC-LAPS	Grid resolution, cyclone wind and pressure
North Sea	CS3X	Grid resolution, tides
Southwest Atlantic	2DDI models	Grid resolution, bottom friction, wetting and drying, surface waves

Table 1.2: Examples of storm surge modelling systems used and their challenges.

1.4 Processes contributing to storm surges

Harris [1963] has summarized the mechanics of a storm surge into five main components: wind, waves, atmospheric pressure, Coriolis effect and rainfall. Here, the effect of wind stress and the Coriolis effect will be discussed together. Waves will not be discussed in depth as it has been widely researched on (e.g. *Brown* [2010], *Dean and Bender* [2006]) and will not be incorporated into this model study. The mass and momentum contribution of rainfall will be discussed separately.

1.4.1 Wind stress

For two layers of moving fluid in contact, there will be momentum transferred from the faster moving layer to the slower one. The stress on the sea surface due to wind, or wind stress (τ_w) can be expressed as follows [*Pugh*, 1987]:

$$\tau_w = C_D \rho_A \vec{v}^2 \tag{1.1}$$

where C_D is the dimensionless drag coefficient, ρ_A is the air density and $\vec{v}$ is the wind velocity.

Due to the square law relationship between wind stress and wind speed, the orthogonal components of wind stress are resolved as follows to retain its direction:

$$\tau_{wx} = C_D \rho_A |\vec{v}| U \tag{1.2}$$

$$\tau_{wy} = C_D \rho_A |\vec{v}| V \tag{1.3}$$

where τ_{wx} and τ_{wy} are the x and y components of wind stress respectively and U and V are the corresponding x and y components of wind speed.

Considering the case of wind blowing along a channel of constant depth, the steady state effect of the wind stress on the sea surface slope generated can be represented by:

$$\frac{\partial \zeta}{\partial x} = \frac{C_D \rho_A \vec{v}^2}{g \rho_W D} \tag{1.4}$$

where ζ is the sea surface elevation, g is the gravitational acceleration, ρ_W is the density of sea water and D is the depth of the water body. Also known as wind set-up, equation (1.4) describes the effect of wind on sea surface elevation increasing inversely with water depth. Hence, wind blowing across extensive areas of shallow waters will produce a larger increase in sea levels. Due to the temporally varying 3D nature of storm surges, steady state assumptions may not be realistic. However, they are helpful in understanding the order of magnitude of different effects. In storm surge modelling, achieving numerical solutions of a dynamic storm will be more reasonable.

The Coriolis effect can also affect the wind-driven surge levels. Any wind vector blowing across the coastline can be resolved into its two orthogonal components: the cross-shore and the alongshore components. The wind component blowing onshore (orthogonal to the

coastline) creates a direct wind set-up and increases the height of the storm surge. The wind component blowing alongshore (parallel to the coastline) can be deflected by Coriolis force to change the sea surface elevation at the coast. In the northern hemisphere, if the coastline is located to the right of the alongshore wind component, the sea level at the coast increases. If the coastline is to the left of the alongshore wind component, the sea level at the coast decreases. Consider the case of a uniform wind stress (F_s) acting on the ocean surface at time t at the coastline with no cross-boundary flow ($v = 0$) (Figure 1.1):

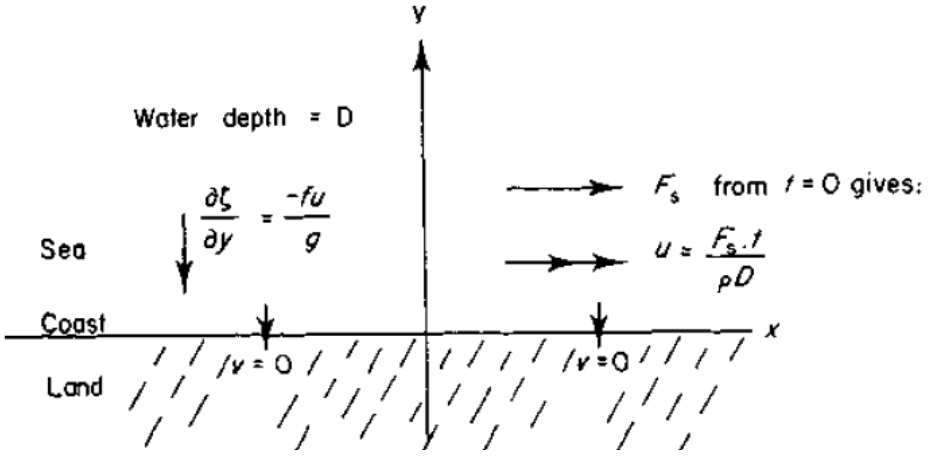


Figure 1.1: Ocean response to the alongshore wind stress at the coast. Extracted from *Pugh* [1987].

The horizontal momentum equations and the hydrostatic relationship reduces to [*Pugh*, 1987]:

$$u = \frac{F_s t}{\rho D} \tag{1.5}$$

and

$$\frac{\partial \zeta}{\partial y} = -\frac{fu}{g} \tag{1.6}$$

where u is the alongshore velocity and f is the Coriolis parameter.

The implication of equation (1.5) is that the alongshore current increases with time at a rate inversely proportional to the depth of the water body. In practice, this current does not increase indefinitely and is limited by the bottom friction. Equation (1.6) shows the sea surface gradient normal to the coastline in geostrophic balance with the alongshore current u, where u increases with time correspondingly. The sea surface height gradient also increases with depth.

Onshore and offshore winds induce a positive and negative surge respectively. In the case study of a storm surge generated by a counter-clockwise rotating storm hitting the coast of Orissa, India, *Pugh* [1987] described the positive surge generated to the right of the storm track due to the onshore winds and a negative surge generated to the left of the storm track due to the offshore winds. A clockwise rotating storm in the southern hemisphere was described by *Pousa et al.* [2013], hitting the coast of Argentina in 1984. Here, a positive surge was generated at Mar de Plata and a negative surge at Buenos Aires, which is located north of Mar de Plata.

Positive surges are widely studied due to the high impacts of coastal flooding but negative surges are less well understood. Some impacts of negative surges include ship grounding and draining of coastal aquifers. Ship grounding can lead to hull damage, subsequent collisions and/or oil spills. The draining of coastal aquifers can lead to the depletion of drinking water supply and is a concern to coastal communities dependent on it [*Pousa et al.*, 2013]. Negative surges can also destroy coastal aquacultures that countries such as Bangladesh depend on as a major economic contributor [*AsSalek*, 1997]. *AsSalek* [1997] showed that negative surges are affected by factors such as the cyclone's inflow angle, central pressure, radius of maximum winds, speed of translation, propagation path, angle of coastal crossing and the interaction with astronomical tides. However, the study was specific to the unique coastal geometry of

the Meghna estuary and is based on the sea surface height response at nine selected points along the coast, making it difficult to apply the same conclusions to other coastal cases. Figure 1.2 shows the geometry of the Meghna estuary and an example of how the extent of the negative surges changes due to a doubling of the cyclone moving speed.

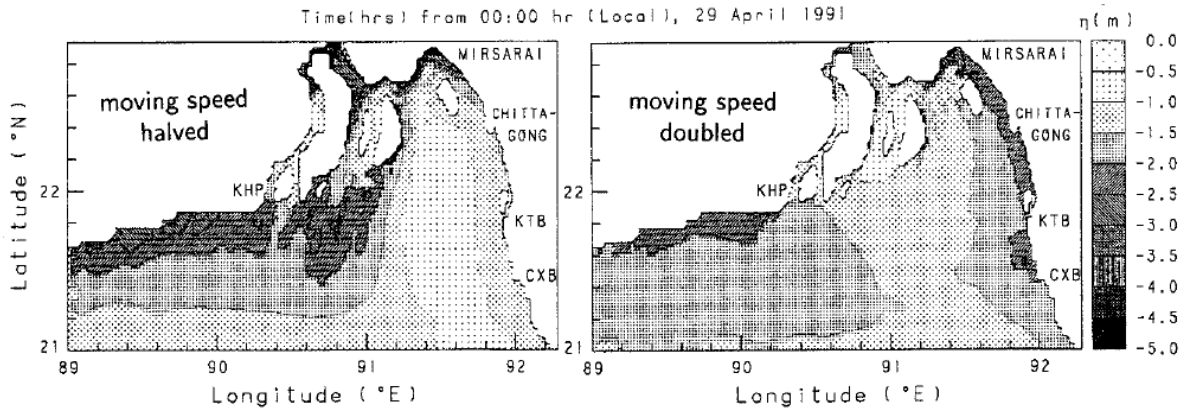


Figure 1.2: Changes in the water level (η) in the Meghna estuary after doubling the moving speed of the cyclone. Extracted from *AsSalek* [1997].

Peng et al. [2006] studied the asymmetry in positive and negative surges generated in an idealized coastal set-up, investigating the sensitivity of the surges to the cyclone's inflow angle, radius of maximum winds and the speed of translation. However, this idealized study was limited to a one-dimensional analysis where the positive and negative sea surface height response was investigated at a single point and did not account for the simultaneous occurrence of positive and negative surges at the coastline, as reported by *Pousa et al.* [2013] and *Pugh* [1987]. This will be investigated in detail in Chapter 4.

Apart from driving horizontal motion, wind stress can affect the vertical motion of ocean waters. The transfer of momentum from an anti-clockwise rotating wind stress (in the Northern hemisphere) deflects the wind-driven layer of the ocean to the right of the wind direction, creating divergence of surface water and upwelling of subsurface water. Also

known as Ekman pumping [*Colling*, 2001], this results in a lowering of the sea surface height and raising of the thermocline. On the other hand, clockwise-rotating winds will cause a convergence of surface water due to the deflection of the rotating winds to the right. This generates a rise in sea surface height, downwelling of subsurface water and lowering of the thermocline. This is illustrated in

Figure 1.3. This effect will be reversed in the Southern hemisphere.

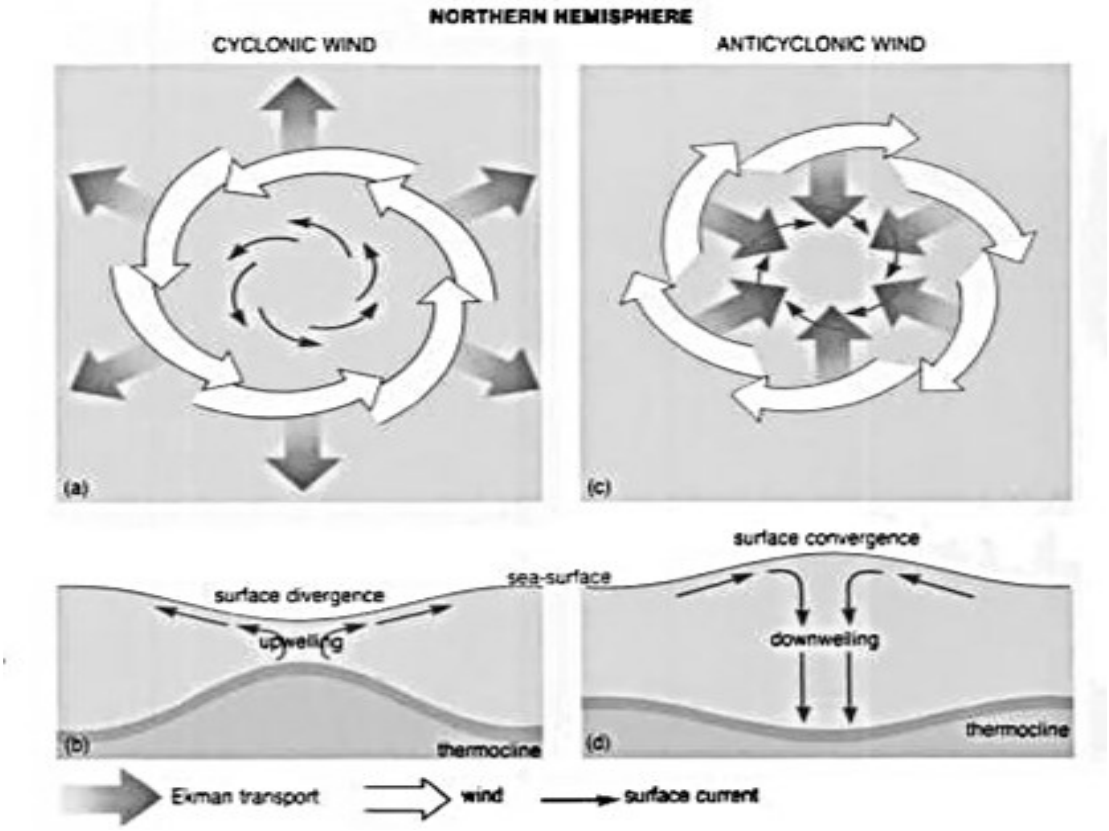


Figure 1.3: Ekman pumping driven by the rotating winds. Extracted from *Colling* [2001].

1.4.2 Pressure effect

The inverse (or inverted) barometer effect was first described by Nils Gissler in 1747 [*Roden and Rossby*, 1999], where he estimated a 1 cm drop in sea surface height for every increase of

1 mbar in atmospheric pressure. The correlation between sea level height and atmospheric pressure can be seen in Figure 1.4 where the sub-tidal variations of the sea level in the Celtic Sea are compared against the atmospheric pressure recorded at St. Mary's [*Pugh*, 1987].

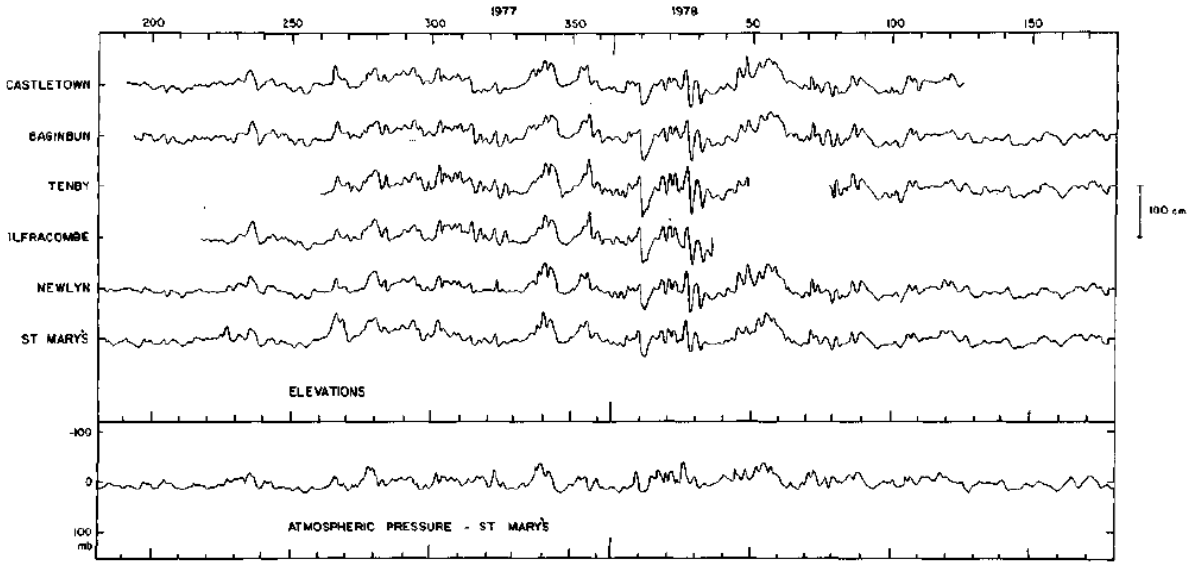


Figure 1.4: Sub-tidal variations in sea level height at various locations around the Celtic Sea, compared against the atmospheric pressure at St. Mary's. Extracted from *Pugh* [1987].

The inverse relationship between sea level height and atmospheric pressure can be modelled theoretically and has been incorporated in many ocean models. For local variations in atmospheric pressure (ΔP) about the mean atmospheric pressure over the ocean surface, the variation in sea surface level ($\Delta\zeta$) about the mean sea level is as follows [*Pugh*, 1987].:

$$\Delta\zeta = -\frac{\Delta P}{\rho_w g} \qquad (1.7)$$

where ρ_w is the density of sea water and g is the gravitational acceleration.

Taking density of sea water as 1026 kg m^{-3} and gravitational acceleration as 9.81 m s^{-2}, equation (1.7) is evaluated as $\Delta\zeta = -0.994\Delta P$ (where $\Delta\zeta$ is in cm and ΔP is in mbar) and is

similar to Gissler's approximation of 1 cm increase in sea surface height for every 1 mbar decrease in atmospheric pressure. For a typical tropical cyclone with a pressure drop of 50 – 100 mbar, this would correspond to an increase in the sea surface height by 50 – 100 cm.

1.4.3 Surface wave effect

While common bulk formula for air-sea fluxes assumes that the magnitude of wind stress is dependent only on the wind speed (Section 1.4.1), it has long been recognized that wind stress is also a function of the sea state and atmospheric stability (e.g. *Monin and Obukhov* [1954] and *Charnock* [1955]. Many bulk parameterizations has been based on field measurements in wind regimes of less than 25 m s^{-1}, with the drag coefficient increasing monotonically with wind speed [*Moon et al*., 2004]. In the case of tropical cyclones, *Moon et al*. [2003] have shown that the surface wave field is complex and dominant waves can even propagate at conflicting angles to the local wind. By combining an ocean-wave model and a wave boundary layer model, it has been found that the drag coefficient does not increase monotonically with wind speed for the case of extreme wind speeds. There is a levelling off or even a decrease of the drag coefficient due to the young waves generated by the strong winds. The spatial variability of the drag coefficient is also found to increase with the hurricane translation speed.

Excess momentum flux from surface gravity waves at the shore, also known as radiation stress, can induce changes to the sea surface elevation. *Dean and Bender* [2006] have shown that the effect of radiation stress cannot be neglected in the coastal sea level rise during storm events. When waves break at the shoreline, they carry considerable amount of water shoreward. The process of wave breaking can generate significant transport of more than twice the wave height due to the momentum the waves carry [*Harris*, 1963]. If the waves

break far from the shore, the energy is dissipated as turbulence. If the waves break near the shore, the water cannot flow back to the ocean as rapidly as it was brought to shore and a gradient in water level is created. This is known as wave set-up. The overall storm surge contribution of radiation stress reported varies greatly. *Brown* [2010] studied the independent effects of waves by coupling a wave model to an ocean model and found that wave set-up could increase the overall height of the storm surge by 50 - 150 cm. *Mastenbroek et al.* [1993] modelled three separate storms in the North Sea and found that the effect of radiation stress can increase the storm surge by up to 5%. *Kim et al.* [2010] modelled the wave set-up in the storm surge during Typhoon Anita and found that radiation stress can contribute up to 40% of the peak sea level rise. Nevertheless, there have been many studies investigating and quantifying the effect of waves on storm surges and this will not be covered further in this thesis. However, the model used in this study has the capability of coupling the effect of waves and future work could incorporate waves to enhance the comprehensiveness of this study.

1.4.4 Rain mass

Many studies such as *Bao et al.* [2004] have argued that the temperature and salinity effects of rainfall should not be neglected in ocean circulation models as these effects can significantly affect air-sea heat flux estimates. It has since become more common for ocean models to incorporate the temperature and salinity effects of rainfall. However, the mass contribution of rainfall continues to be disregarded. While the effect of incorporating freshwater mass from rivers has been extensively studied (e.g. *Warner et al.* [2005]), the effect of adding freshwater mass from rain directly to the ocean is unknown and is implicitly thought to be negligible. There is very little work addressing the contribution of rain mass to

sea surface heights. *Ponte* [2006] incorporated realistic freshwater fluxes in a global barotropic model and found that they can cause annual standard deviations in sea surface level can be as large as 1 cm, especially in shallow and semi-enclosed regions.

Jacob and Koblinsky [2007] modelled a hurricane case using the Hybrid Coordinate Ocean Model (HYCOM) to investigate the response of the ocean mixed layer to the temperature and salinity fluxes from rainfall. They found that including the heat and salinity of precipitation in the model can cool the mixed layer temperature by up to 4.5°C and freshen the mixed layer salinity by up to 0.3 psu. However, the response from including precipitation mass was neglected. *Wijesekera et al.* [2003] modelled the sea surface anomaly due to tropical rainfall, outlining only the exchange of heat and salinity fluxes between rainfall and the ocean in the Princeton Ocean Model (POM). *Wang et al.* [2008] used ROMS to quantify the relative importance of only the inverted barometer effect and wind effect for the Irish coast line. However none of these studies include how the effect of rain could effectively contribute to the storm surge. *Sheng et al.* [2012] described a test platform used to review several established storm surge models such as CH3D-SSMS [*Sheng et al.*, 2010], ADCIRC [*Westerink et al.*, 1992], FVCOM [*Chen et al.*, 2008], CMEPS [*Peng et al.*, 2004] and SLOSH [*Jarvinen and Lawrence*, 1985]. Thirty scenarios were used to test their sensitivity towards parameters such as bathymetry, storm forcing, wind drag coefficient, bottom friction, Coriolis and 2D-3D formulation, but precipitation was not investigated. The lack of studies investigating the mass contribution of rainfall to storm surges is not surprising, since many common ocean circulation and storm surge models do not incorporate rain mass into the model at all.

FVCOM is a finite volume, primitive equation, hydrostatic, mesoscale ocean circulation model and is developed by the School of Marine Science, University of Massachusetts. Due

to the topological flexibility of its unstructured grid system, it has been widely used from global scales to estuarine scales, particularly in regions that are characterized by irregular coastlines such as islands, inlets, inter-tidal zones and streams. Precipitation is considered in terms of exchanges in temperature and salinity, but not in mass. In particular, there is no addition of rain mass in the sea surface height or in the vertical velocity routines (e.g. vertvl_edge.F).

ROMS [*Shchepetkin and McWilliams*, 2005] is a free-surface, hydrostatic, split-explicit, primitive equation ocean model that has many research applications including modelling of river plumes (e.g. *Hetland* [2005]), estuaries (e.g. *Warner et al.* [2005]), sea ice (e.g. *Dinniman et al.* [2007]) and storm surges (e.g. *Li et al.* [2006]). While temperature and salinity changes due to rainfall are calculated in the bulk flux routine, the effect of rain mass has not been considered in the model to date. In ROMS, the sea surface elevation remain unchanged no matter how much rainfall is introduced. In Chapter 2, the effect of rain mass will be incorporated into ROMS, for the first time. In Chapter 3, this effect will be isolated and investigated in an idealized set-up of ROMS. Finally, the effect of rain mass on storm surges will be compared against the effect of wind, pressure and rain stress in a case study outlined in Chapter 5 to understand how substantial the contribution of rain mass can be.

1.4.5 Rain stress

Rain stress is an under-studied phenomenon. While wind stress is the shear stress exerted by wind on the water surface, rain stress is exerted on the water surface when raindrops impact the surface, transferring mass and momentum to the water body. The transmission of momentum from raindrops to the water surface was first investigated by *Van Dorn* [1953] where he measured the surface stress in an artificial pond, comparing three different types of

surface conditions. The surface stress was first measured and compared between a normal water surface case and one with reduced surface drag where soap was applied to the water surface. Here, the surface stress reduces in the presence of soap. Subsequently, artificial droplets simulating rain were added to investigate how rain can affect the surface stress (Figure 1.5). In the presence of rain, the surface stress increases.

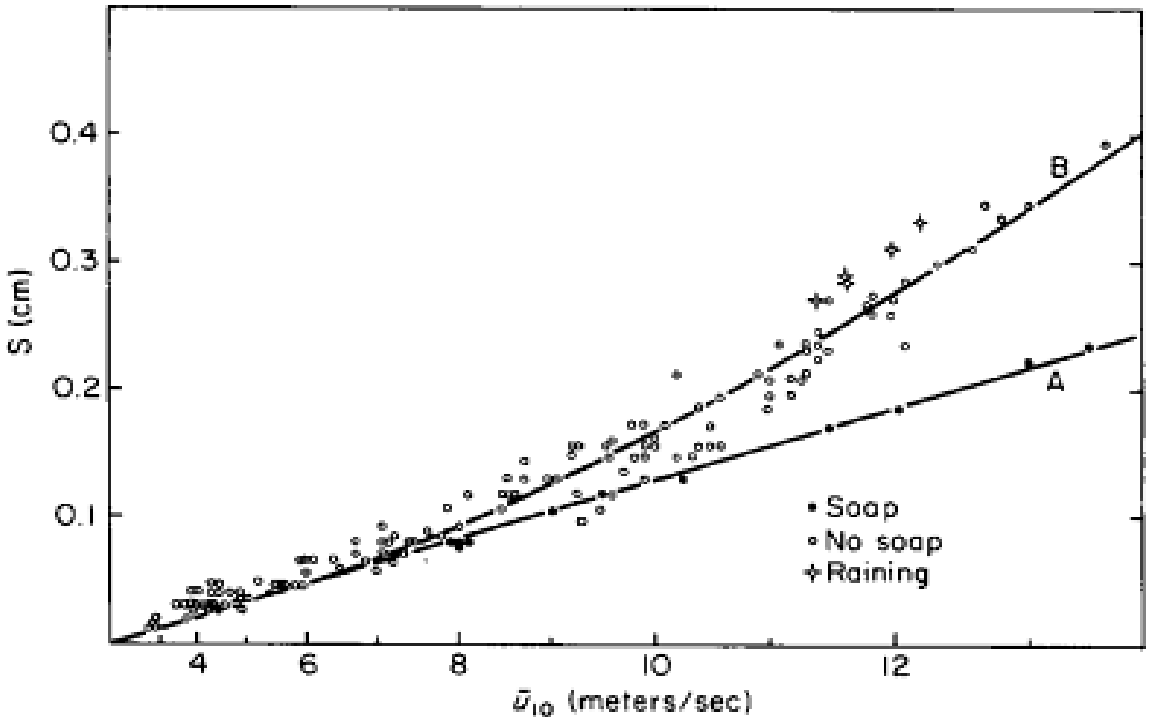


Figure 1.5: Relationship between surface stress and wind speed at 10 m. Extracted from *Van Dorn* [1953].

Caldwell and Elliott [1970] modified several assumptions made by *Van Dorn* [1953] and parameterized rain stress as a function of rain rate and wind speed. They pointed out that *Van Dorn* [1953] incorrectly assumed the typical raindrop size as 6 mm when *Cataneo and Stout* [1968] showed that 1 - 2 mm is more reasonable. Additionally, an incorrect drag coefficient for raindrops was used. Finally, the horizontal component of the total force acting on the raindrop should be used instead of simply using the horizontal wind speed. Figure 1.6 shows

how gravity and the drag forces of air act on a raindrop of mass m. The velocity of the raindrop (U_r) is at an angle θ to its vertical velocity (W) and U-V represents the horizontal speed of the raindrop relative to the speed of the air.

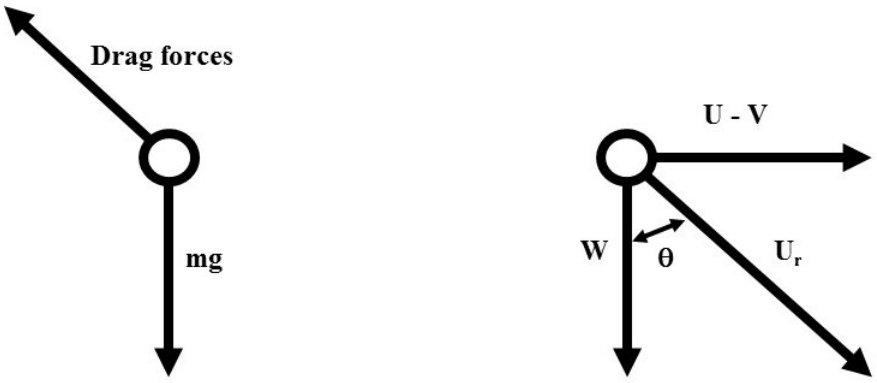


Figure 1.6: Gravity and drag forces acting on a raindrop (left) and the horizontal and vertical velocities of a raindrop (right) [*Caldwell and Elliott*, 1970].

The rain stress parameterization proposed by *Caldwell and Elliott* [1970] assumes a logarithmic wind profile to calculate the drop in velocity over a range of typical raindrop sizes. It has been found that the droplet speed at impact is on average 15% lower than the wind speed at 10 m. Hence, it is proposed that the ratio of rain stress (τ_r) to wind stress (τ_w) can be expressed as follows:

$$\frac{\tau_r}{\tau_w} = \left(\frac{\rho_r}{\rho_a}\right)\left(\frac{0.85R}{C_{10}\vec{v}_{10}}\right) \tag{1.8}$$

where ρ_r is the density of rain, ρ_a is the density of air, R is the rain rate, C_{10} is the drag coefficient at 10 m and $\vec{v}_{10}$ is the wind velocity at 10 m.

Equation (1.8) simplifies to:

$$\tau_r = 0.85 R \rho_r \vec{v}_{10} \qquad (1.9)$$

The work of *Caldwell and Elliott* [1970] has been widely referenced. *Fairall et al.* [1996] have included the energy and momentum interactions between rain and the ocean in their bulk parameterization that relates near-surface atmospheric variables with the oceanographic bulk variables. They have also tuned the algorithm to fit the measurements made on three different cruise legs during the Coupled Ocean-Atmosphere Response Experiment (COARE). The Regional Ocean Modelling System (ROMS) used in this thesis has adopted this bulk parameterization. *Clayson and Kantha* [1999] incorporated the parameterization of rain stress in their one-dimensional mixed layer model to study the characteristics of turbulent mixing in the western Pacific warm pool. They found that while the Turbulent Kinetic Energy (TKE) and dissipation rates are significantly elevated during the westerly wind bursts, turbulent mixing does not penetrate much below the mixed layer due to the equatorial undercurrent being too weak and too deep to propagate the mixing. *Andreas* [2004] compared and contrasted this rain stress parameterization with his formulation for the transfer of momentum from sea spray. Unlike rainfall, sea sprays are bounded by the conservation of momentum in the system and cannot enhance the air-sea stress beyond the large scale flow however sea sprays can redistribute the momentum by slowing down the near-surface winds. It was shown that the mass flux from sea spray to the sea surface damps short waves and reduces the surface drag, creating a negative feedback that limits the air-sea momentum transfer. While the parameterization of rain stress has been incorporated in many models and used for comparison with other processes, its isolated effect has never been shown. In the context of storm surges, the effect of rain stress has not been quantified or compared with other processes affecting storm surge heights. This shall be further investigated in Chapter 3 and 5.

1.5 Thesis plan

This study investigates the relative importance of the following physical processes affecting storm surges: wind, atmospheric pressure, rain stress and rain mass. This is carried out with the use of WRF to create the atmospheric conditions and ROMS to simulate the oceanic response to the atmospheric state generated using WRF. Chapter 2 introduces and discusses the set-up of WRF and ROMS. The mass of rainfall, which has been neglected in ROMS to date, has been incorporated into the model. Chapter 3 studies the effect of rain mass and rain stress on the sea surface elevation. An idealized cyclone is generated using WRF and is used as an atmospheric forcing in an idealized set-up of ROMS to show their isolated effects. Chapter 4 investigates the asymmetry between positive and negative surges, which has been reported in literature but not extensively studied. Chapter 5 combines the understanding of the rain effects in Chapter 3 and the wind effects Chapter 4 through a case study of a real tropical cyclone. The effects of rain mass and rain stress are quantified and compared against established storm surge processes such as the wind-driven effect and the pressure-driven effect. The significance of rain mass and rain stress in the context of storm surges is determined.

2 Model description

2.1 COAWST model

The Coupled Ocean–Atmosphere–Wave–Sediment Transport (COAWST svn 711) Modelling System [*Warner et al.*, 2010] has been used in this study as a platform where the atmosphere model WRF and the ocean model ROMS are set up. COAWST is developed by the Woods Hole Science Coastal and Marine Science Center and is designed to couple several key circulation models to study their interdependence and coupled effects. The component modules within COAWST include WRF, ROMS, the wave model Simulating WAves Nearshore (SWAN) [*Booij et al.*, 1999] and the sediment capabilities of the Community Sediment Transport Model (CSTM) [*Warner et al.*, 2008]. The Model Coupling Toolkit (MCT) [*Larson et al.*, 2005] uses a parallel coupled approach to transmit and transform distributed data between the component models within COAWST. The Spherical Coordinate Remapping Interpolation Package (SCRIP) [*Jones*, 1998] is used to compute weights to interpolate between different grids used by the different models. In this study, only WRF and ROMS are used and there is no coupling between the processes in the two models. However, some preliminary work on coupling processes has been conducted and COAWST can serve as a suitable platform for future work.

2.2 ROMS model

The ocean domain studied in this thesis is simulated using ROMS version 3.4, with *Shchepetkin and McWilliams* [2005] and *Warner et al.* [2005] outlining the computational algorithms used. ROMS is a free-surface, hydrostatic, split-explicit, primitive equation ocean

model that uses stretched, terrain-following coordinates in the vertical and orthogonal curvilinear coordinates in the horizontal. Jointly developed by Rutgers University and the University of California at Los Angeles, ROMS is used widely in many different applications, including modelling of river plumes (e.g. *Hetland* [2005]), estuaries (e.g. *Warner et al.* [2005]), sea ice (e.g. *Dinniman et al.* [2007]) and storm surges (e.g. *Li et al.* [2006]).

The horizontal equations of motions are shown here in Cartesian coordinates:

$$\frac{\partial u}{\partial t} + \vec{v}.\nabla u - fv = -\frac{\partial \phi}{\partial x} - \frac{\partial}{\partial z}\left(\overline{u'w'} - \nu\frac{\partial u}{\partial z}\right) + F_u + D_u \quad (2.1)$$

$$\frac{\partial v}{\partial t} + \vec{v}.\nabla v + fu = -\frac{\partial \phi}{\partial y} - \frac{\partial}{\partial z}\left(\overline{v'w'} - \nu\frac{\partial v}{\partial z}\right) + F_v + D_v \quad (2.2)$$

where t is time, (x,y) are the horizontal coordinates, z is the vertical coordinate, (*u,v,w*) are the (x,y,z) components of vector velocity ($\vec{v}$), *f* is the Coriolis parameter, ν is the molecular viscosity, ϕ(x, y, z, t) is the dynamic pressure, F_u, F_v are the forcing terms and D_u, D_v are the diffusive terms. The overbar represents a time average and the prime represents a fluctuation about the mean.

The time evolution of the scalar concentration field C(x, y, z, t) (such as salinity and temperature) is governed by the advective-diffusive equation:

$$\frac{\partial C}{\partial t} + \vec{v}.\nabla C = -\frac{\partial}{\partial z}\left(\overline{C'w'} - \nu_\theta\frac{\partial C}{\partial z}\right) + F_C + D_C \quad (2.3)$$

where ν_θ is the molecular diffusivity, F_c is the forcing term and D_c is the diffusive term.

These equations are closed by parameterizing the Reynolds stresses and turbulent tracer fluxes as:

$$\overline{u'w'} = -K_m \frac{\partial u}{\partial z} \tag{2.4}$$

$$\overline{v'w'} = -K_m \frac{\partial v}{\partial z} \tag{2.5}$$

$$\overline{C'w'} = -K_C \frac{\partial C}{\partial z} \tag{2.6}$$

where K_m and K_C are the mass and scalar concentration vertical eddy viscosities.

The equation of state that correlates the density in terms of temperature, salinity and pressure is given by:

$$\rho=\rho\ (T, S, P) \tag{2.7}$$

where T is potential temperature, S is salinity and P is total pressure where $P \approx -\rho_0 gz$ and $\rho_0 = \rho(x, y, z, t)$ is the total *in situ* density.

The Boussinesq approximation is made, neglecting the density variations in the momentum equations except where there is a contribution to the buoyancy force in the vertical momentum equation. Together with the hydrostatic approximation, where the vertical pressure gradient balances the buoyancy force, the vertical motion is expressed as follows:

$$\frac{\partial \phi}{\partial z} = -\frac{\rho g}{\rho_0} \tag{2.8}$$

where $\phi(x, y, z, t)$ is the dynamic pressure, $\phi = (P/\rho_0)$ and g is the gravitational acceleration.

Assuming incompressibility, the continuity equation is expressed as follows:

$$\frac{\partial u}{\partial x} + \frac{\partial v}{\partial y} + \frac{\partial w}{\partial z} = 0 \qquad (2.9)$$

By discretizing the continuity equation using a finite volume approach and summing vertically, we obtain the free-surface relationship as follows:

$$\zeta_{i,j}^{n+1} = \zeta_{i,j}^{n} - \frac{\Delta t}{\Delta A_{i,j}}\left[\overline{U}_{i+\frac{1}{2},j} - \overline{U}_{i-\frac{1}{2},j} + \overline{V}_{i,j+\frac{1}{2}} - \overline{V}_{i,j-\frac{1}{2}}\right] \qquad (2.10)$$

Where ζ is the free surface, $\Delta A_{i,j}$ is the horizontal area of the grid box i, j, $\overline{U}$ and $\overline{V}$ are the barotropic volume fluxes, E and P are the evaporation and precipitation volume fluxes at time, t.

In a time-splitting, free surface model such as ROMS, the free-surface Equation 2.10 and the vertically integrated momentum equations are advanced using a smaller time step compared to the tracer equations. The 3D momentum components (Equations 2.1 and 2.2) are computed during the baroclinic time step and vertically integrated to provide forcing terms for the barotropic mode. During the barotropic time stepping, the free surface and the barotropic velocities are averaged over the barotropic time steps and fed back into the 3D momentum equations.

The energy and salinity exchange of rain is included in the bulk parameterization as outlined by *Fairall et al.* [1996], with adjustments using the data from the Tropical Ocean Global Atmosphere Coupled Ocean–Atmosphere Response Experiment (TOGA COARE). Sensible heat flux due to rain (H_r) is calculated using the mass of rain introduced to each grid and the difference between the air and sea temperatures. It is assumed that the rain is at the wet-bulb temperature:

$$H_r = -RC_w\alpha_w\,(1+\frac{1}{B_0})(T_{sea}-T_{air}) \qquad (2.11)$$

where R is the mass flux of rain, C_w is the specific heat of liquid water, α_w is the Clausius-Claperyon wet-bulb factor [*Fairall and White*, 1994], B_0 is the bulk Bowen ratio, T_{sea} is the sea temperature and T_{air} is the air temperature.

The salt flux in or out of the ocean (Stflx) is calculated based on the difference in evaporation (E) and precipitation (R) rates:

$$Stflx = \frac{1}{\rho_w}(E-R) \qquad (2.12)$$

where ρ_w is the density of water.

As the adding of rain mass (Section 2.2.1) requires grid manipulation and reformatting of variables, a description of the horizontal and vertical discretization of the governing equations is provided here. The ROMS governing equations are discretized over orthogonal curvilinear coordinate grid. The eta (η) points are in the direction of the latitudinal points while the xi (ξ) points in the direction of the longitudinal points. The state variables are staggered using an Arakawa C-grid (e.g. *Arakawa and Lamb* [1977] and *Collins et al.* [2013])

as shown in Figure 2.1. The free surface, density and tracers are located in the centre of the cells (ρ points). There are 3 tracer types: the active tracers (potential temperature and salinity), the inert tracers (dyes and pollutants) and passive tracers (sediment and biological). The horizontal velocities (*u* and *v*) are located at the west-east and north-south cell edges. Overall, the ρ-point quantities are evaluated between the points where currents are evaluated.

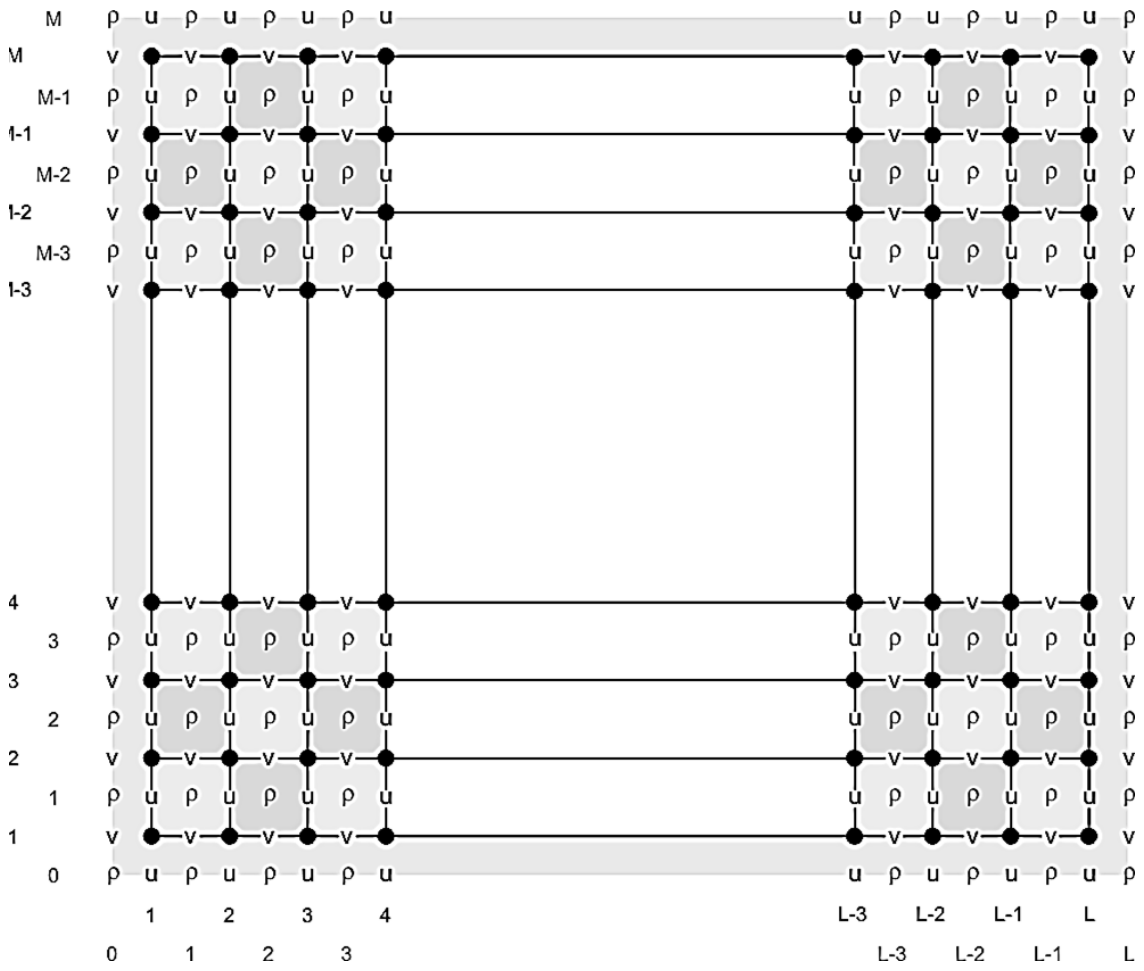


Figure 2.1: Arakawa-C grid staggering of the ROMS grid showing the horizontal velocity points (*u* and *v*) and density (ρ).

In the vertical direction, the governing equations are discretized over the topography using a stretched, terrain-following sigma (σ) coordinate. Hence, each cell may have different thickness (Hz) and volume. The state variables are staggered vertically such that the density

(ρ), horizontal velocities (*u, v*) and tracers are located at the centre of the grid cell. The vertical velocity (*w*) is located at the top and bottom faces of the cell. This is illustrated in Figure 2.2.

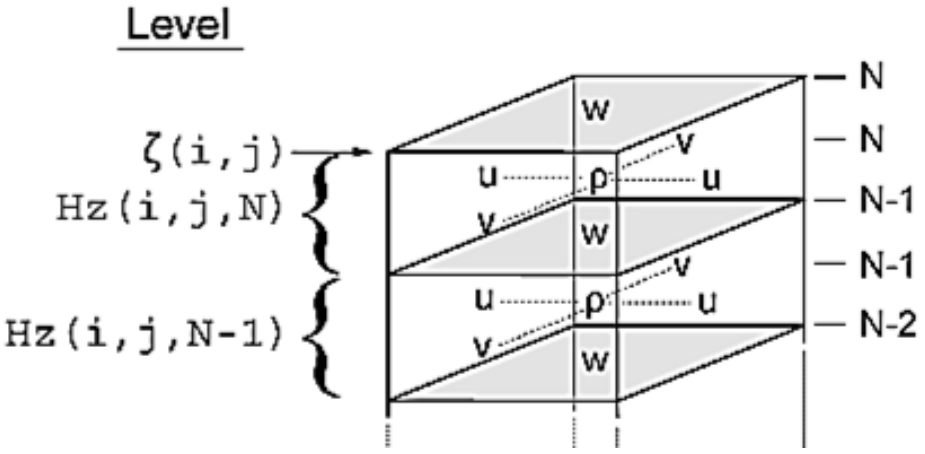


Figure 2.2: Vertical coordinate system of the ROMS grid showing the horizontal velocity points (*u* and *v*), vertical velocity points (*w*) and density points (ρ).

2.2.1 Set-up of the new rainfall scheme in ROMS to introduce rain mass

Introducing point sources or sinks is a method employed in ROMS to add or remove mass and momentum into the system. This is an approach widely used within the ROMS modelling community to introduce river run-off. The option of providing river run-off is enabled by the 'LuvSrc' definition in the model which imposes a point source via the horizontal fluxes that crosses the u-face or v-face of a cell (Arakawa-C gridding system). By introducing an additional positive volumetric flow rate to the specified cell, mass is introduced to it. On the other hand, introducing an additional negative volumetric flow rate to the specified cell will remove mass from it. The advection operator then takes the divergence of the volume fluxes. While this definition introduces mass into the system, it introduces horizontal momentum and

is not suitable for rain mass. The 'LwSrc' definition in the model imposes a source via a vertical mass flux that crosses the w-face of the cell. The 'LwSrc' definition has been provided in ROMS for the sake of completeness and has no practical applications within ROMS to date. The function and effect of introducing a vertical momentum source term in this manner has never been reported and is unknown within the ROMS community. Here, this approach is used for the first time to introduce rain mass to the model. However, it is not intended to introduce momentum since the transfer of momentum from rainfall to the ocean surface has already been parameterized (further discussed in Chapter 3). Nevertheless, with the small amount of mass flux added, it is likely that the vertical momentum introduced will not be substantial. This will be verified later in Chapter 3.

The variables required in ROMS to set up point sources are provided in Table 2.1. These variable names have been named and recognized in ROMS as 'rivers' since this is the most common and widely used application for point sources. While the variables used for atmospheric forcing in ROMS (namely wind velocity, specific humidity, atmospheric pressure, cloud cover, rain rate, longwave and shortwave radiation) are provided as a function of time and position, point sources are specified as a function of identification number and sigma level. The river identification number provides the ξ position, η position, vertical profile and the vertical integrated mass flux of each point source specified. Rivers are not explicitly defined to be a function of time, since it is implicit in the vertical integrated mass flux rate. Unlike rivers, rainfall is not a continuous volumetric flux generated from a fixed position in space. To simulate rainfall, an additional function is included to map the identification number back to its position to create a rainfall term that is a function of position instead of the identification number. Rainfall is now treated as a fluctuation at each position to simulate a continuous rainfall travelling from one grid point to the next. This aligns the

way point sources are implemented with the way ROMS is forced by atmospheric variables. To simulate the addition of rain mass to the sea surface, the point source is introduced only to the surface-most sigma level. This is different from the case of rivers where the mass flux can be distributed through the sigma levels.

Variable name	***Description***	***Variable is a function of:***
river	identification number	-
river_time	model time	-
river_Xposition	ξ-position	river
river_Eposition	η-position	river
river_Vshape	mass transport vertical profile	sigma level, river
river_transport	vertically integrated mass flux	river_time, river

Table 2.1: Variables required in ROMS to set up a point source.

Rain information produced from the WRF simulation output is first formatted into an input file recognized by ROM. WRF generates two output variables for rainfall: RAINC and RAINNC. RAINC is the rainfall from the cumulus parameterization and RAINNC is the rainfall from the cloud microphysics scheme. The sum of the two quantities yields the total rainfall generated in WRF. Both RAINC and RAINNC are cumulative and have to be differenced between each time-step to obtain the instantaneous rainfall rates. This rainfall quantity is finally renamed as the variable 'rain' and converted from the units of mm in WRF to the units of kg m^2 s^{-1} in ROMS. This is a commonly used approach to reformat WRF rain

data for the purpose of forcing ROMS. Finally, the rain data is converted from the forcing file into a point source format using a separate script written using the NCAR Command Language (NCL) (http://dx.doi.org/10.5065/D6WD3XH5). The rain data can either be written into the analytical file ana_psource.h or a Network Common Data Form (netCDF) file (http://www.unidata.ucar.edu/software/netcdf/). The approach of using an analytical file is simpler in manipulating the rainfall rates, but requires compiling the entire rain information into the ROMS executable file. To implement this, the total number of non-zero point sources has to be pre-determined to reduce excessive memory usage in writing zero rain data. Nevertheless, this is still a time-consuming and inflexible approach. The netCDF file approach writes the rain data into a separate file that ROMS reads in during its computational iterations. The netCDF file is much larger in size as it is a 3D array that includes all entries of rain at every time and position. However, there is no downtime in compiling the model once the netCDF file is generated. This approach involves more pre-processing to format the rain information and requires a greater understanding in the way ROMS reads in the forcing data. Overall it is more flexible especially when different rain data sets are used for different simulations.

For both methods, the unit of the rain data has to be converted from kg m^2 s^{-1} to m^3 s^{-1} and assigned to the variable river_transport. river_transport is the vertically integrated volume transport and is a function of time and the identification number. The non-dimensional shape function is river_Vshape which specifies the vertical profile distribution of the point source. It is a function of the vertical sigma level and the identification number. Providing an equal distribution will generate a source that is apportioned equally through the sigma levels. The function river_Vshape must sum to 1 over all the sigma levels. In this case, river_Vshape is specified to introduce the mass flux at one level below the surface-most w-level to simulate

precipitation mass addition from the ocean surface. Point sources cannot be introduced at the surface-most w-level as any vertical velocities present at this level is equated to zero by the free surface routine in ROMS to ensure zero velocities at the free surface. Each set of ξ and η positions is assigned to a specific river identification number in ascending order. Rainfall rate at each position is directly assigned to the river identification number instead of the ξ and η positions. Here, the unique river identification number (river) specifies a unique river_Xposition, river_Yposition, river_transport and river_Vshape (Table 2.1). Temperature and salinity are not prescribed and the existing temperature and salinity state of the ocean is adopted by the point source.

Since the existing ROMS code only considers the temperature and salinity effects of rainfall but not the mass, the point source addition of rain mass will complement the existing implementation by not altering temperature and salinity. However, the two implementations (existing and point sources) will be compared and examined separately in Chapter 3 to isolate their effects. Ultimately, the new rainfall scheme will not replace the existing treatment of rainfall but should be implemented together to achieve a more realistic representation of rainfall that considers its temperature, salinity and mass.

2.2.2 Set-up of the idealized ocean model

An idealized set-up is useful in creating a highly controlled environment to isolate specific effects and processes. This set-up is used in Chapters 3 and 4. Here, the ROMS model is set up with 21 vertical levels and a horizontal resolution of 15 km over the same spatial extent as WRF (5°N to 35°N and 120°E to 180°E) and illustrations are zoomed into a smaller region as shown in Figure 2.3.

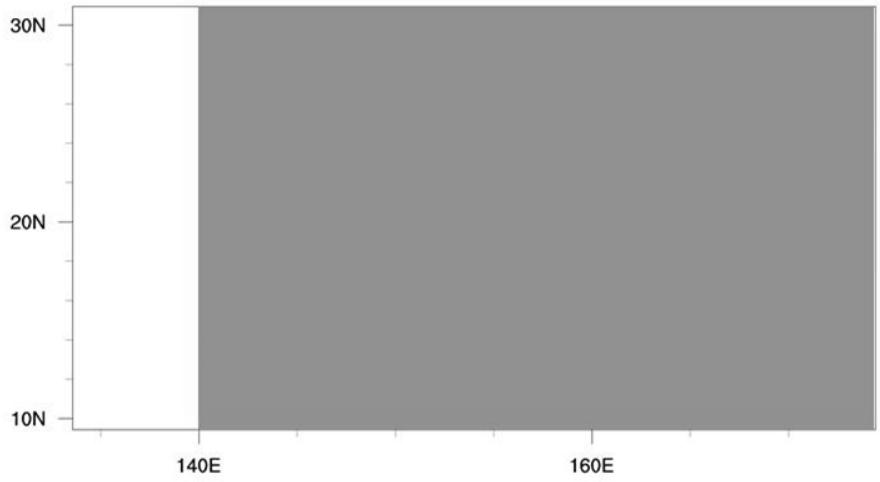


Figure 2.3: Domain of the idealized model.

The initial ocean state has a uniform temperature of 26°C and uniform salinity of 35 psu. Closed boundaries are used. As long as the domain is large enough and the simulation time is short enough, the boundary interferences are negligible. Experiments are halted at times to prevent reflections from the boundaries. The land mask is specified from the western boundary up to 140°E to simulate the coastline. A third-order upwind scheme is used for horizontal momentum advection, with a Smagorinsky-like viscosity applied [*Griffies and Hallberg*, 2000]. The momentum fluxes and air–sea heat fluxes are calculated by bulk formulae [*Fairall et al.*, 1996]. The background or minimum mixing is defined as 10^{-5} m^2 s^{-1} for momentum and 10^{-6} m^2 s^{-1} for tracers. Both shear and stratification are averaged horizontally before mixing rates are calculated. At the coastal wall, the normal velocity is zero while the tangential velocity is provided with the no-slip condition. The same applies to the ocean bottom. To ensure positive tracer concentrations, the Multidimensional Positive Definite Advection Transport Algorithm (MPDATA) is used [*Smolarkiewicz*, 1983]. The turbulence closure scheme used to calculate vertical mixing is based on the Generic Length Scale (GLS) parameterization as described by *Umlauf and Burchard* [2003] applying the k-ε

[*Rodi*, 1987], k-ω [*Wilcox*, 1988] and 'gen' scheme. This scheme solves equations (2.4) – (2.6) by determining the turbulent kinetic energy and turbulent length scale.

2.2.3 Set-up of the real-case ocean model

To compare the different processes affecting storm surges, a real case study is simulated in Chapter 5. The ROMS set-up uses a single grid at a horizontal resolution of 6 km in the domain as shown in Figure 2.4.

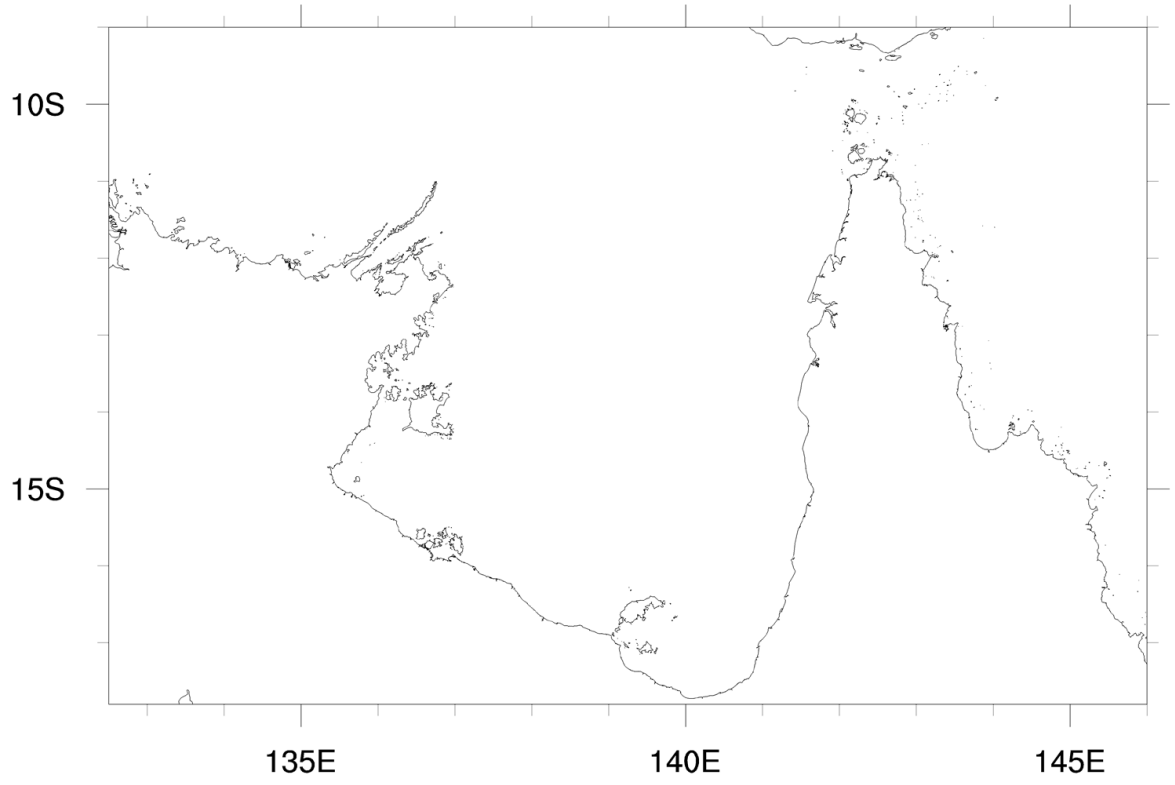


Figure 2.4: Domain of the real-case simulation

Open boundaries are employed, using the conditions by *Flather* [1976] for the barotropic velocities and the *Chapman* [1985] conditions for sea surface elevation. A minimum depth of 10 m and maximum depth of 5500 m is specified. 20 layers are chosen in the vertically stretched terrain-following sigma-coordinate, with higher resolution placed at the surface and

lower resolution placed at the bottom. Geometry of the bathymetry is obtained from Global Topography v14.1 [*Smith*, 1997]. The turbulent fluxes for wind, heat and moisture are computed using Monin-Obukhov similarity theory [*Liu et al.*, 1979] and the net longwave radiation is derived using the *Berliand and Berliand* [1952] formula. The tidal forcing is applied at the open boundaries and imposed on the elevation and the barotropic velocities. It is derived from 11 tidal harmonics that are extracted from the 1/12° resolution Pacific Ocean Atlas solution provided by the Oregon State University (OSU) Tidal Data Inversion (e.g. *Egbert et al.* [1994] and *Egbert and Erofeeva* [2002]). The analysis of these harmonics shows that the tidal forcing in the domain of this study is dominated by the semi-diurnal component M_2. The 1/12° resolution HYbrid Coordinate Ocean Model (HYCOM) [*Bleck and Boudra*, 1981] global daily analysis data is used as the initial, boundary and nudging conditions for the model. This is consistent with the approach of *Schiller et al.* [2011] in nesting coarser models into a data assimilation model to ensure proper modelling of shelf-to-offshore interactions. The HYCOM simulation employs the Navy Coupled Data Assimilation system (NCODA) [*Cummings*, 2005], which is an oceanographic version of the multivariate optimum interpolation technique commonly employed in atmospheric forecasting systems. The NCODA system assimilates satellite altimetry track-by-track and sea surface temperature directly from orbital data using model forecasts as the first guess [*Schiller et al.*, 2011]. A nudging relaxation zone with eight grids from the boundary is set up to relax the baroclinic structure to the forcing fields at the boundary [*Marchesiello et al.*, 2001]. The normal velocity is zero at the coastal wall and at the ocean bottom, while the tangential velocity is provided by the no-slip condition. To ensure positive tracer concentrations, the Multidimensional Positive Definite Advection Transport Algorithm (MPDATA) is used [*Smolarkiewicz*, 1983]. The *Orlanski* [1976] radiation conditions (additionally modified by *Raymond and Kuo* [1984]) impose a normal phase velocity on currents and tracers to radiate

out incoming and outgoing flow at the same boundary. For horizontal momentum advection, a third-order upwind scheme is used with a Smagorinsky-like viscosity is applied [*Griffies and Hallberg*, 2000]. The air–sea heat and momentum fluxes and are calculated by the bulk formulae as outlined by *Fairall et al.* [1996]. The background mixing is defined as 10^{-6} m^2 s^{-1} for tracers and 10^{-5} m^2 s^{-1} for momentum. The turbulence closure scheme used for vertical mixing is based on the Generic Length Scale (GLS) parameterization as described by *Umlauf and Burchard* [2003].

2.3 WRF model

WRF [*Skamarock et al.*, 2008] is a mesoscale Numerical Weather Prediction (NWP) model jointly created by the National Center for Atmospheric Research (NCAR), the National Oceanic and Atmospheric Administration (NOAA), the Air Force Weather Agency (AFWA), the Naval Research Laboratory (NRL), the University of Oklahoma, and the Federal Aviation Administration (FAA). The model is developed and supported for both research and operational applications across a range of physical scales from tens of metres to thousands of kilometres. Applications of WRF include real-time forecasting, regional climate modelling, idealized simulations, and data assimilation. WRF is currently in use operationally by NCEP, AFWA, and several other centres. It has a large worldwide community of about 25,000 registered users in over 130 countries.

There are two dynamical core variants of WRF, the WRF-Non-hydrostatic Mesoscale Model (NMM) and the Advanced Research WRF (ARW). NMM is a non-hydrostatic model that is currently in use for real-time NWP, forecast research, parameterization research, coupled model applications and teaching. It is supported by the Developmental Testbed Center (DTC). ARW is the hydrostatic branch of the WRF model and is supported by the NCAR

Mesoscale and Microscale Meteorology (MMM) Division. It has similar applications to NMM such as meteorological investigations, real-time NWP, idealized atmospheric simulations, data assimilation studies and development, coupling studies with other earth system models and modelling training.

The WRF model used in this study is the ARW-WRF model version 3.4. It is a fully compressible, Eulerian and non-hydrostatic model. Its vertical coordinate is a terrain-following hydrostatic pressure coordinate, with the top of the model being a constant pressure surface. WRF uses the Arakawa C-grid for the horizontal staggering of the horizontal velocities (U and V) and density (ρ) points as shown in Figure 2.5. The horizontal velocities are located at the west-east and north-south cell edges respectively and scalar quantities such as temperature (θ) are located at the centre of the cell. Compared to a WRF grid of the same domain size and resolution, ROMS has an additional row of V and ρ points at the start and end of the grid along the η direction and an additional row of U and ρ points at the start and end of the grid along the ξ direction. It is important to note that although both ROMS and WRF use the Arakawa C-grid for horizontal staggering, the ROMS grid will still be larger than the WRF grid by two V points and two ρ points in the η direction and by two U points and two ρ points in the ξ direction. The implication is that, for a set-up involving variables forced from WRF to ROMS, the WRF grid has to be at least two grid cells larger than the ROMS grid to ensure that the ocean variables in all the ocean grid cells are provided with a corresponding atmosphere variable. The WRF grid size also has to be larger than the ROMS grid size for a two-way coupling using COAWST. In two-way coupling, the forcing files for WRF include SST, so the WRF grid cells that do not receive SST updates from ROMS will obtain SST values from the forcing files. Conversely, ROMS is not provided with a separate atmospheric forcing file and it is fully reliant on WRF to provide all the atmospheric

variables. Nesting and grid refinement is also illustrated in Figure 2.3. Due to the staggering of the vector and scalar quantities in the C-grid, the grid size of the parent and child grids are recommended to be in the ratio 1:3 or 1:5 so the finer grid is interpolated onto the same staggering grid format as the parent grid, with the scalar quantities at the centre of the cell and the horizontal velocity points (*U* and *V*) located at the west-east and north-south cell edges respectively.

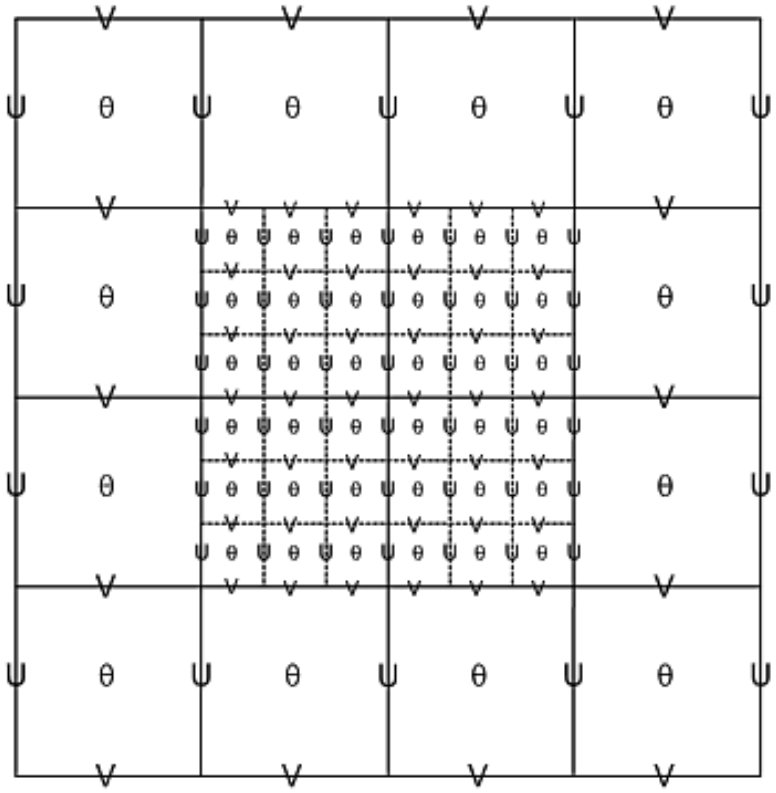


Figure 2.5: Arakawa C-grid staggering in WRF, showing the horizontal velocity points (*U* and *V*) and temperature (θ). A portion of a nested grid with 1:3 grid size ratio is shown with the solid lines denoting coarse-grid cell boundaries and the dashed lines denoting fine-grid cell boundaries.

There are various physics options available in WRF. The micro-physics in WRF offers several schemes to explicitly resolve water vapour, cloud and precipitation processes. The

cumulus parameterization used to represent the vertical fluxes as updrafts and downdrafts may not be resolved sufficiently at horizontal resolutions coarser than 5km. Land-surface schemes calculate the heat and moisture fluxes over land. Some of the variables used in these schemes include friction velocities, exchange coefficients from the surface layer scheme, radiative forcing from the radiation scheme and precipitation forcing from the microphysics and convective schemes. The planetary boundary layer scheme is not only responsible for the boundary layer physics, but for the eddy transport in the atmospheric column. It determines the profile of the fluxes in a well-mixed boundary and stable layer and temperature, moisture and horizontal momentum in the atmospheric column. The radiation schemes determine the heating in the atmosphere due to longwave and shortwave radiation. They are column, one-dimensional schemes that represent a good approximation if the vertical thickness is much smaller than the horizontal grid length. Upward longwave radiation is determined by surface emissivity and is dependent on the type of land use and skin temperatures.

2.3.1 Set-up of the idealized cyclone model

An idealized tropical cyclone simulated using WRF. This atmospheric state prescribes the atmospheric conditions required by ROMS. This is used in Chapter 3 to isolate the effects of rain mass and rain stress. The idealized tropical cyclone is set up using the 10-m wind field as described by *Chan and Williams* [1987]:

$$V(r) = V_m\left(\frac{r}{r_m}\right)e^{\frac{1}{b}\left(1-\frac{r}{r_m}\right)^b} \tag{2.13}$$

where V is velocity, r is radius from the centre of the vortex, r_m is the radius of maximum wind, V_m is V(r) at the radius of maximum wind and is the factor that determines the shape of the wind profile. Here, the radius of the maximum wind (r_m) is set to 75 km, the velocity at

the radius of maximum wind (V_m) is set to 75 m/s and the factor determining the shape of the wind profile (b) is set to 0.33 [*Hill and Lackmann*, 2009].

The vertical structure of the wind field is obtained by decaying the horizontal wind field linearly with height [*Rotunno and Emanuel*, 1987]. The environmental sounding profile is obtained from the mean tropical sounding during the tropical cyclone season from July to October [*Jordan*, 1958]. A background flow of -4 m/s is introduced to translate the cyclone westward. After the initial vortex has been introduced to the environment, the temperature, geopotential heights and pressure perturbations are replaced. The temperature field is calculated from thermal wind balance, the geopotential heights are set in terms of gradient wind balance and the pressure perturbations are calculated from the hydrostatic equation [*Kwok and Chan*, 2005]. Here, relative humidity is fixed and the specific humidity varies with the temperature and pressure changes. One single nest is set up with 31 vertical levels and a horizontal resolution of 15 km in the domain spanning 5°N to 35°N and 120°E to 180°E. The model is run for 8 days and the following variables are extracted as forcing variables for ROMS: U-component of wind speed, V-component of wind speed, pressure, specific humidity, rainfall rate, solar shortwave downward radiation and downward longwave radiation. In order to set up an idealized ocean model that can isolate the effect of wind and precipitation, the other atmospheric forcing variables are set to a nominal and constant value. In addition, the rainfall output from WRF is formatted as a rain mass forcing file for ROMS to incorporate the effects of rain mass. The microphysical parameterization used is based on *Lin et al.* [1983]. The scheme is from the Purdue cloud model [*Chen and Sun*, 2002] and includes six hydrometeor classes. Cumulus parameterization is not included, which reduces the computational time required, for each simulation. Without cumulus parameterization, the amount of precipitation may be underestimated with a horizontal resolution coarser than 5 km. However, the aim of the study is to understand the specific effect of adding precipitation

mass to the ocean model in a simple, idealized set-up, and not to reproduce the real physical environment. The surface layer scheme is based on Monin-Obukhov with Zilitinkevich thermal roughness length and standard similarity functions [*Paulson*, 1970]. Planetary boundary layer processes are parameterized using the Mellor-Yamada-Janjic scheme [*Janjic*, 1994]. The longwave and shortwave radiation schemes are implemented from *Mlawer et al.* [1997] and *Dudhia* [1989] respectively.

2.3.2 Set-up of the real-case atmosphere model

The WRF model is used to simulate a high resolution atmospheric state of tropical cyclone Monica. This atmospheric state prescribes the atmospheric conditions required by the ocean model used in the case study in Chapter 5. Two nests are employed with 28 vertical levels. The parent grid is set up with a horizontal resolution of 18 km that is interpolated from CFSR reanalysis data at a 0.5° resolution. The final grid has a horizontal resolution of 6 km. Several sets of physics configurations are simulated to obtain the set of physics options that yield the best results when validated against observations. From the WRF output, the U-component of wind speed, V-component of wind speed, pressure, specific humidity, rainfall rate, solar shortwave downward radiation and downward longwave radiation are extracted and reformatted as forcing variables for ROMS. In addition, the rainfall output from WRF is formatted as a rain mass forcing file for ROMS to incorporate the effects of rain mass. The WRF model uses the ETA scheme [*Rogers et al.*, 2001] for microphysical parameterization. The Kain-Fritsch cumulus parameterization scheme [*Kain*, 2004] has been used for both nests. The surface layer scheme is based on Monin-Obukhov with Carslon-Boland viscous sub-layer and standard similarity functions. The selected planetary boundary layer from Yonsei University [*Hong et al.*, 2006] includes an explicit term in the treatment of the

entrainment layer and uses a buoyancy profile at the top of the planetary boundary layer. The Mesoscale Model 5 (MM5) 5-layer thermal soil temperature model [*Dudhia*, 1996] is used to calculate the heat and moisture fluxes over the land. This soil temperature model assumes no horizontal interaction and is regarded as a one-dimensional column model. The longwave and shortwave radiation schemes are implemented from *Mlawer et al.* [1997] and *Chou and Suarez* [1994] respectively. NCEP Climate Forecast System Reanalysis (CFSR) [*Saha et al.*, 2010] has been used for initial and lateral boundary conditions. The 3D fields include temperature, relative humidity and the horizontal components of momentum. The 2D static fields include albedo, Coriolis parameter, terrain elevation, land-use type, land and water mask, map scale factors, map rotation angle, soil texture category, vegetation greenness fraction, annual mean temperature, latitude and longitude. The 2D time-dependent fields include surface pressure, sea-level pressure, soil temperature and moisture, snow depth, skin temperature, sea surface temperature and sea ice flag. The boundary forcing is prescribed every 6 hours and the model interior is allowed to evolve freely.

3 The effect of precipitation mass and momentum

3.1 Introduction

Surface freshwater sources such as rivers and rainfall are considered to be important drivers of ocean circulation. While the effect of freshwater mass from rivers is more commonly studied, the effect of mass from rainfall is widely neglected. This is expected, considering that many ocean circulation models and storm surge models do not incorporate the effect of rain mass. Ocean models such as ROMS and FVCOM only incorporate the temperature and salinity effects of rain, but not the effect of rain mass. Storm surge models such as ADCIRC and SLOSH ignore the effects of rain entirely. While it may be reasonable to neglect rain mass when considering typical rain rates over the vast ocean domain, highly precipitating storm events with extreme rain rates may raise the sea surface height substantially. Chapter 2 discusses how a new rainfall scheme has been set-up in ROMS to account for the effect of rain mass. This scheme will complement the existing routine in ROMS that calculates temperature and salinity changes due to rainfall. An idealized set-up of ROMS will be used to isolate the effects of adding rain mass to the sea surface height. To understand the effect of rain mass on sea surface height in the context of storm surges, an idealized tropical cyclone is generated using WRF. The rainfall from the idealized tropical cyclone is used to force ROMS and the effect on the sea surface height is evaluated. This section serves as a validation of the newly implemented rainfall scheme and to check that that the model is behaving as expected.

In the next section, the transfer of momentum from raindrops to the water surface will be investigated. Rain stress was first documented by *Van Dorn* [1953], who concluded that the stress contributions from rainfall can considerably intensify surface stresses. *Caldwell and*

Elliott [1970] have since built on his work, parameterizing rain stress as a function of rain rate and wind speed. This parameterization has been widely incorporated in many model studies such as the one-dimensional mixed layer model developed by *Clayson and Kantha* [1999] and the bulk parameterization relating the near-surface atmospheric to the oceanographic bulk variables [*Fairall et al.*, 1996]. This air-sea bulk parameterization has also been adopted in ROMS. While the parameterization of rain stress has been widely adopted, there has been no study so far that shows its isolated effect in the models it has been implemented in. For the case of tropical cyclones, where extreme wind speeds and precipitation rates are involved, the isolated effect of rain stress has never been shown and its contribution to storm surges is not known. This chapter shall employ the use of an idealized set-up in ROMS to show the isolated effects in the context of storm surges.

3.2 Short term response to rain mass

In order to isolate the SSH response to rain mass, an idealized model of ROMS is set up as outlined in Section 2.2.2. To isolate the effects of rainfall, the wind field is set to zero and all other atmospheric forcings are set to a constant nominal value. One centimetre of rain is introduced to a single grid cell (15 km by 15 km) for 1 hour, to study the effect of a single-point perturbation on the free surface. The rain is added to the centre of the domain at the location 20°N 150°E. Figure 3.1 shows the ocean surface response after 2 hours and 9 hours. Once the perturbation is introduced, a surface gravity wave is generated, propagating radially outwards from the point of perturbation. At time = 2 h, the maximum SSH is 0.0094 cm, the minimum is -0.0078 cm and the horizontal extent that it has propagated to is about 2° from the initial point of perturbation. At time = 9 h, the maximum SSH is 0.0020 cm, the minimum

is -0.0014 cm and the wave propagates to about 10° from the initial point of perturbation. Over 9 hours, the amplitude of the gravity wave drops by about 80%.

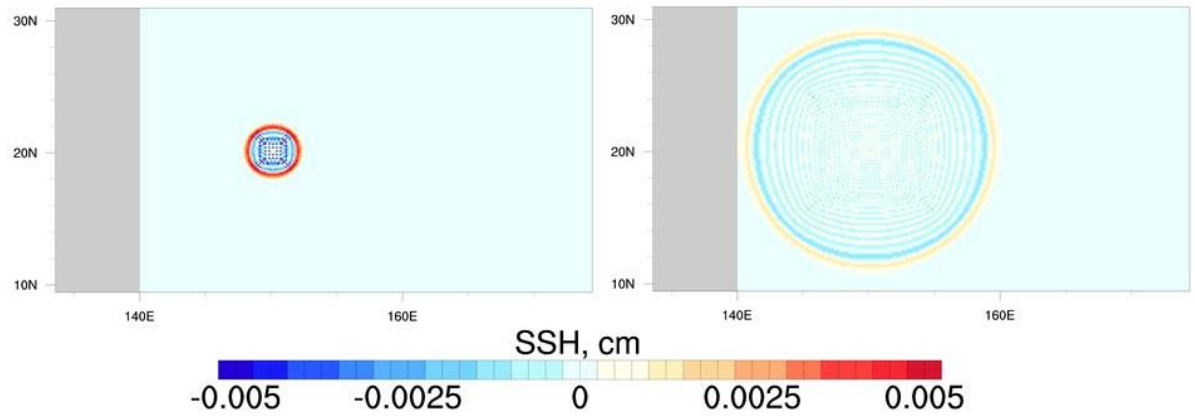


Figure 3.1: SSH response to a drop of rain on a single surface grid cell after 2 hours (left) and 9 hours (right).

3.3 Longer term response to rain mass

Next, the SSH response to rainfall over a longer time scale is studied by forcing ROMS with rainfall from an idealized tropical cyclone simulated using WRF over 8 days. The idealized tropical cyclone has been detailed in Section 2.3.1. At the first time-step, the rainfall rate is up to 5 mm/day and confined to a relatively small area of about 1° (8 cells). A small vertical velocity is generated at the surface-most cell and is in the range of 10^{-6} m/s. The maximum rain rate is not at the centre of the cyclone, but along the rain bands. The cyclone gradually grows in size and intensity as it treks from the east to the west of the domain. The rain bands of the tropical cyclone also increase in size with time. Figure 3.2 shows the cumulative rainfall throughout the event, with a maximum of 319 mm at any one grid point. To avoid any interference from the winds, the wind field is set to zero so the sea surface is unaffected by wind stress and responds only to the cyclone rainfall.

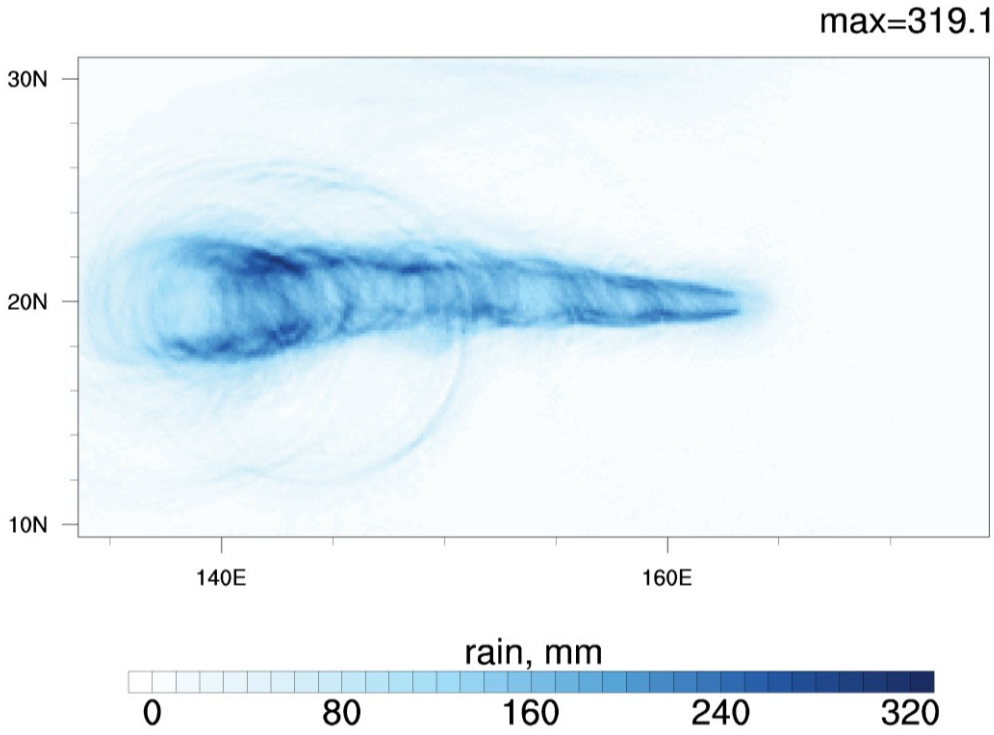


Figure 3.2: Cumulative rainfall of the idealized tropical cyclone over 8 days.

The SSH response to rainfall from the idealized tropical cyclone is compared between an ocean 100 m and 1000 m deep. Figure 3.3 shows the sea surface height at the 170th hour of the simulation when the tropical cyclone makes landfall at the coastline along 140°E. For both depths, the SSH increases along the rainfall path, gradually decreasing towards the domain boundaries. For the case with a depth of 100 m, the maximum SSH is 5.8 cm and the minimum SSH is 1.3 cm at the 170th hour. Through geostrophic adjustment, a clockwise gyre is formed, where the sea surface currents have a magnitude of 10^{-2} m/s. Figure 3.4 shows the SSH response along the coastline, with the SSH to the north of 20°N (up to 1.3 cm) lower than the SSH to the south (up to 2.7 cm). For the case with a depth of 1000 m, the maximum SSH is 3.2 cm while the minimum SSH is 2.3 cm. A weaker clockwise gyre is formed with the sea surface currents reduced to a magnitude of 10^{-3} m/s.

(a) (b)

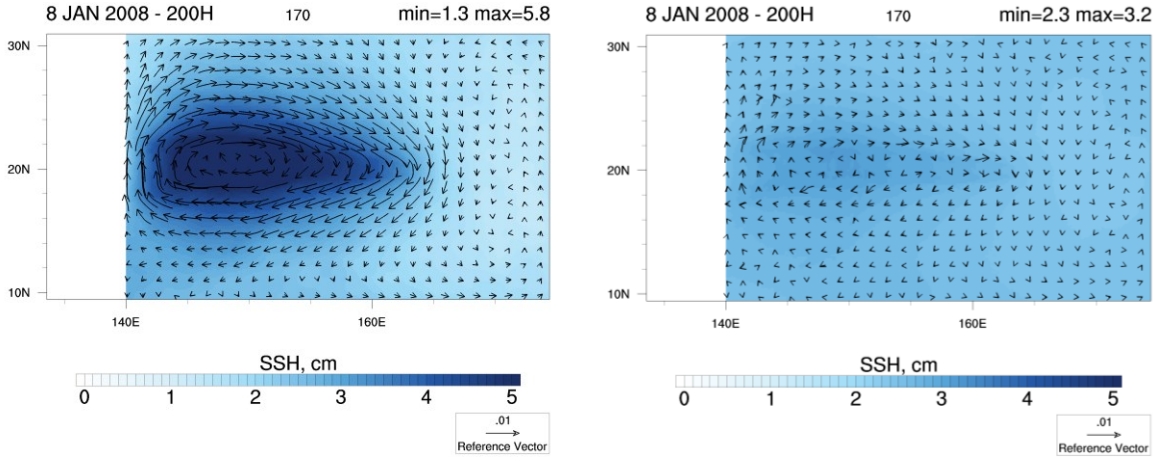


Figure 3.3: SSH and sea surface current response to the rain mass added to the ocean with (a) 100 m depth and (b) 1000 m depth. The reference vector is 0.01 m s^{-1}.

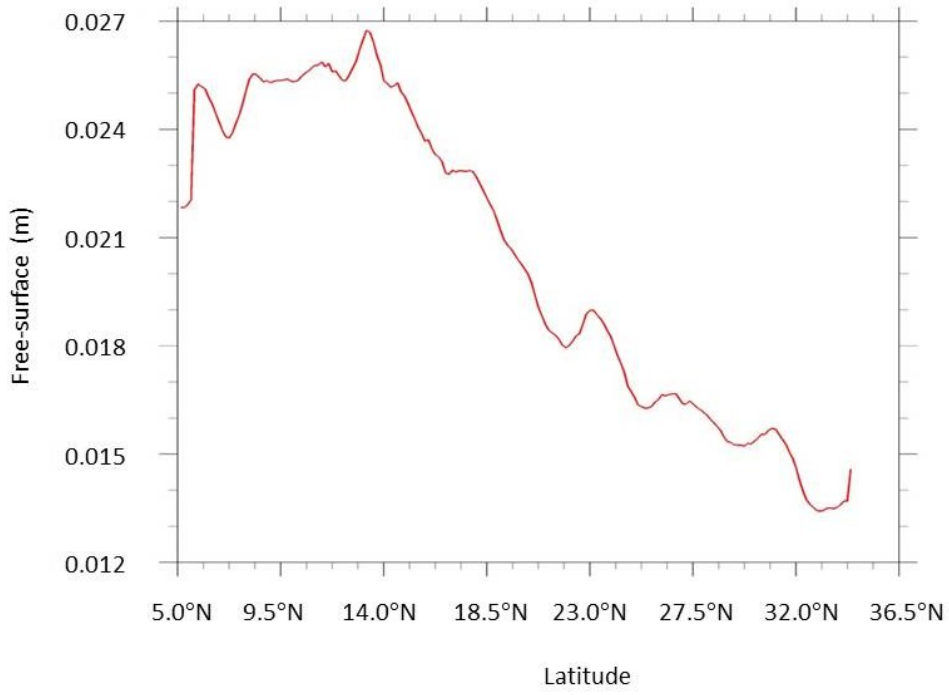


Figure 3.4: SSH response to rain mass against latitude along the coast at 170th hour for the ocean set-up with 100 m depth.

The various components of horizontal momentum from equations (2.1) and (2.2) are examined at different depths. The momentum components include Coriolis term, pressure gradient, horizontal advection, vertical advection, horizontal viscous term and vertical viscous term. Throughout the depth of 100 m, the Coriolis term and the pressure gradient terms are dominant. An example of the u-momentum contributions at the point 20°N 141°E against the water depth are shown in Figure 3.5. Here, the u-component of the pressure gradient is in the negative x direction and the Coriolis force is in the opposite direction. At the surface, the pressure gradient force (u-component) is almost exactly balanced by the Coriolis force (u-component) and there is a small net acceleration (u-component) towards the coast. At the bottom, the Coriolis force (u-component) is slightly larger than the pressure gradient force (u-component) and there is a net acceleration (u-component) away from the coast.

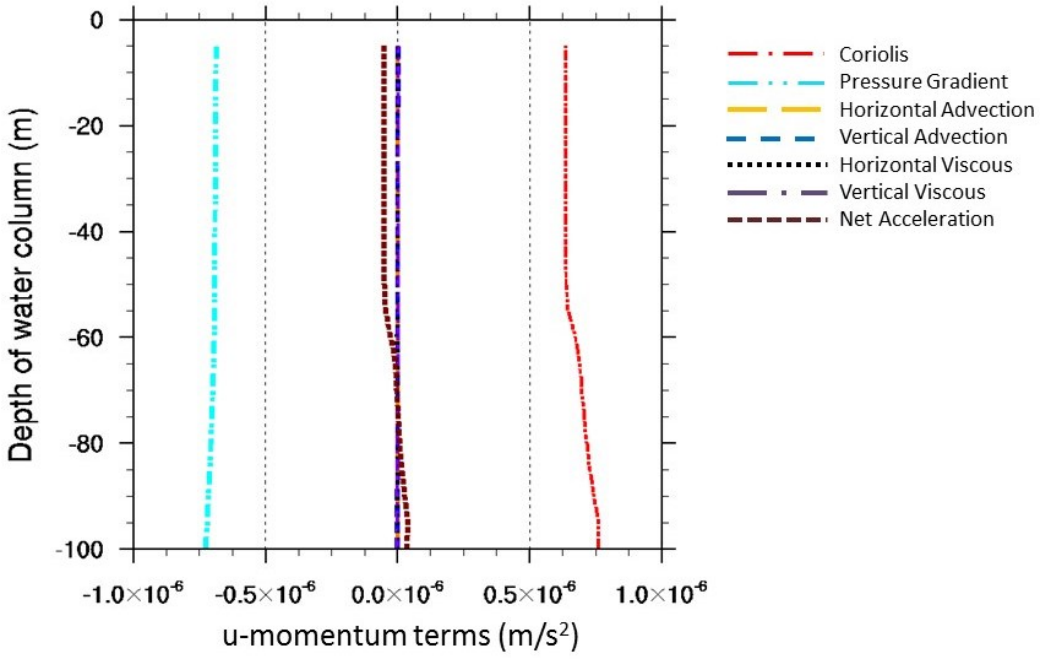


Figure 3.5: u-momentum terms through the ocean depth at the point 20 °N 141 °E.

Figure 3.6 and Figure 3.7 show geostrophic balance between the pressure gradient and Coriolis terms at the surface and bottom of the ocean respectively. The results are shown at the 170th hour and superimposed onto the SSH contour plot. The magnitudes at the bottom are slightly smaller than the magnitudes at the surface, but the directions are very similar. The pressure gradient force is outwards from the location where the rain is added towards the boundaries of the domain. The Coriolis force is in the opposite direction to the pressure gradient force and acts inwards from the boundaries of the domain towards the centre where the rain is added.

(a) (b)

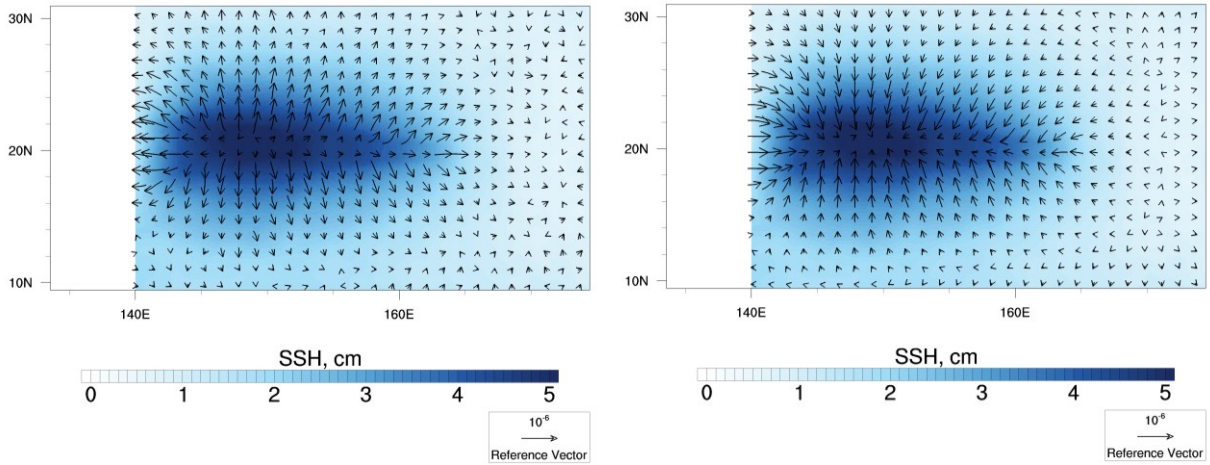


Figure 3.6: Surface momentum terms (vector field) superimposed onto SSH, showing (a) pressure gradient term (b) Coriolis term. The reference vector is 1 x 10^{-6} m s^{-1}.

(a) (b)

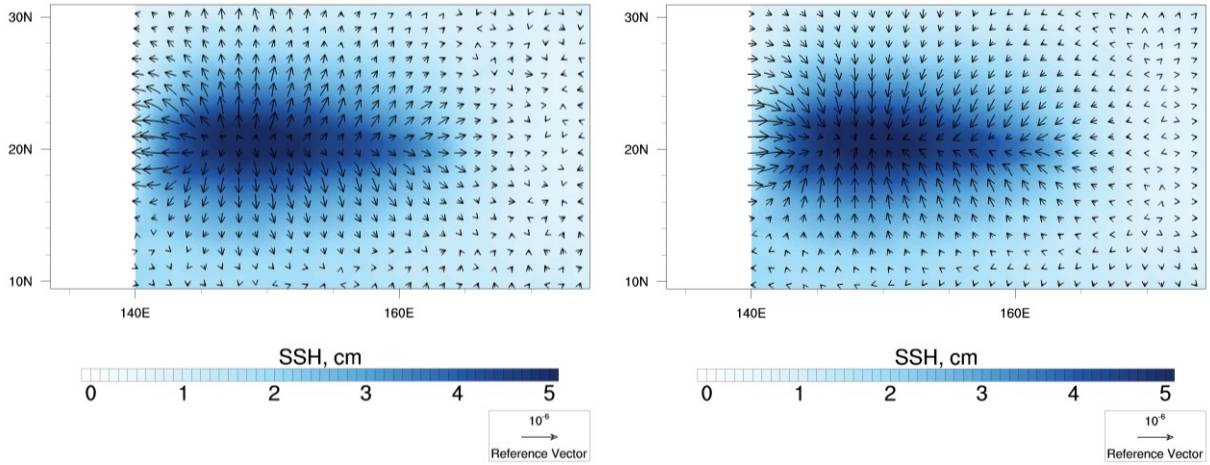


Figure 3.7: Bottom momentum terms (vector field) superimposed onto SSH, showing (a) pressure gradient term (b) Coriolis term. The reference vector is 1 x 10^{-6} m s^{-1}.

To further investigate the asymmetrical spreading of the rain mass shown in Figure 3.4, a single pulse of rain from the 160th hour is introduced to the water body. The spatial distribution of the rainfall introduced in this experiment is shown in Figure 3.8. In Figure 3.9, a surface gravity wave can be seen propagating outwards towards the domain boundaries. The rain mass spreads out more towards the south of 20 °N compared to the north of it, with both the crests and troughs to the south of 20°N higher than the crests and troughs to the north of 20°N. The same experiment is repeated but with the Coriolis parameter set to zero (Figure 3.10). Here, the rain mass propagation is symmetrical along 20°N and the crests and troughs of the wave are of similar magnitude.

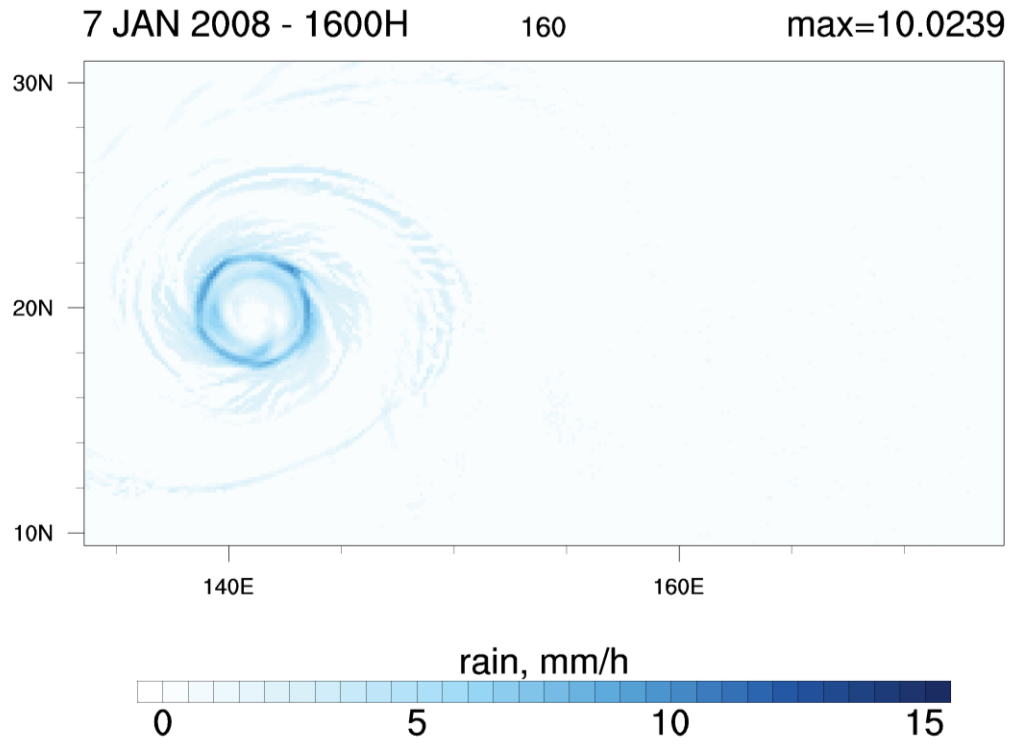


Figure 3.8: Rain input at the 160th hour; cyclone making landfall at 140°E.

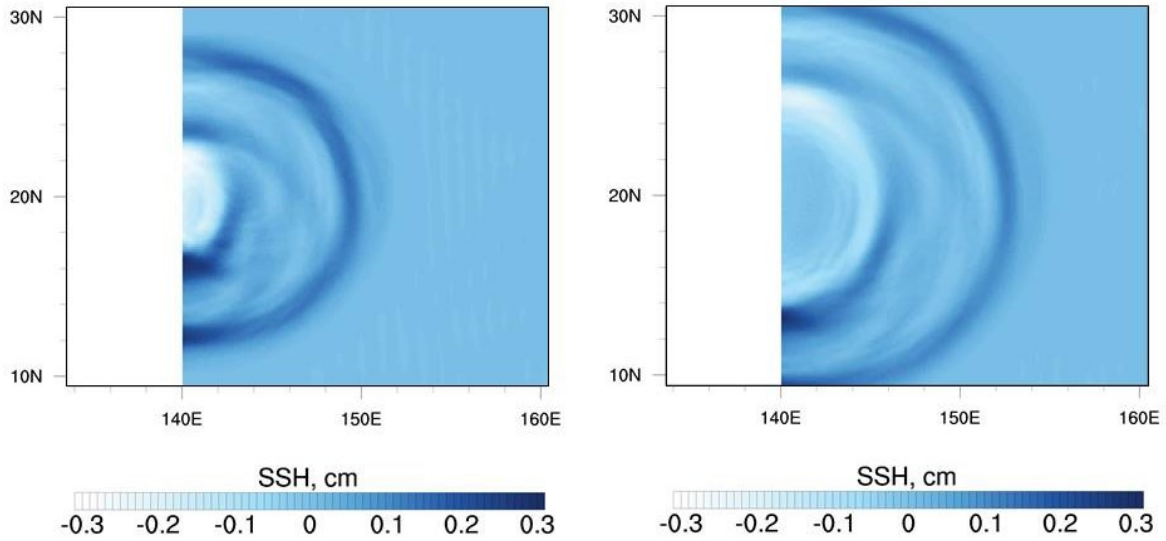


Figure 3.9: SSH response from introducing a single burst of rainfall at t = 160 h. Different time-frames show (left) t = 166 h and (right) t = 169 h.

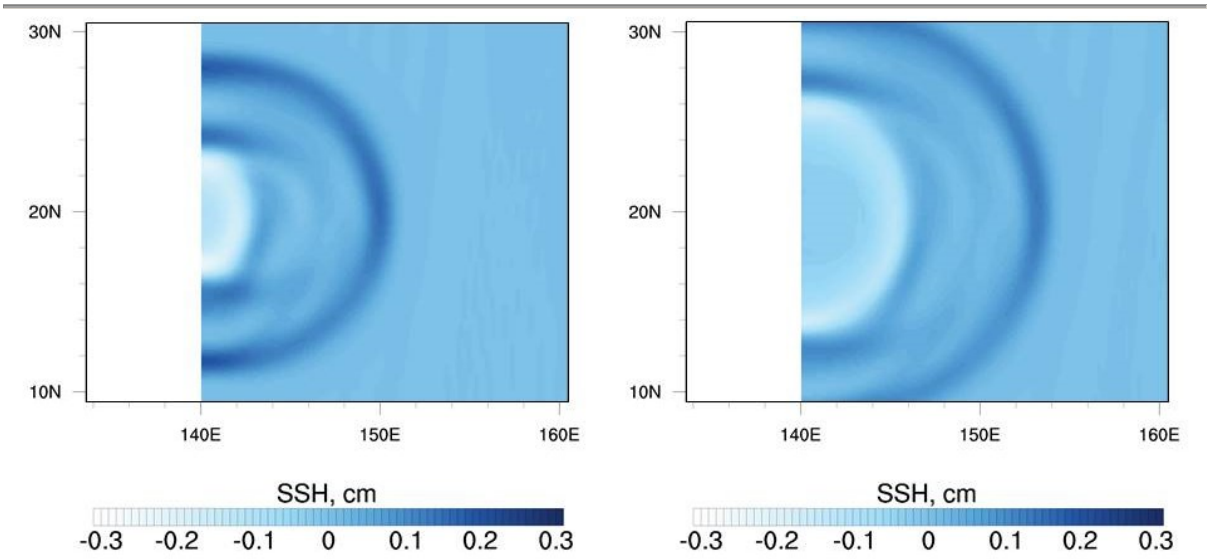


Figure 3.10: SSH response from introducing a single burst of rainfall at t = 160 h. Different time-frames show (left) t = 166 h and (right) t = 169 h. Here, the Coriolis parameter has been set to zero.

3.4 Impact of rain mass on temperature and salinity

Finally, the two methods of introducing rainfall to the model are examined separately to show that the methods can and should be used simultaneously. The first method is used in the existing implementation in ROMS, where rainfall rates are read in by the model and its temperature and salinity effects are considered. However, the rainfall mass is ignored. The second method is the new rain scheme that has been described in Section 2.2.1. The new rain scheme implements rainfall as point sources, adding mass to the system. Since temperature and salinity effects are already considered in the existing implementation of ROMS, temperature and salinity levels are not further prescribed here. Rainfall should ultimately be specified using both methods concurrently to consider mass, temperature and salinity effects.

The idealized tropical cyclone outlined in Section 2.3.1 is used to force the idealized ocean set-up described in Section 2.2.2. The initial SST is 25 °C, SSS is 35.0 psu and SSH is 0 m. With the air temperature set to 26 °C, the SST rises slightly through the simulation to an average of 25.25°C. Two simulations are conducted. To isolate the effect of rainfall, the winds are set to zero and other atmospheric forcings are set to a constant value. The first simulation uses the existing implementation for rainfall in the ROMS model. Rainfall is introduced using a regular forcing file and ROMS considers the temperature and salinity changes from rain, but not its mass. Figure 3.11a shows the SST response to the cooler rainfall, falling to a minimum of 24.03°C. In the absence of wind, there is little spreading and the colder temperature signal closely follows to the rainfall path. There is a freshening effect as shown in Figure 3.12a, with SSS levels dropping as low as 33.2 psu. Similar to the temperature signal, the salinity signal remains close to the path of the rainfall in the absence of wind. There is a small SSH increase of up to 0.004 m as shown in Figure 3.13a. The location of SSH increase is similar to the position of the temperature and salinity response. There is a very small current (of a magnitude of $\sim 10^{-3}$ m/s) generated largely along the rainfall path, as well as sporadic locations around the domain where rainfall is introduced.

The second simulation uses the point source implementation of rainfall in ROMS. Here, the regular rainfall forcing file is set to zero so the temperature and salinity effects are not considered. An additional forcing file is created to specify point sources to account for the mass effect of rainfall. Figure 3.11b and Figure 3.12b shows the SST and SSS response at the 170^{th} hour. The temperature and salinity changes from the ambient conditions are very small, up to 0.02°C and 0.1 psu. The SSH signal is substantial, reaching heights of up to 5.8 cm (Figure 3.13b). The rain mass spreads outwards from the rainfall path towards the boundaries.

A distinct clockwise gyre is formed and the sea surface currents are of a magnitude of 10^{-2} m/s.

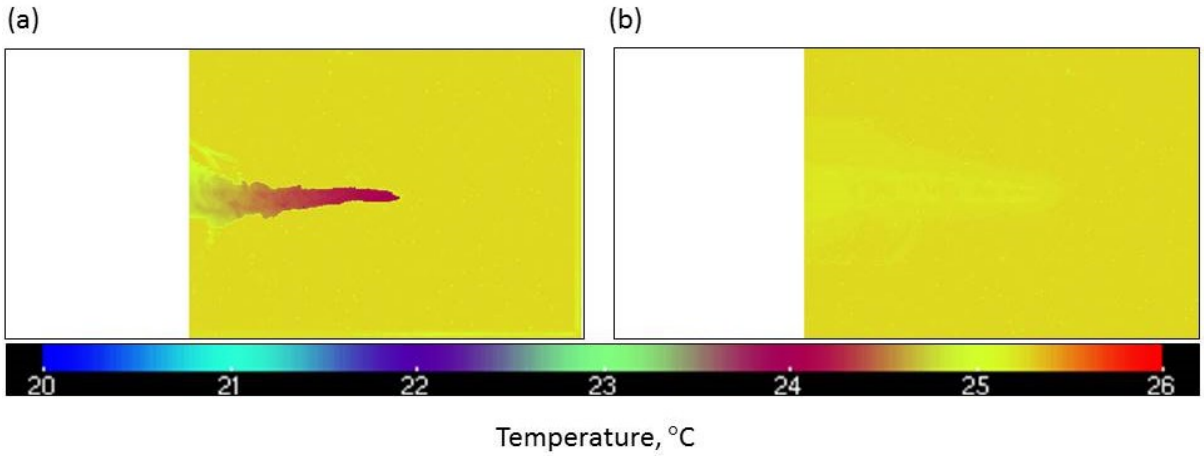


Figure 3.11: SST for (a) the existing implementation with rain forcing but without rain point sources (min SST = 24.03 °C) and (b) the point source implementation of rain without rain forcing (min SST = 25.23 °C).

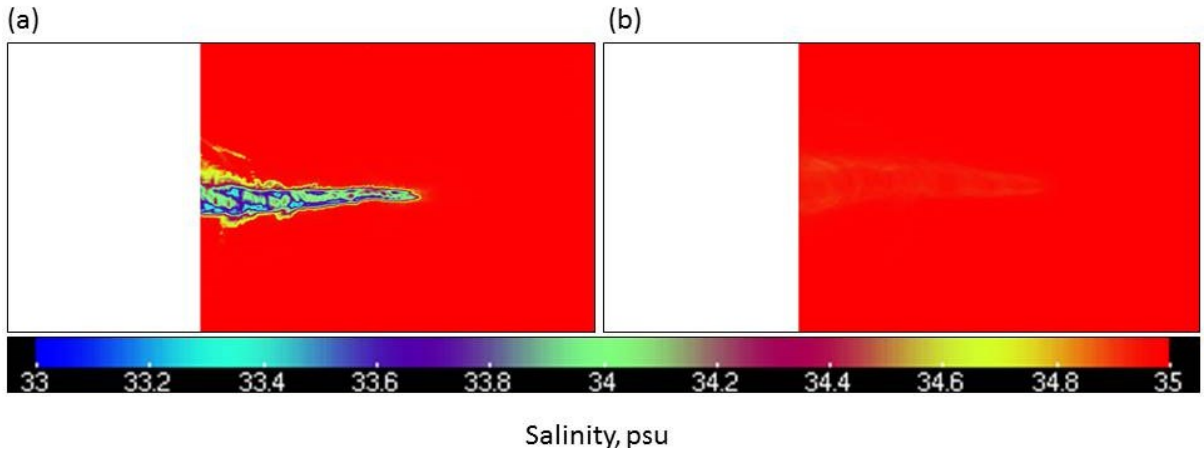


Figure 3.12: SSS for (a) the existing implementation with rain forcing but without rain point sources (min SSS = 33.15 psu) and (b) the point source implementation of rain without rain forcing (min SSS = 34.90 psu).

(a) (b)

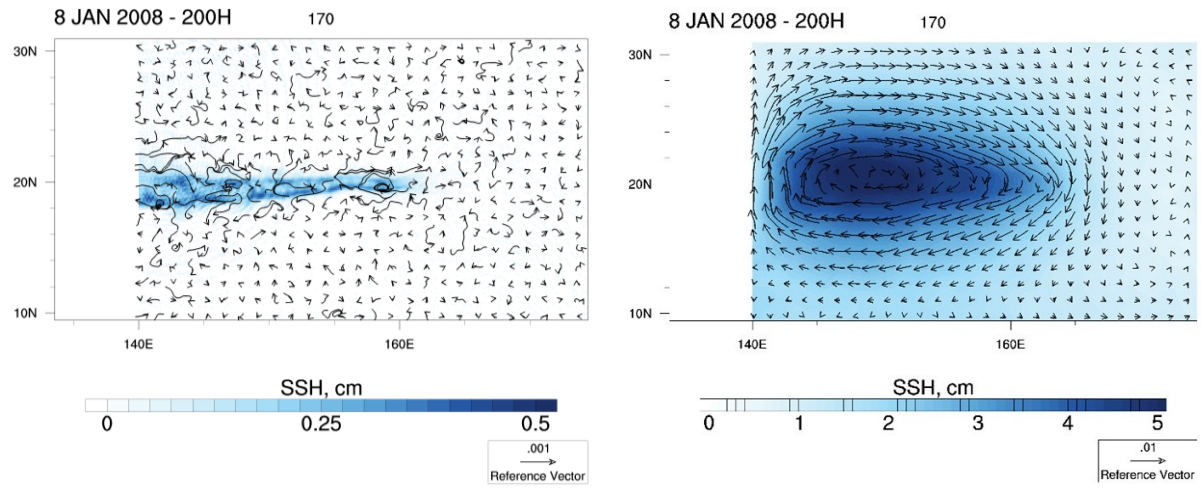


Figure 3.13: Sea surface currents superimposed onto SSH for (a) the existing implementation with rain forcing but without rain point sources (max SSH = 0.4 cm) and (b) the point source implementation of rain without rain forcing (max SSH = 5.8 cm). Different scales have been used in (a) and (b). The reference vector is 0.01 m s^{-1}.

The previous sections dealt with how rain mass is incorporated into ROMS and how ROMS respond to the effect of rain mass. The upcoming sections shall examine the rain stress formulation in ROMS and the necessary corrections that were made to the code.

3.5 Corrections to ROMS' implementation of rain stress

In ROMS, rain stress is implemented in the bulk fluxes routine from *Fairall et al.* [1996] and is based on the parameterization by *Caldwell and Elliott* [1970] as follows:

$$\tau_x = \tau_{wx} + 0.85R\rho_r|\vec{v}_{10}| * SIGN(U_{10}) \quad (4.1)$$

$$\tau_y = \tau_{wy} + 0.85R\rho_r|\vec{v}_{10}| * SIGN(V_{10}) \quad (4.2)$$

where τ_x is the total surface stress in the x direction, τ_{wx} is the wind stress in the x-direction, $SIGN(U_{10})$ denotes the sign of U_{10} (U-component wind speed at 10 m), τ_y is the sum of wind stress and rain stress in the y direction, τ_{wy} is the total surface stress in the y-direction and $SIGN(V_{10})$ denotes the sign of V_{10} (V-component wind speed at 10 m).

This implementation sums the wind and rain stresses together in their respective U and V components. The direction of the U and V wind components is considered for the rain stress, which will correspond to an increase or decrease in the magnitude of the overall surface stress. However, the rain stress parameterization of *Caldwell and Elliott* [1970] is derived from a one-dimensional model where $\vec{v}_{10}$ refers to the wind velocity in the direction of reference (Section 1.2.4). When considering wind velocity resolved in the U and V components, it would be incorrect to utilize the total velocity in calculating the rain stress. This results in a systematic overestimation of rain stress and an incorrect direction calculated for the overall wind stress.

The corrected implementation of the rain stress parameterization is as follows:

$$\tau_x = \tau_{wx} + 0.85R\rho_r u_{10} \quad (4.3)$$

$$\tau_y = \tau_{wy} + 0.85R\rho_r v_{10} \quad (4.4)$$

With this correction, the direction and magnitude of the rain stress will be consistent with the x and y stress components.

For the experiments carried out to isolate the effect of rain stress in the model, a control experiment is set up with modifications to the ROMS code to exclude the rain stress and include only the wind stress as follows:

$$\tau_x = \tau_{wx} \quad (4.5)$$

$$\tau_y = \tau_{wy} \quad (4.6)$$

3.6 Point source response to rain stress

An idealized model is used to verify the corrected implementation of rain stress. The model set-up is detailed in Section 2.2.2. The domain spans 5°N to 35°N and 120°E to 180°E, with a horizontal resolution of 15 km. Here, the u-component wind is set to a constant -1 m/s and the v-component wind is set to zero. One centimetre of rain is introduced to a single cell (15 km by 15 km) in the centre of the domain (20°N 150°E) for 1 hour. Two runs are conducted to compare the existing implementations of rain stress (using equations (4.1) and (4.2)) and the corrected implementation of rain stress (using equations (4.3) and (4.4)). Both the runs are subtracted from a control run using equations (4.5) and (4.6) to eliminate any noise such as the SSH response to the background u-component wind. Figure 3.14 shows the

perturbation setting off a surface gravity wave that propagates outwards from the point of perturbation towards the domain boundaries.

(a) (b)

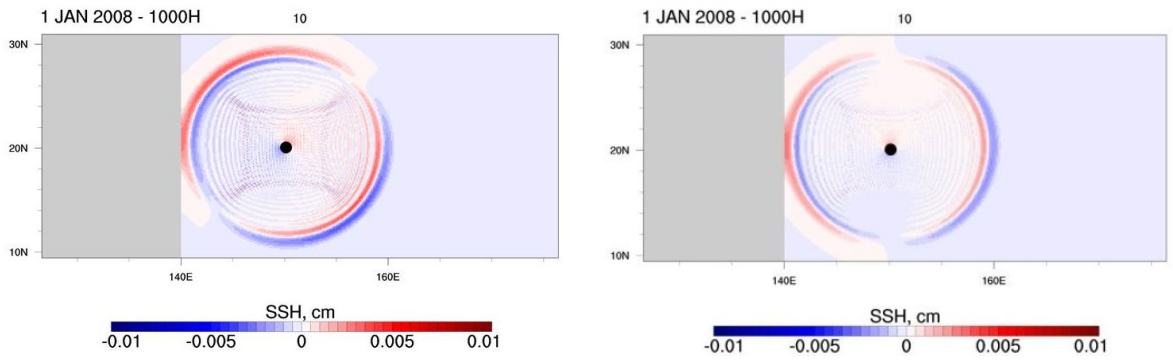


Figure 3.14: Sea surface height at 10 hours after introducing a rain stress perturbation for (a) the existing implementation of rain stress in ROMS and (b) the corrected implementation of rain stress in ROMS. The black dot in the centre of the domain (20°N 150°E) denotes the initial position of perturbation.

In the existing implementation of rain stress (Figure 3.14a), the resulting surface gravity wave is at an angle of 45° to the wind direction. The front of the wave is led by a crest in the north-westward direction with an amplitude up to 0.01 cm. In the south-eastward direction, the wave is led by a trough of up to 0.01 cm in amplitude. Figure 3.14b shows the SSH response to the corrected implementation of rain stress in ROMS. The surface gravity wave generated from the rain stress perturbation is now symmetrical to the wind direction. In the westward direction, the front of the wave is led by a crest of up to 0.005 cm in amplitude. In the eastward direction, the wave is led by a trough of up to 0.005 cm in amplitude.

3.7 Effect of rain stress on storm surges

Next, the contribution of rain stress to storm surges is investigated by forcing ROMS (set-up discussed in Section 2.2.2) with an idealized tropical cyclone simulated using WRF (set-up discussed in Section 2.3.1). Here, the wind and rainfall fields are retained, but the other forcing fields are set to a nominal and constant value in order not to introduce interfering signals into the system. To show the isolated effect of rain stress, two runs are conducted. The control simulation ignores the effect of rain stress by using equations (4.5) and (4.6) in ROMS to calculate the total surface stress. The rain stress simulation includes the effect of rain stress by using equations (4.3) and (4.4) in ROMS to calculate the total surface stress. Figure 3.15 shows the response of SSH sea surface currents from the rain stress simulation that has been subtracted from the control simulation, at the time where the cyclone makes landfall (t = 163 h). Here, an anticlockwise circulation centering 20°N 141°E is generated with a decrease in SSH at the circulation centre. Along the coastline at 140°E, the magnitude of the negative surge is larger than the positive surge. The positive surge is up to +0.44 cm and the negative surge is up to -0.63 cm.

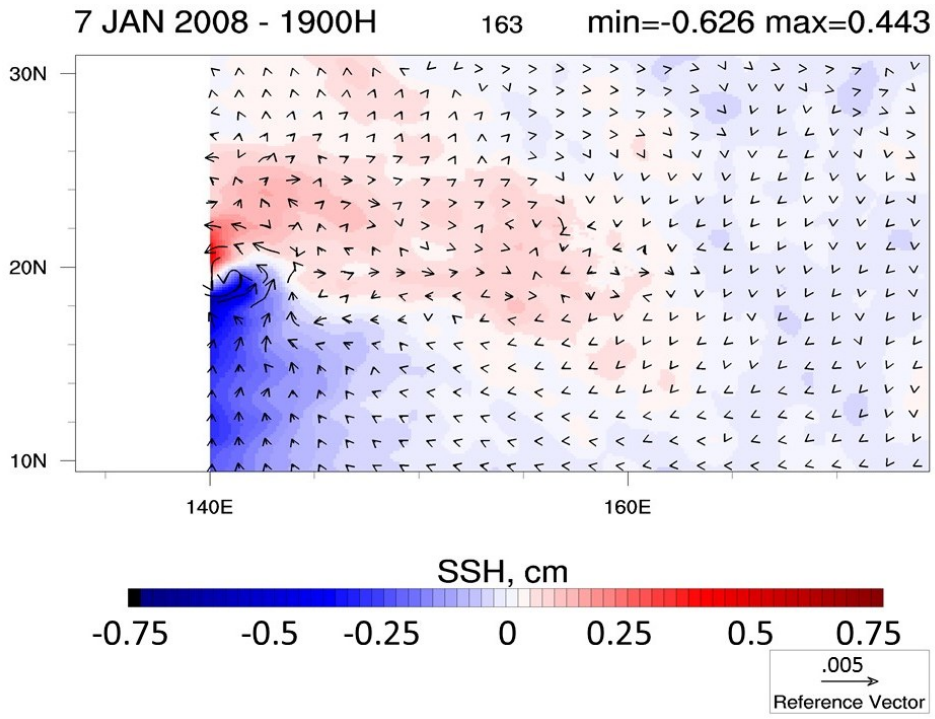


Figure 3.15: Response of SSH and sea surface currents to rain stress at t = 163 h.

3.8 Discussion

In

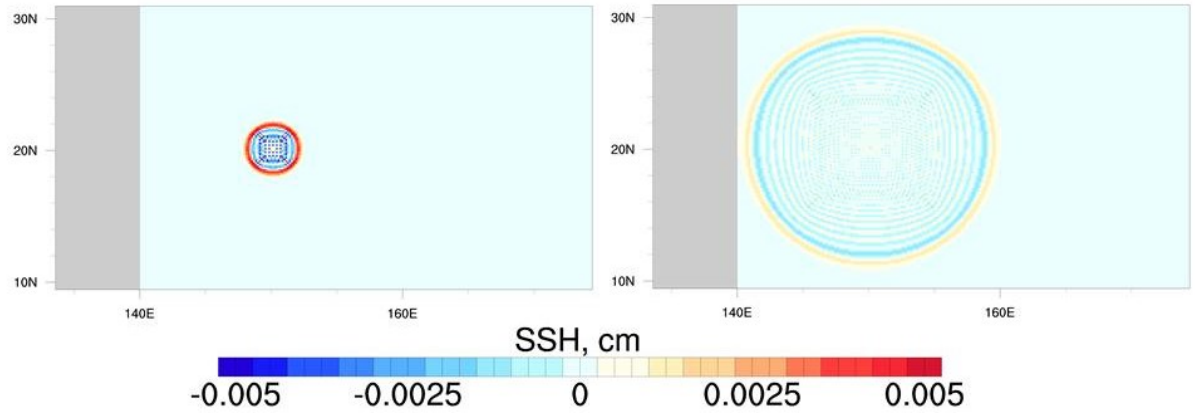


Figure 3.1, the point perturbation on the water surface sets off a surface gravity wave propagating outwards towards the domain boundaries over a time scale of several hours. A surface gravity wave is generated when a perturbation to the water surface causes water to

rise above the equilibrium water level and gravity acts on it to pull it back to the equilibrium position. Due to the displacement of water above the equilibrium water level, a pressure gradient and horizontal motion is created. This causes an adjacent surface rise above the equilibrium water level and a travelling wave starts propagating outwards from the point of perturbation.

Characteristics of surface waves are inherently non-linear. But considering a straight canal of uniform depth and assuming the amplitude of the surface waves to be infinitely small such that the surface is essentially a plane, and that there are no limits to the horizontal boundaries, the wave frequency (ω) of the surface wave can be expressed as follows [*Lamb*, 1895]:

$$\omega^2 = gktanh(kd) \tag{3.1}$$

where g is the gravitational acceleration, k is the wave number and d is the water depth.

For shallow water approximations [*Stewart*, 2009], if the water depth is much smaller than the wavelength, then kd<<1 and tanh(kd) ≈ 1. Equation (3.1) reduces to:

$$c = \sqrt{gd} \tag{3.2}$$

where c is the phase speed at which a particular phase of the wave propagates. Considering the speed of propagation of the wave crest, the crest advances one wave length for one wave period. That is, $c = \frac{\omega}{k}$.

From the initial point of perturbation, the surface wave propagated from 20°N 150°E to 20°N 160°E in 9 hours translating at a speed of 30.9 m s^{-1}. The shallow water approximation is valid for water depths much less than the wavelength. Here, the water depth is 100 m while

the wavelength is about 100 km. The water depth in this case is only 0.1% that of the wavelength, making the shallow water approximation a valid assumption. From equation (3.2), the surface gravity wave in this case should advance at a phase speed of 31.3 m/s, which is consistent with the ROMS output.

Next, the SSH response on a longer time scale is examined using an idealized tropical cyclone to force the ocean model over 8 days. The idealized cyclone produces a maximum cumulative rainfall of 32 cm (Figure 3.2) and this is forced onto two ocean cases, one with a depth of 100 m and the other with a depth of 1000 m. When rain mass is added via point sources, vertical momentum is generated in the process. At this time, the vertical velocity generated is of the magnitude of 10^{-6} m/s when a rain rate of 5 mm/day is introduced. Considering an extreme precipitation case, such as Typhoon Morakot's record 741 mm/day [*Wu*, 2013], the vertical velocity generated will still be within the range of 10^{-4} m/s, which is extremely small considering the horizontal model resolution of 15 km used here. In this set-up there is no exchange in water mass from the closed boundaries and no additional fresh water sources such as rivers. Hence, rainfall is the only source of mass transfer in the system. In the shallow ocean case (100 m), the maximum SSH drops off by a factor of six over 8 days, from 32 cm to 5.3 cm as shown in Figure 3.3a. The added mass spreads outwards from the mass sources towards the domain boundaries via gravity waves. In the deeper ocean case (1000 m), the maximum SSH decreases much faster to 3.2 cm as shown in Figure 3.3b. From equation (3.2), gravity waves in the deeper case travel 3 times faster than in the shallow water case, which accounts for the faster decrease in SSH in the deeper ocean. With the rain mass spreading out faster in the deeper ocean, the minimum SSH reaches a greater magnitude for the deep ocean case (2.3 cm) compared to the shallow ocean case (1.3 cm).

At longer time scales (after 7 days), the pressure gradient generated from the increase in sea surface height creates a geostrophic adjustment and geostrophic currents of the magnitude 0.01 m/s are generated. The geostrophic adjustment is further examined by considering the various components of momentum from equations (2.1) and (2.2). The largest components are the Coriolis and pressure gradient terms, while the horizontal advection, vertical advection, horizontal viscous and vertical viscous terms are much smaller. In the example illustrated in Figure 3.5, the pressure gradient force at the point 20°N 141°E acts in the direction of the coast due to the higher sea surface level at the middle of the ocean compared to the coast. As shown in Figure 3.13b, the SSH is higher to the east of 20°N 141°E compared to the west of it. In this case, the Coriolis force (u-component) is opposite in direction to the pressure gradient force (u-component) and almost similar in magnitude. The pressure gradient force (u-component) is slightly larger than the Coriolis force (u-component) and there is a net acceleration (u-component) towards the coast. With the added rain mass, the difference in SSH generates a pressure gradient outwards from the locations of higher SSH to lower SSH as shown in Figure 3.6. With the pressure gradient force acting outwards from the position of increased rain mass, the right-ward geostrophic currents generate a clockwise rotating gyre around the centre of increased mass. In hydrostatic balance, the pressure at each height along the water column adjusts accordingly with the new mass added at the top. At the bottom of the ocean, there is a pressure gradient generated due to the higher pressure at the locations where rain mass has been added (Figure 3.7). Similarly, this outward-acting pressure gradient force is balanced by the Coriolis force acting in the opposite direction. The right-ward geostrophic currents generate a similar clockwise rotating gyre around the centre of the increased mass as observed at the ocean surface. The magnitudes of the currents at the bottom are smaller than the surface currents due to the bottom stress.

In Figure 3.3 and Figure 3.4, there is a higher SSH to the south of 20°N compared to the north of it. Onshore and offshore winds can generate positive and negative surges respectively (further discussed in Chapter 4). In this current set-up, the wind field is absent and adding rain mass contributes to storm surges differently along the coastline. When a single pulse of rainfall is introduced (Figure 3.8), a surface gravity wave is generated with a leading crest propagating outwards from the rainfall source (Figure 3.9). The sea surface currents show an overall south-ward flow, showing a right-ward deflection due to Coriolis force. The beta effect is clearly shown in Figure 3.10 when the experiment is repeated with Coriolis force set to zero. Here, there is no deflection due to Coriolis force and the gravity wave propagates symmetrically outwards from the rainfall source.

Next, the two methods of adding rainfall to ROMS are investigated. The existing implementation considers the temperature and salinity of rain but does not include the mass effects. Figure 3.11 and Figure 3.12 show a substantial drop in temperature and salinity due to the effect of rain. The temperature plot (Figure 3.11a) shows distinct areas of cooler temperatures along the path of the cyclone track. The salinity plot (Figure 3.12a) shows a similar effect. In the absence of wind and a lack of advection, tracer quantities such as temperature and salinity spread very slowly via diffusion. The SSH response is very small, with a slight increase of 0.4 cm. Introducing cooler and fresher water into the system creates a temperature and salinity gradient that can set up a small horizontal advection that increases the sea surface elevation slightly. In the proposed rain implementation using point sources, the SSH increases up to 5.8 cm. An increase of 5.8 cm in SSH after introducing up to 32 cm of rainfall is reasonable, compared to the existing ROMS code that generated no substantial rise in SSH regardless of the rainfall amount added.

In the attempt to isolate the implementation of rain stress in ROMS, an error was uncovered in the existing code. The square law relationship between wind stress and wind speed requires that the orthogonal components of wind stress to be resolved by multiplying the magnitude of the net wind speed with the orthogonal components of wind speed as in equations (1.2) and (1.3). For rain stress, there is no square law relationship between rain stress and wind speed and the orthogonal components of rain stress can be resolved by directly equating the orthogonal components of wind speed. The implementation of the rain stress parameterization in ROMS may have been carried out in a similar fashion as wind stress, resulting in the incorrect use of the wind speed instead of the orthogonal components of wind speed.

In the existing implementation of rain stress in ROMS, the u and v components of the rain stress are calculated using the magnitude of the net wind speed and will always be identical in magnitude. As such, the magnitude of the u-component winds (U) and the v-component winds (V) used in the calculation of wind stress will always be $\sqrt{U^2 + V^2}$. This results in a systematic overestimation in the magnitude of rain stress by a factor of $\sqrt{2}$. The error in the direction of rain stress is more inconsistent. Since U and V are always set to be equal in magnitude (equal to the net wind speed), the directions of the rain stress can only be in any of the four directions: 45°, 135°, 225° and 315°, unless there is zero rainfall or zero wind speed. On top of that, the Fortran sign transfer function (SIGN) used in the ROMS rain stress code always assigns a positive sign to zero values. For example, if the U is zero, it will still be assigned the magnitude of the V (now equal to the magnitude of the net wind speed) with the direction of positive U. This is further illustrated in Figure 3.16, with 16 directional scenarios showing the error within each 22.5° directional case. The error in the direction of the rain stress term can range from 0° (when U=V) to 45° (when either U=0 or V=0).

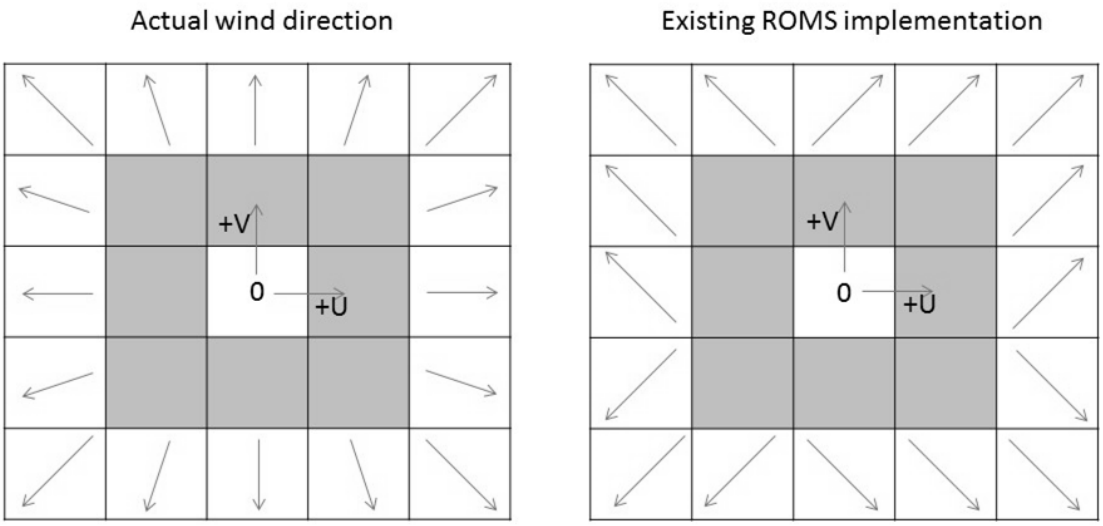


Figure 3.16: Wind direction scenarios illustrating the errors that would arise when using the existing ROMS implementation of rain stress.

With the implementation of rain stress now corrected in ROMS, the SSH response to rain stress is shown by forcing ROMS with an idealized tropical cyclone. Figure 3.15 shows the response of SSH and sea surface currents to rain stress. Rain stress is parameterized as a function of rain rate and wind speed and follows the direction of the winds. Hence, rain stress is only exerted in areas where non-zero values of rain rate and wind speed coincide. In the case of a tropical cyclone, rainfall is highest along the rain bands towards the centre of the cyclone. Rain stress contributes to storm surges in a manner similar to wind stress. Ekman transfer of momentum from the anti-clockwise rotating rain stress to the sea surface creates an anti-clockwise gyre. Coriolis force deflects the currents to the right and generates an outward diverging flow that decreases the SSH at the centre of the gyre. The concept of Ekman pumping has been discussed in Section 1.2.1 and illustrated in

Figure 1.3. When the cyclone makes landfall, the onshore and offshore rain stress generates a positive and negative surge respectively. There is an asymmetry in the positive and negative

surge, with the negative surge at a factor of 1.4 to the positive surge. This asymmetry is similar to that created by an anticlockwise rotating wind stress and will be further investigated in Chapter 4.

3.9 Conclusion

In Chapter 2, a new rainfall scheme has been set up in ROMS to consider the mass effects of rainfall. In this chapter, the effect of rain mass is investigated. When a single-point rain perturbation is introduced to the ocean surface, the perturbation generates surface gravity waves with a propagation speed that is proportional to the square root of water depth. An idealized tropical cyclone is used to investigate the effect of adding rain mass over longer time scales. The rain mass added to the ocean surface spreads out from the path of the cyclone via gravity waves. A maximum cumulative rainfall of 32 cm over 7 days increased the SSH to a maximum of 5.8 cm in a closed basin 30° by 40° and 100 m in depth. When the depth of the ocean is increased to 1000 m, the surface gravity waves travel faster and the SSH increase after 7 days is only up to 3.2 cm. With the increased speed of spreading in the deep ocean, the minimum SSH reaches a greater magnitude of 2.3 cm compared to 1.3 cm in the shallow case. At time scales of several days, the increased SSH from the rain mass creates an outward-directing pressure gradient that is balanced by Coriolis force in the opposite direction. With this geostrophic adjustment, a clockwise flow is generated around the region of increased SSH. The spreading of rain mass is also affected by Coriolis force. For a tropical cyclone making landfall in the Northern hemisphere, the rain mass diverging from the coastline is deflected to the right, increasing the SSH more to the left of the cyclone's path more than to the right of it.

A comparison between the two implementations of rainfall in ROMS is made. The existing rainfall implementation considers the temperature and salinity effects of rainfall but not the mass of rainfall. When forced by an idealized tropical cyclone, ROMS responds to the rainfall with a cooling of the SST by 1.22°C and freshening of the SSS by 1.85 psu from the ambient conditions. The new rainfall scheme considers the mass of rainfall by introducing point sources to the rainfall locations. This approach introduces rain mass into the system without prescribing temperature and salinity conditions since that has been taken care of in the existing implementation of ROMS. Here, the SSH increase is up to 5.8 cm from the effects of rainfall. Ultimately, the point source implementation of rainfall should be incorporated together with the existing ROMS code such that the temperature, salinity and mass effects of rainfall are considered in the simulation.

Next, the momentum transfer from rainfall to the ocean surface has been investigated. *Caldwell and Elliott* [1970] have parameterized rain stress as a function of rain rate and wind speed, transferring momentum to the ocean surface in the same direction as the wind. While this parameterization has been widely adopted by many models such as ROMS, it has only been incorporated and its isolated effects have never been investigated. An idealized set-up of the ROMS model is used to investigate the effect of rain stress on the sea surface height. A point-source rain stress perturbation on the water surface sets off a surface gravity wave that propagates out radially. A positive front is formed ahead of the perturbation propagating in the direction of the surface wind, while a negative front propagates behind the point of perturbation in the opposite direction. Isolating the effect of rain stress in ROMS uncovered an oversight in the existing implementation in ROMS. The existing implementation of rain stress equated the net wind velocity to the resolved rain stress components. In doing so, it produced a systematic overestimation in its magnitude by 41% and an error in the direction of up to 45°. In the case of a tropical cyclone, the response of SSH and sea surface currents to

rain stress is very similar to wind stress. Ekman pumping is generated from the anticlockwise rotating rain stress. When the cyclone makes landfall, positive and negative surges are generated from the onshore and offshore rain stress respectively. There is an asymmetry in the magnitude of the positive and negative surges and this will be further investigated in Chapter 4.

4 Asymmetry in positive and negative surges

4.1 Introduction

The onshore and offshore winds of tropical cyclones have been observed and described to generate positive and negative surges respectively. While positive surges have been extensively studied due to the high impacts of coastal inundation, negative surges are not as well understood. Negative surges can cause ship grounding that leads to hull damage, subsequent collisions and even oil spill disasters. Negative surges can also deplete drinking water supply by draining coastal aquifers [*Pousa et al.*, 2013] and destroy coastal aquacultures [*AsSalek*, 1997]. *AsSalek* [1997] investigated the factors influencing negative surges, but these factors were highly specific to the complicated coastline of the Meghna estuary and did not isolate the primary mechanism effectively.

Studies from *Pousa et al.* [2013] and *Pugh* [1987] have reported on the asymmetry in positive and negative surges generated by strong winds during storms events. However, there are very few studies that have discussed this asymmetry. *Peng et al.* [2006] have described the asymmetry in positive and negative surges using a one-dimensional mechanism at a single coastal point. However, positive and negative surges occur simultaneously along the coast line and a one-dimensional mechanism would not be sufficient to describe the process. In this chapter, an idealized set-up in ROMS is used to provide a basic framework to understand the asymmetry between the positive and negative surges. ROMS is forced by an axisymmetric cyclone that treks towards the coastline, makes landfall and generates a storm surge. This makes the case sufficiently general for understanding the basic mechanism and for applications in real case scenarios. Apart from the asymmetry in the vertical extent of the

positive and negative surges, the asymmetry in the horizontal extent is also examined. In this spatial analysis, the importance of the 2-D wind field and the alongshore wind to negative surges is shown for the first time.

4.2 Results

An idealized set-up of ROMS is used to isolate the SSH response to winds from an idealized cyclone. This set-up is outlined in Section 2.2.2. The axisymmetric wind field is described by *Chan and Williams* [1987] and detailed in Section 2.3.1. The vortex is initialized to the right of the domain at 20°N 165°E and translated westward at the speed of 15 km/h for a total of 5 days. The temperature, rain, pressure, humidity, long-wave radiation and short-wave radiation fields are prescribed to be spatially constant and time-invariant. Increasing the atmospheric pressure has been known to decrease the SSH by 1 cm per mbar (Section 1.2.2), but this is a systematic and symmetric change localized near the cyclone centre. For clarity, the inverse barometer effect, together with other environmental conditions that can affect SSH are not considered here in order to isolate the effect of wind on the asymmetry of storm surges.

Six experiments are conducted to investigate the SSH response under different wind and ocean scenarios, as outlined in Table 4.1. The spatial extent of Cases A and B is identical to the atmospheric domain (5°N to 35°N, 120°E to 180°E). The bathymetry is uniform at 100 m. For Cases C and D, the domain is shifted northwards by 10° (15°N to 45°N, 120°E to 180°E). The same cyclone wind field is used to force the ocean model. Cases E and F have the same spatial extent as the atmospheric domain (5°N to 35°N, 120°E to 180°E) and a bathymetry that slopes linearly from 50 m near the coast eastwards to a maximum of 954 m. The chosen ratio of 1:5000 is an average of the range of coastal slopes studied by *Irish et al.* [2008],

where the influence of storm size on hurricane surge over coastal slopes ranging from 1:250 to 1:10000 was investigated. Cases A, C and E are forced by the complete wind field, which includes both the cross-shore and alongshore wind components. Cases B, D and F are forced only by the cross-shore wind component, with the alongshore wind component set to zero.

Cases	***Wind Conditions***	***Spatial Extent***	***Bathymetry***
Case A	Both cross-shore and alongshore components	5°N to 35°N, 120°E to 180°E	Constant 100 m
Case B	Cross-shore component only	5°N to 35°N, 120°E to 180°E	Constant 100 m
Case C	Both cross-shore and alongshore components	15°N to 45°N, 120°E to 180°E	Constant 100 m
Case D	Cross-shore component only	15°N to 45°N, 120°E to 180°E	Constant 100 m
Case E	Both cross-shore and alongshore components	5°N to 35°N, 120°E to 180°E	Slope of 1:5000
Case F	Cross-shore component only	5°N to 35°N, 120°E to 180°E	Slope of 1:5000

Table 4.1: Cases set up with different wind and ocean conditions.

The time-frame at 105 hours is chosen as a fair representation of the peak positive surge and negative surge during the event. Not all the cases exhibit their peak positive and negative surges at the same time-step, and 105 hours is selected for consistency. A later analysis (Figure 4.6) shows that 105 hours is a good representation of the peak surges. The figures are zoomed into 13°N - 28°N and 132°E - 158°E to display details at the coastline. The surface stresses are shown in Figure 4.1 and Figure 4.2. Figure 4.1 shows the complete wind field as the cyclone crosses the coastline. The surface stress is anticlockwise rotating and centered on

20°N 140°E. Figure 4.2 shows the cross-shore and alongshore component of the surface stresses. The onshore surface stress is largest around 21°N 140°E and the offshore surface stress is largest around 19°N 140°E. At 105 hours, the cyclone centre almost coincides with the coastline and the coastal flow is strongly influenced by a northward alongshore surface stress.

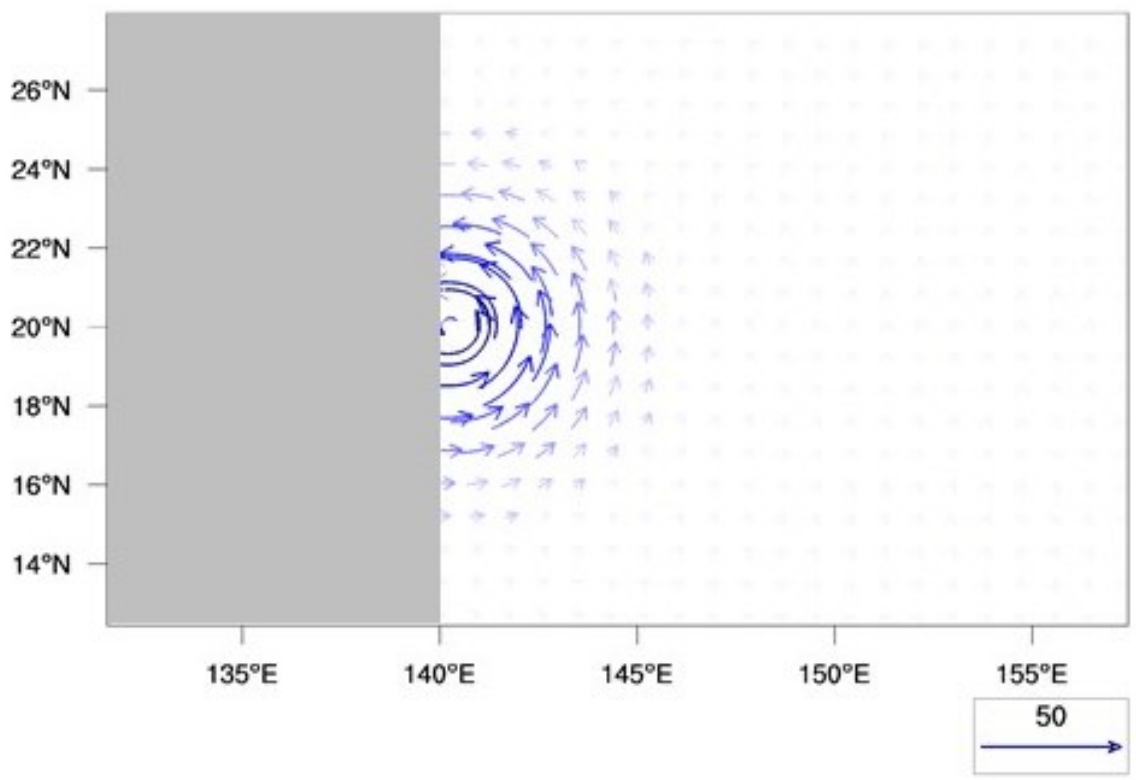


Figure 4.1: Surface stress (N/m^2) response to the total wind stress at 105 hours.

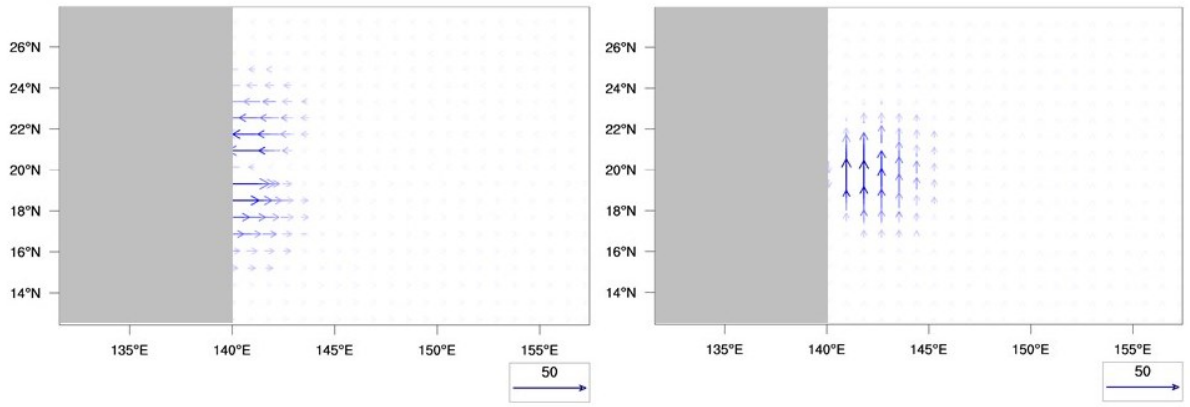


Figure 4.2: Surface stress (N m^{-2}) response (at 105 hours) to only the cross-shore wind stress (left) and only the alongshore wind stress (right). The reference vector for the surface stress is in 50 N m^{-2}.

Figure 4.3 shows the sea surface height response at 105 hours when the cyclone makes landfall at 140°E for the Case A. In Figure 4.3a, an anticlockwise circulation centering 20°N 142°E is generated with a decrease in SSH at the circulation centre. Along the coastline at 140°E, the magnitude of the negative surge is much larger compared to the positive surge. The positive surge is up to +5.3 m and the negative surge is up to -13.1 m. Figure 4.3b shows the SSH response to only the cross-shore component of the wind stress in Case B. Similar to Figure 4.3a, an anticlockwise circulation is generated, but it is elongated zonally and the circulation centre is shifted eastward to 143°E instead of 142°E. The surge pattern is substantially more symmetrical with a positive surge of up to +4.0 m and a negative surge of up to -4.5 m.

(a) (b)

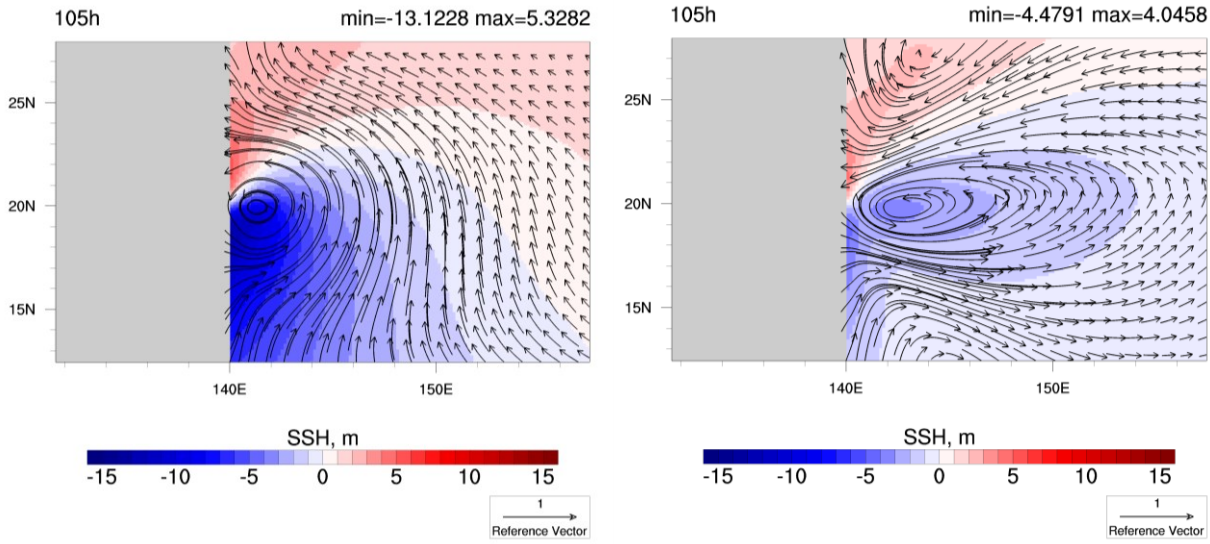


Figure 4.3: SSH response to (a) Case A and (b) Case B at 105 hours into the simulation. The reference vector for the sea surface currents is 1 m/s.

Next, the role of the Coriolis parameter in Case C is shown in Figure 4.4a. Compared to Case A in Figure 4.3a, Case C shows an enhanced rightward deflection in the sea surface currents. There is a larger decrease in SSH at the anticlockwise circulation centering 30°N 142°E. The positive surge is decreased from +5.3 m to +4.4 m and the negative surge is enhanced from -13.1 m to -14.6 m. With the alongshore wind stress removed in Case D (Figure 4.4b), the positive and negative surges are more symmetrical compared to the case with the complete wind field shown in Figure 4.4a. The positive surge is decreased slightly to +3.9 m but the negative surge is weakened substantially to -5.0 m.

(a) (b)

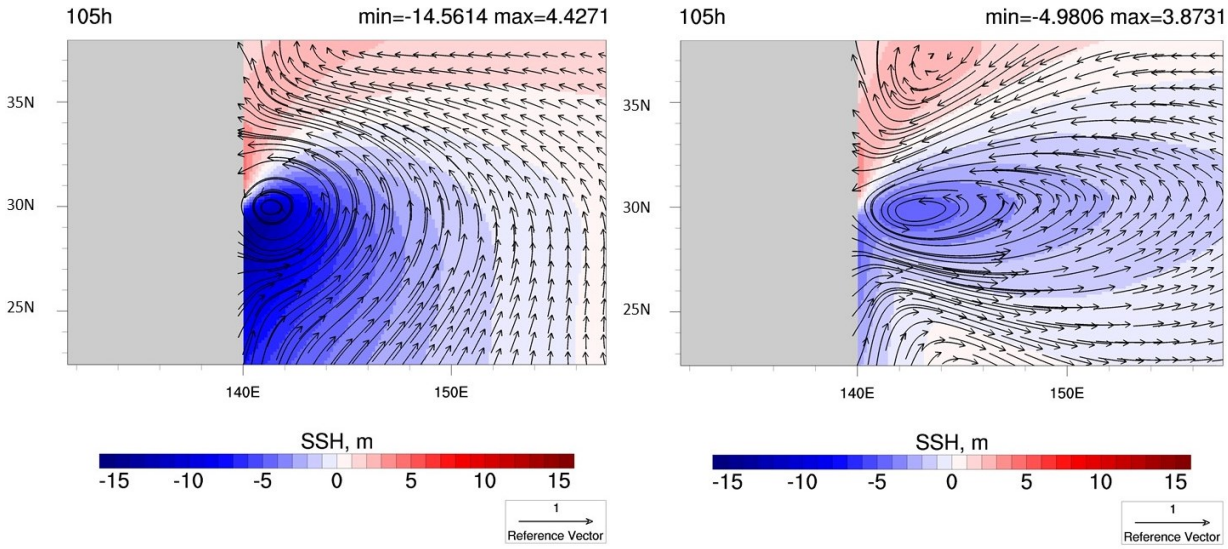


Figure 4.4: Sea surface height response to (a) Case C and to (b) Case D at 105 hours into the simulation. The reference vector for the sea surface currents is 1 m/s.

Figure 4.5 shows the SSH response in Case E. Here, the bathymetry varies at a gradient of 1:5000, with a depth of 50 m at the coast to a depth of 954 m at the eastern boundary. Compared to Case A in Figure 4.3a, Figure 4.5a shows an overall weaker response in SSH and the ocean currents are less regular. A negative SSH can still be observed at the centre of the anticlockwise circulation centering 30°N 142°E. The positive surge is up to +4.0 m and the negative surge is up to -6.7 m. The magnitude of the negative surge is still larger compared to the positive surge. With the alongshore wind stress removed in Case F (Figure 4.5b), the positive and negative surges are more symmetrical compared to the case with the complete wind field shown in Figure 4.5a.

(a) (b)

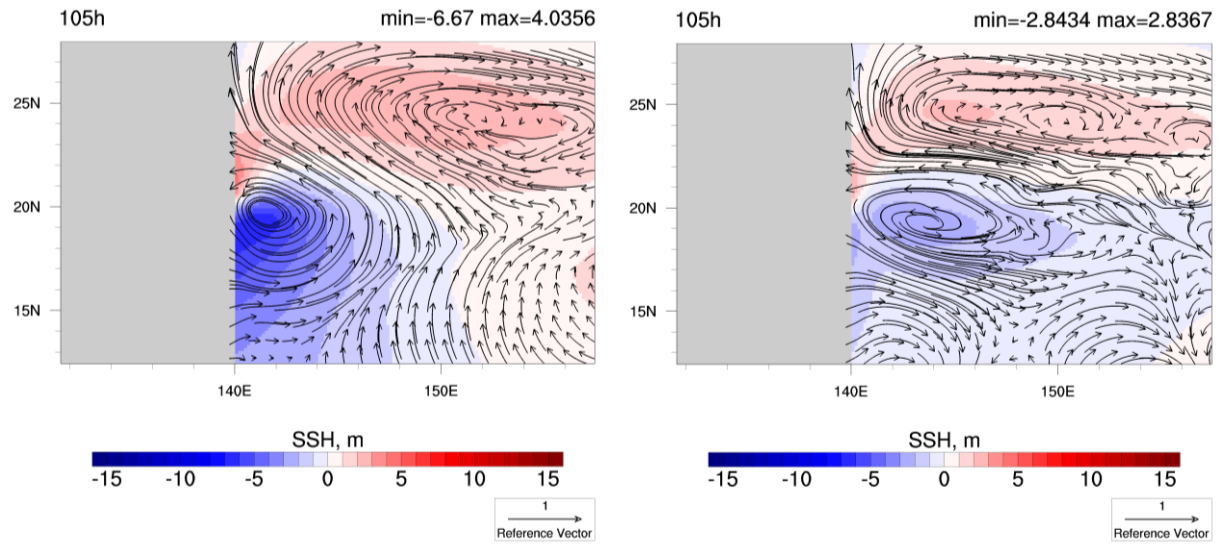


Figure 4.5: SSH response to (a) Case E and to (b) Case F at 105 hours into the simulation. The reference vector for the sea surface currents is 1 m/s.

Next, the maximum of the surges at any time along the coast is examined. Figure 4.6 shows the cross section of the peak positive and negative surges (at 140°E) at any time during the simulation. This shows the worst case scenario that the coastline experiences for this event. The horizontal axis shows the latitudes spanning 10°N to 30°N (or 20°N to 40°N for the higher latitude case). Cases A, C and E with both the cross-shore and alongshore wind stresses (bold lines) show a larger magnitude for the negative surge compared to the positive surge. The surge ranges from -13.1 m to +5.3 m for Case A, -14.6 m to +4.5 m for Case C and -6.7 m to +4.0 m for Case E. Cases B, D and F with only the cross-shore wind stress (dashed lines) have weak asymmetry and comparable positive and negative surges. The surge ranges from -5.3 m to +4.6 m for Case B, -5.4 m to +4.4 m for Case D and -3.0 m to +3.0 m for Case F. These results also confirm the choice of 105 hours to map the horizontal extent of

the surges for all cases in Figure 4.3, Figure 4.4 and Figure 4.5 as the numbers at 105 hours and the simulation maximum in Figure 4.6 are very similar.

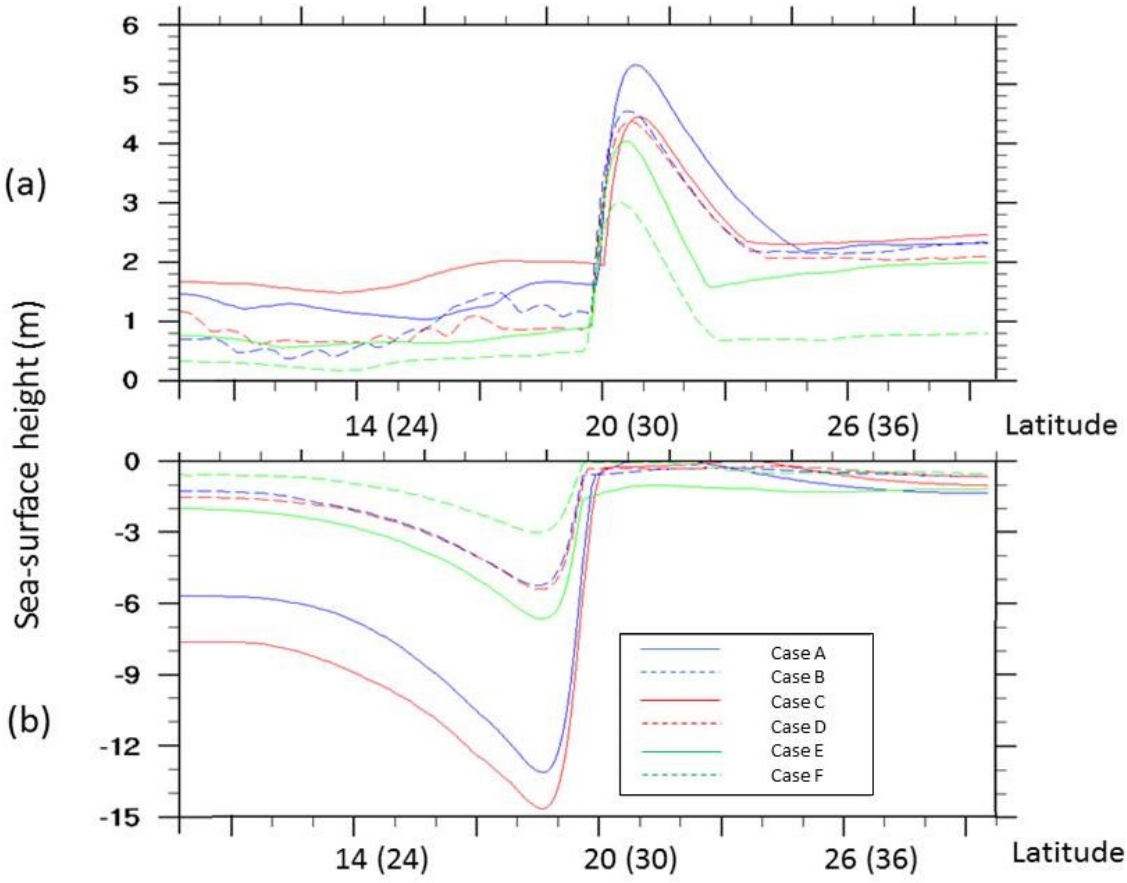


Figure 4.6: SSH along the coastline at 140°E. (a) Plot of temporal maximum SSH against latitude (b) Plot of temporal minimum SSH against latitude.

Considering the horizontal extent along the coastline, the positive surge affects a smaller extent compared to the negative surge. In Cases A, C and E with both the cross-shore and alongshore wind stresses, the positive surge is narrowly distributed along the coast compared to the negative surge which extends far to the south. For Cases B, D and F with only the cross-shore wind stress, both the positive and negative surges have comparably narrow distributions along the coast. For example, in Case A, the coastal extent impacted by a positive surge larger than +4 m is 2°, while the region impacted by a negative surge lower

than -4 m is 20° or more. Without the alongshore wind stress component in Case B, the coastal region that is affected by a positive surge greater than +4 m is halved to about 1°, while the region that is affected by a negative surge larger than -4 m is reduced by a factor of 10 to only about 2°. In Case C with the total wind field, the 4 m impact extent of the positive surge is 1° while the horizontal extent of the negative surge is increased much further to 25° or more. Without the alongshore component in Case D, the region with a surge greater than 4 m remains at 1°, while the region with a surge lower than -4 m is reduced by a factor of 13 to only 2°. For Case E, the coastal region impacted by a positive surge greater than 2 m is 2.5°, while the region with a negative surge lower than -2 m is 10°. Without the alongshore component in Case F, the region with a surge greater than 2 m is reduced to 1.5°, while the region impacted by a surge lower than -2 m is only 2.5°.

Next, the time-series of the positive and negative surges are studied to understand the time evolution of the surges and not be confined to the single time of 105 hours chosen earlier. Two coastal points are located to represent the positive and negative surges. Figure 4.7 shows the cross-shore surface stress that is experienced at the coastline at 106 hours. While 105 hours is chosen earlier to illustrate the peak surges in all three scenarios, the time of 106 hours is now selected as it is the time when the alongshore surface stress alters its direction from southward to northward. In terms of the ROMS grid system, the coastline is at $\xi = 130$ (x-direction) along the η points (y-direction) from $\eta = 0$ to 200. The maximum onshore surface is around 21°N (η=110) and the maximum offshore surface stress is around 19°N (η=90). These two points will be used to analyse the positive and negative surges during this event.

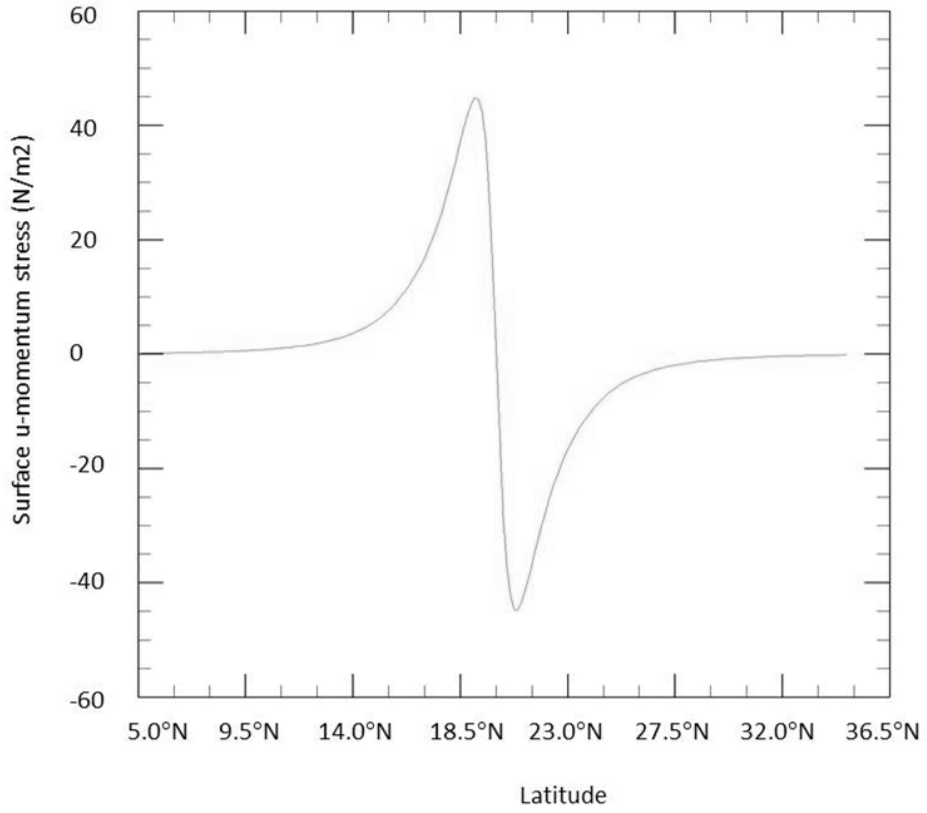


Figure 4.7: Surface u-momentum stress along the coastline at 140°E (t = 106 hours).

Figure 4.8 shows the surface stresses at 21°N 140°E. Here, the maximum onshore stress is at 106 hours. This is also the time corresponding to the point of inflexion for the surface v-momentum stress. The coastline experiences a southward alongshore wind stress up to 106 hours and switches direction to a northward alongshore wind stress after 106 hours. The point 19°N 140°E will show the same plots for surface momentum stress, but the surface u-momentum stress will be reversed in direction.

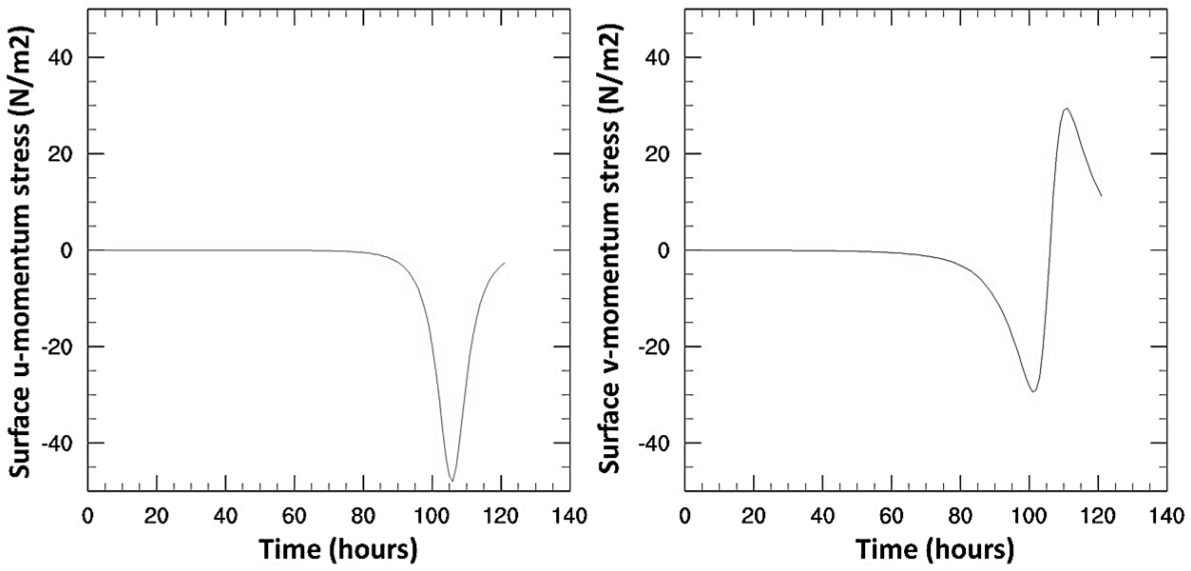


Figure 4.8: Time-series of surface momentum stress at 21°N 140°E, showing the u-momentum stress (left) and v-momentum stress (right).

The time-series of SSH response of the positive surges (21°N 140°E) and the negative surges (19°N 140°E) is investigated in the control case. Figure 4.9 shows the comparison between the SSH response to the total wind stress (solid lines) in Case A and the SSH response to only the cross-shore wind component (dashed lines) in Case B. At 21°N 140°E, the SSH response is higher for the case with the total wind stress up to 90 hours. Between 90 hours and 103 hours, the SSH response is lower in the presence of the alongshore wind component. From 103 hours onwards, the SSH response is again higher when the alongshore wind component is present. At 19°N 140°E, the SSH response is higher in the presence of the alongshore wind component up to 90 hours. From 90 hours onwards, the SSH response is lower in the presence of the alongshore wind component.

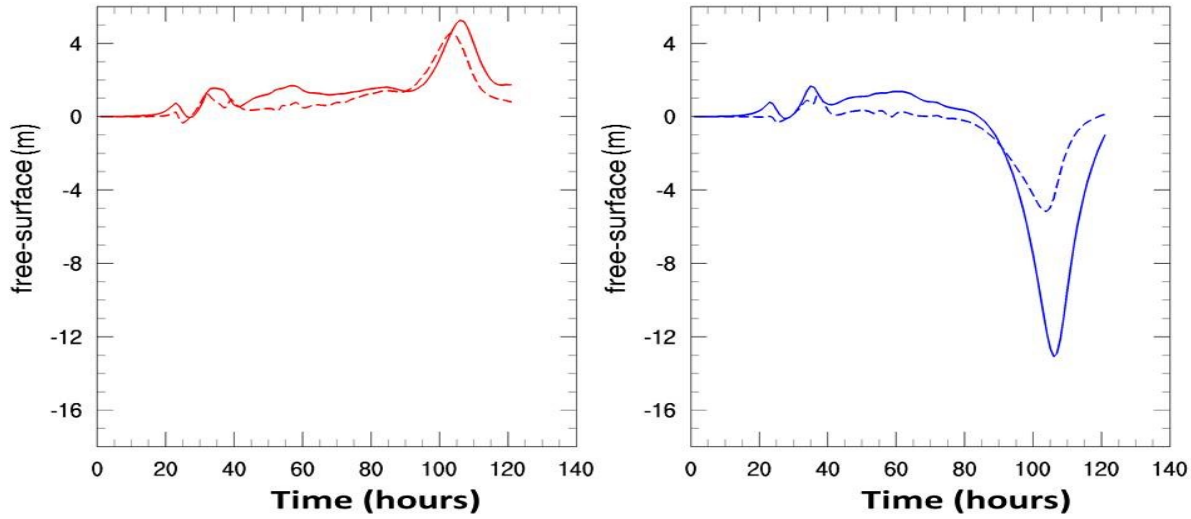


Figure 4.9: SSH response at the points 21°N 140°E (left) and 19°N 140°E (right) for the control case, forced with the total wind field (solid lines) and with only the cross-shore wind component (dashed lines).

Next, the positive surge at 21°N 140°E and the negative surge at 19°N 140°E are compared between Case A and Case C as shown in Figure 4.10. Here, the two cases are forced by both the cross-shore and alongshore winds. Before 100 hours, increasing the latitude increases both the positive and negative surges at 21°N 142°E and at 19°N 142°E respectively. From 100 hours onwards, increasing the latitude decreases both the positive and negative surges at 21°N 142°E and at 19°N 142°E respectively.

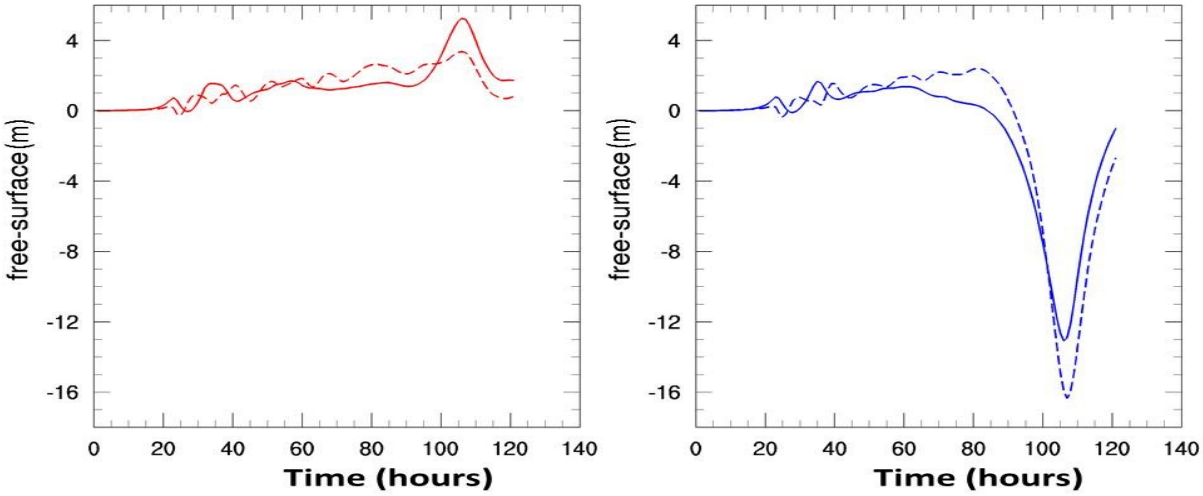


Figure 4.10: SSH response at the points 21°N 140°E (left) and 19°N 140°E (right) in the control case (solid lines) and the higher latitude case (dashed lines). Both cases are forced with the complete wind field.

Finally, the positive surges at 21°N 140°E and the negative surges at 19°N 140°E are compared between Case A and Case E (Figure 4.11). The magnitude of the positive and negative surges at 21°N 142°E and at 19°N 142°E respectively is generally reduced with the sloping bathymetry.

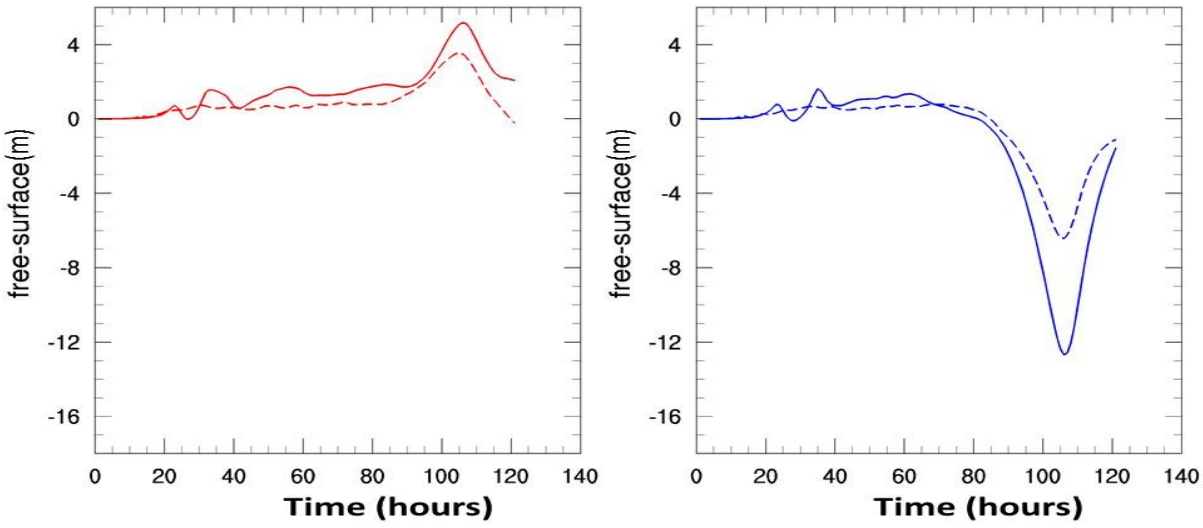


Figure 4.11: SSH response at the points 21°N 140°E (left) and 19°N 140°E (right) in the control case (solid lines) and the sloping bathymetry case (dashed lines). Both cases are forced with the complete wind field.

4.3 Discussion

A mechanism has been proposed by *Peng et al.* [2006] to account for the one-dimensional (1D) asymmetry in the sea level response: the pressure gradient force required to balance the wind is a function of $(h+\zeta)d\zeta/dx$ (where h, ζ, x are the undisturbed water depth, the sea surface elevation and distance from the coast, respectively). This 1D analysis does explain the basic asymmetry in positive and negative surges, where it is relatively easier to move the lower water mass for a negative surge, given the same wind conditions. However, observations and analyses described by *Pousa et al.* [2013] and *Pugh* [1987] showed horizontal surge features that a one-dimensional mechanism cannot fully represent quantitatively. The idealized study here provides a basic framework for the understanding of

cyclone-driven surges and a spatial analysis is important to understand the asymmetry between the positive and negative surges.

Figure 4.3a shows the sea surface height response to the surface wind stress of a tropical cyclone. As the cyclone moves westwards, anticlockwise ocean currents are generated due to the transfer of momentum from the anticlockwise wind stress. Ekman transfer of momentum from the wind stress deflects the currents to the right and sets up an outward diverging flow that decreases the sea surface height at the centre of the anticlockwise circulation at 20°N 142°E. This has been discussed in Chapter 1 and illustrated in

Figure 1.3. As the cyclone makes landfall at 140°E, the easterly wind to the north of 20° generates a positive surge. The westerly wind to the south of 20°N generates a negative surge. Here, the positive surge is up to +5.3 m and the negative surge is up to -13.1 m. The predicted asymmetrical response pattern shown here is also observed in the storm affecting the coast of Argentina in 1984 [*Pousa et al.*, 2013] where the clockwise rotating storm created a positive surge of +1.9 m at Mar de Plata and a larger negative surge of -3.7 m at Buenos Aires, which is located north of Mar de Plata. *Pugh* [1987] reported a maximum positive surge of +4.5 m and negative surge of -4.0 m when the storm of 1982 made landfall at the Orissa coast of India. As shown in Figure 4.12, the large +4.5 m surge is only observed in a small region within the funnel-shaped bay between Dhamra and Chandipur and is due to the flow converging into the bay. For a regular coastline without the bay, the positive surge is expected to be +1.5 m, as observed outside the bay.

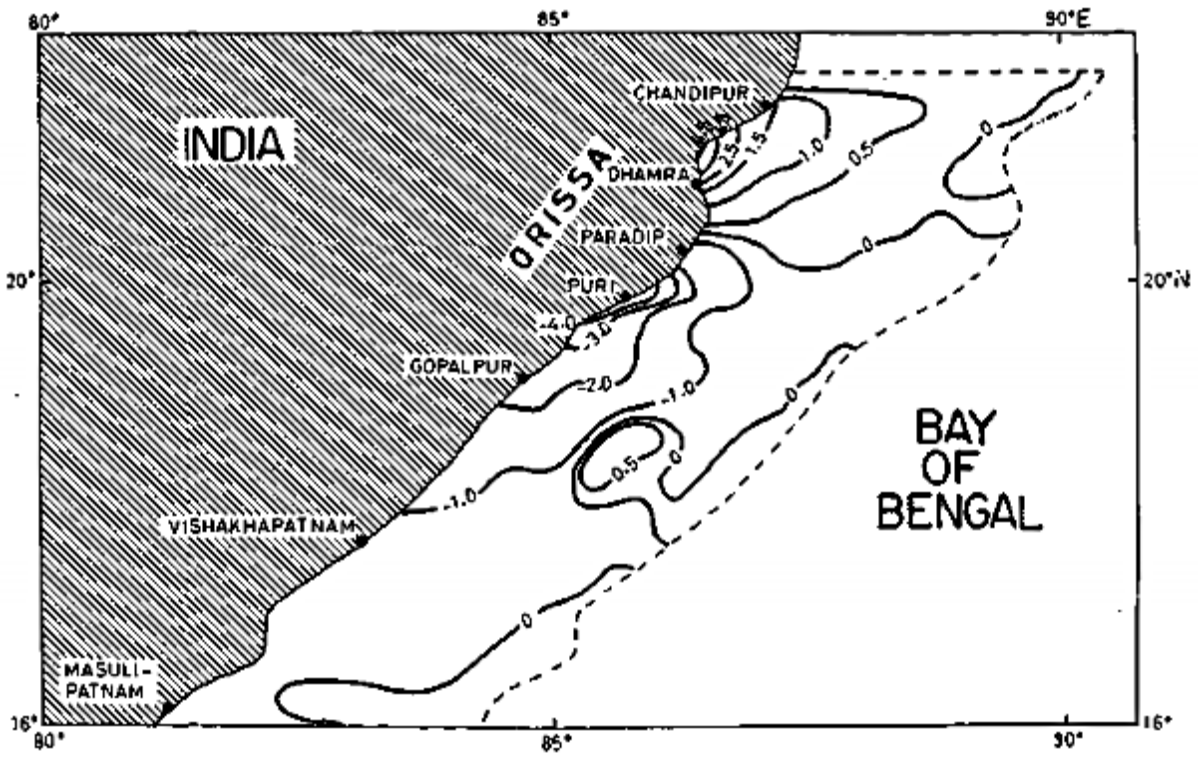


Figure 4.12: Map of Bay of Bengal showing the contours of sea surface heights generated 30 min after the storm made landfall at the Orissa coast. Extracted from *Pugh* [1987].

In the absence of the alongshore wind stress (Figure 4.3b), the coastal surge pattern is more symmetrical along 20°N. The anticlockwise circulation is elongated along 20°N since only the cross-shore wind stress is present. The centre of the anticlockwise circulation is shifted eastwards with the western land-mask acting as a barrier, shifting the elongated water mass eastwards. The northward alongshore wind stress generates a northward advection of water mass that increases the positive surge and decreases the negative surge (Figure 4.3a). In addition, Ekman transfer of momentum deflects the northward alongshore flow rightwards, decreasing the overall SSH at the coast. Without the alongshore wind stress, the alongshore advection and Ekman transport oppose in the case of the positive surge, showing an overall decrease from +5.3 m to +4.0 m. For the negative surge, the alongshore advection and Ekman transport add up, resulting in a substantial decrease in the magnitude of the negative surge

from -13.1 m to -4.5 m. This substantial additional decrease demonstrates that the alongshore component of the wind stress plays a very important role in creating the asymmetry between the positive and negative surges. Storm surges that are modelled simply by using onshore and offshore winds generate fairly symmetrical surge patterns as shown in Figure 4.3b. In the case of a southern hemisphere scenario, the tropical cyclone will be rotating clockwise, creating a southward alongshore component in the same domain set-up. The results will be inverted but conceptually the same.

When the ocean domain is shifted northward by 10° (comparing Figure 4.3a and Figure 4.4a), the ocean currents are deflected more towards the right with the enhanced Coriolis force. The increased rightward deflection of the northward alongshore surface stress decreases both the positive and negative surges. The comparison between Cases C and Dis similar to the comparison between Cases A and B as discussed above. The presence of the northward alongshore wind stress in Case A generates a northward advection of water mass that increases the positive surge and decreases the negative surge. On the other hand, Ekman transport deflects the northward alongshore flow rightwards, decreasing the overall SSH at the coast. Without the alongshore wind stress (Case B), the two effects oppose in the positive surge case, resulting in an overall decrease from +4.4 m to +3.9 m. For the case of the negative surge, these two effects complement each other and result in a larger decrease in the magnitude of the negative surge from -14.6 m to -5.0 m. Next, Cases B and D are compared, where both set-ups are forced only by the cross-shore wind stress. With a greater rightward deflection, both the positive and negative surges decrease in magnitude due to the weakened cross-shore surface stress. In addition, the enhanced rightward deflection increases the outward divergence of the anticlockwise circulation, resulting in a greater decrease in the SSH here. Overall, both the positive and negative surge at 21°N 142°E and at 19°N 142°E respectively decreases.

While the previous cases represent a near-shore or continental shelf scenario, the sloping bathymetry case (Figure 4.5) shows a different scenario where the cyclone approaches the coastline from deep waters at a typical 1:5000 slope [*Irish et al.*, 2008]. As the response of the sea surface height to wind stress is inversely proportional to the depth of the water column [*Pugh*, 1987], the deeper water shows a weaker sea surface height response compared to the shallower cases. While the sloping bathymetry case produced smaller magnitude in the asymmetry between the positive and negative surges, it delivers the same qualitative message as the control case. The asymmetry in the magnitude of the positive and negative surges is still substantial. The absence of the alongshore wind stress component generated a fairly symmetrical surge response that is expected from having onshore and offshore winds alone.

The surge asymmetry can be characterised by the ratio defined as $\frac{\zeta^-}{\zeta^+}$ (where ζ^- and ζ^+ are the magnitudes of the minimum and the maximum sea surface height at the coast respectively). In the control case, the absence of the alongshore wind stress decreased the ratio from 2.5 to 1.2, which further demonstrates the significance of the alongshore wind stress in generating the large asymmetry in the positive and negative surges. With a 10° northward shift in latitude, the asymmetry increases to 3.2. The stronger Coriolis deflection on the northward alongshore flow decreases the coastal SSH systematically. This decreases both the positive and negative surges and increases the asymmetry. A deeper and sloping bathymetry lowers the ratio to 1.7, illustrating the effect of the deeper waters in weakening the sea surface height response. However, the effect of the deep ocean is not as significant as the alongshore component of the wind stress. The surge ratios for the storms hitting the Orissa coast in 1982 [*Pugh*, 1987] and the Argentinian coast in 1984 [*Pousa et al.*, 2013] are 2.7 and 1.9 respectively, both of which are well within the range estimated in this study.

In order to rule out the likelihood that the asymmetry in positive and negative surges is generated from the beta effect, Cases A and B are set up with a constant Coriolis parameter corresponding to 20°N. In Figure 4.13, the asymmetry between the positive and negative surges is still present and the beta effect has a very small influence, which only resulted in a small change in the surge magnitudes (0.1 m for Case A). Overall, the flow pattern of the sea surface current is also very similar.

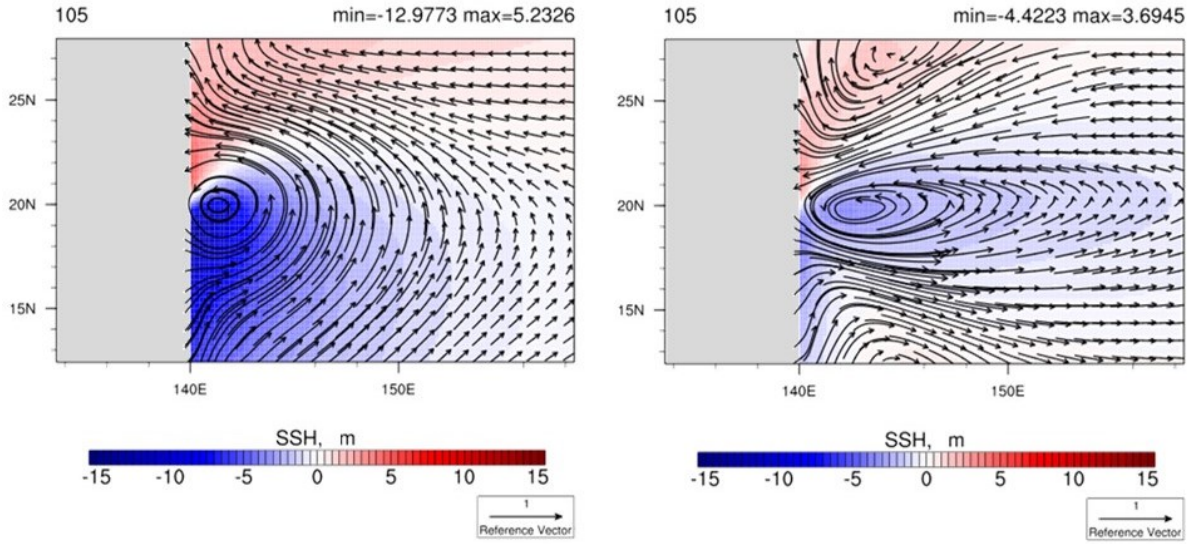


Figure 4.13: SSH response to Case A (left) and Case B (right) at 105 hours into the simulation, with a constant Coriolis parameter corresponding to 20°N. The reference vector for the sea surface currents is 1 m/s.

Apart from the asymmetry in the vertical displacement of the positive and negative surges, there is an asymmetry in the horizontal extent of the positive and negative surges along the coastline which has so far not been noted in literature. Comparing the horizontal extent of the positive and negative surges in Figure 4.6 shows that the alongshore wind stress is the main contributor to this large asymmetry as well. In Case A, the coastal range affected by the negative surge is a factor of 10 greater in extent than that affected by the positive surge. Without the alongshore wind stress (Case B), the asymmetry decreases by a factor of 2. In

Case C, increasing the latitude by 10° northwards raises this asymmetry to 25 but in the absence of the alongshore component (Case D), the asymmetry decreases to 2. With a sloping bathymetry in Case E, the extent of the coast affected by the negative surge is 4 times larger than the extent of the coast affected by the positive surge. Without the alongshore wind stress (Case F), the extent of the coast affected by the negative surge is only a factor of 1.7 larger than the coast affected by the positive surge. This comparison in horizontal extents gave a similar conclusion as the surge ratios discussed previously. The simulation results of *Pugh* [1987] for the storm hitting the Orissa coast of India also shows the negative surge affecting a greater coastal extent than the positive surge. To the left of the storm's approach, a negative surge of 1 m extended up to 3.6° along the coast whereas a positive surge of 1 m extended only up to 1.4° to right of the storm's approach.

In the previous section, it has been suggested that the alongshore advection and the effect of Coriolis force acting on the alongshore flow are important in enhancing the asymmetry in the positive and negative surges. Next, the time-series of the positive and negative surges at 21°N 142°E and 19°N 142°E respectively are analysed to investigate how this enhancement evolves with time, as the cyclone moves towards the shoreline. Figure 4.9 compares the time-series of the storm surge in Case A (solid lines) Case B (dashed lines). Up to 90 hours, both the positive and negative surges at 21°N 142°E and 19°N 142°E respectively are higher in the presence of the alongshore wind component. Coriolis force deflects the southward alongshore wind component to the right, systematically increasing the surge along the coastline. From 90 hours, both the positive and negative surges at 21°N 142°E and 19°N 142°E respectively are lower in the case with the alongshore wind component. Here, Coriolis force deflects the northward alongshore flow to the right, systematically decreasing the surge along the coastline instead. The effect of the Coriolis deflection is more clearly illustrated when the control case and the higher latitude case are compared. Even though the alongshore

surface stress changes direction at 106 hours, the SSH response begins to change as early as 90 hours. This will also be discussed when the Case C is examined. After 103 hours, the positive surge at 21°N 142°E is again higher for the control case. At this time, the southward alongshore wind component begins to weaken and the northward alongshore wind component begins to dominate (Figure 4.9). Before 103 hours the southward alongshore wind stress creates a southward alongshore flow that decreases the SSH at 21°N 140°E. After 103 hours, the northward alongshore wind stress creates a northward alongshore flow that increases the SSH at 21°N 140°E. Hence from 103 hours onwards, the SSH response is again higher in the presence of the alongshore wind component. For the case of the negative surge at 19°N 142°E, the southward alongshore wind stress creates a southward alongshore flow that increases the SSH at 19°N 140°E before 103 hours. After 103 hours, the northward alongshore wind stress creates a northward alongshore flow that decreases the SSH at 19°N 140°E.

The influence of the alongshore advection and Coriolis deflection is illustrated in Figure 4.14. For the positive surge at 21°N 142°E, the effects of alongshore advection and Coriolis deflection oppose each other. Hence, the presence of the alongshore flow can enhance or weaken the surge depending on which effect dominates. As the two effects oppose each other, the overall effect on the positive surge at 21°N 142°E is not as large as the negative surge at 19°N 142°E. For the negative surge at 19°N 142°E, the effect of alongshore advection and Coriolis deflection both increase the SSH when the coastal flow is dominated by the southward alongshore flow and both effects decrease the negative surge at 19°N 142°E when dominated by the northward alongshore flow. The magnitude of the negative surge at 19°N 142°E is particularly large when the cyclone crosses the coastline. At this time, both the

effect of the northward alongshore advection and Coriolis deflection on the northward alongshore flow enhance the negative surge at 19°N 142°E generated by the offshore winds.

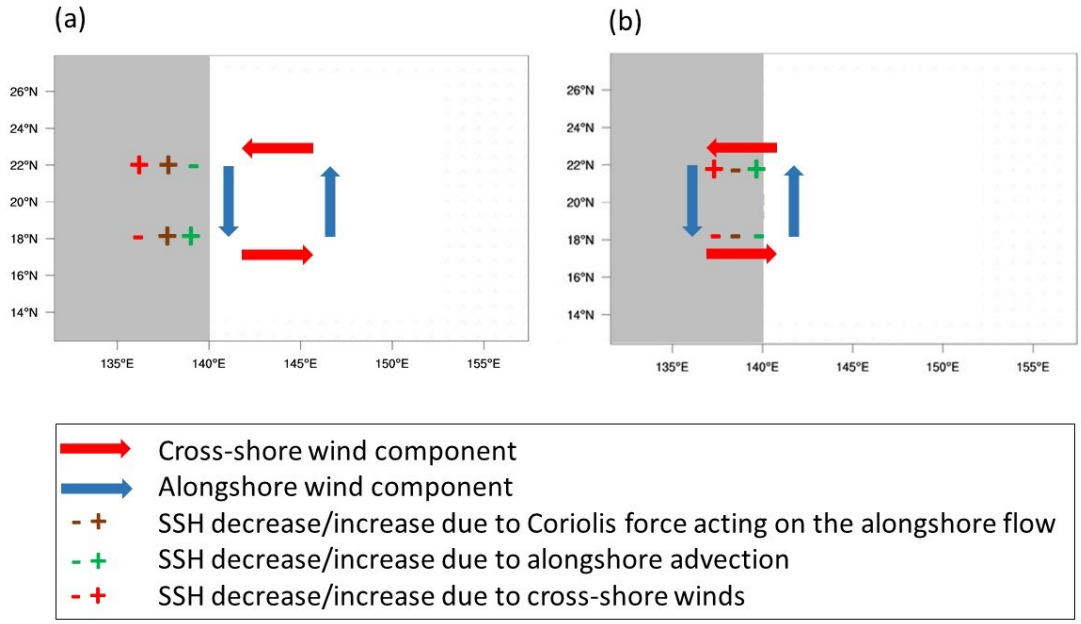


Figure 4.14: Illustration showing how SSH is affected by the southward alongshore wind component (a) and the northward alongshore wind component (b).

Figure 4.10 shows the SSH response in Case A (solid lines) and Case C (dashed lines). Here, both cases are forced by the complete wind field. Before 100 hours, the coastal region is affected by a southward alongshore flow and Ekman transport directs the flow towards the coast, increasing the SSH at the coastline. With increasing latitude, Coriolis force deflects flow more to the right and both the positive at 21°N 142°E and negative surges at 19°N 142°E increase. After 100 hours, the coastal region is affected by a northward alongshore flow and Ekman transport directs the flow away from the coast, decreasing the SSH. Hence both the positive surge at 21°N 142°E and negative surge at 19°N 142°E decrease. Even though the alongshore surface stress changes direction at 106 hours, the SSH response begins to change as early as 100 hours, when the southward surface stress starts weakening and the northward surface stress starts to dominate.

The SSH response in Case A (solid lines) is compared to Case E (dashed lines) as shown in Figure 4.11. Here, both cases are forced by the complete wind field. Here, the magnitude of both the positive surge at 21°N 142°E and negative surge at 19°N 142°E is weakened. As discussed in Chapter 1, equation (1.4) describes how the effect of wind on SSH increases inversely with water depth. Wind blowing across extensive areas of shallow waters will produce a larger increase in sea levels. The water depth in Case E is deeper than in Case A. =Hence, the magnitude of the surges (as well as SSH variations) in Case E is correspondingly smaller compared to Case A.

The magnitudes of the depth averaged alongshore advection and the Coriolis force are plotted in Figure 4.15. Here, 95 h is chosen to show the flow regime before the cyclone reaches the coastline. Overall, the maximum advective term is larger (0.0003 m s^{-2}) than the maximum Coriolis term (0.0001 m s^{-2}). However, the alongshore advection is more confined to the cyclone centre while the Coriolis force has a larger spatial effect. Considering the locations at 25°N 142°E, and 15°N 142°E the advective term is in the order of 10^{-5} m s^{-2} and the Coriolis term is in the order of 10^{-4} m s^{-2}. While advection and the Coriolis force work together in affecting modifying the magnitude of the storm surge, advection plays a more important role near the cyclone centre while the Coriolis force has a larger effect away from the cyclone centre. If the positive and negative surges are investigated based on the points 25°N 142°E, and 15°N 142°E, the Coriolis effect will be the main driving force in modifying the positive and negative surges.

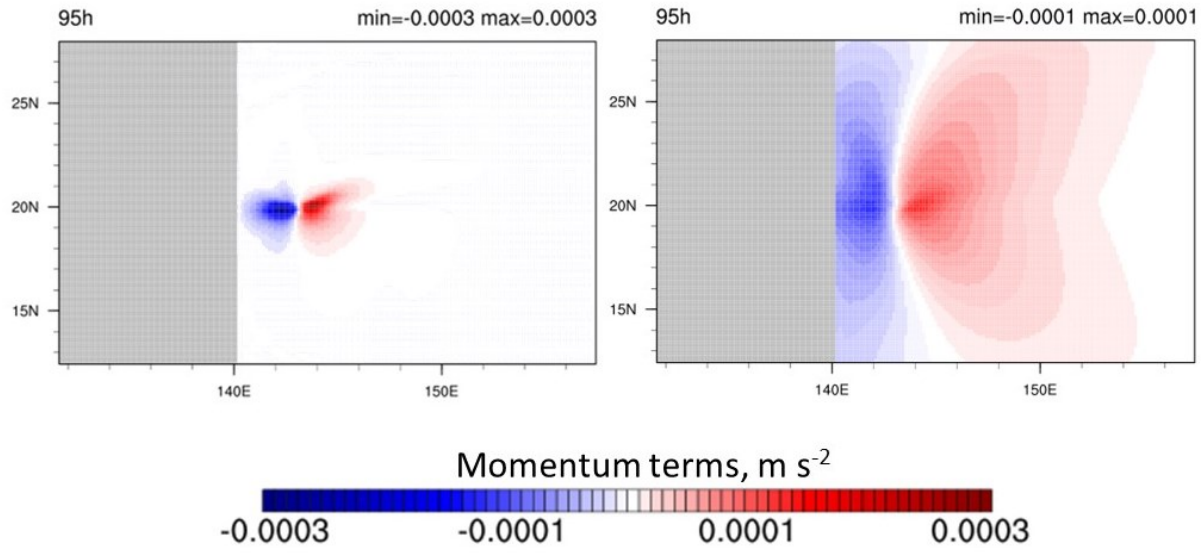


Figure 4.15: Depth averaged momentum terms at 95 h, showing alongshore advection (left) cross-shore Coriolis term (right).

4.4 Conclusion

In this chapter, the asymmetry in positive and negative surges is investigated using idealized experiments. Three cases have been examined. In the first case, the alongshore wind component is removed and the remaining cross-shore wind component created a fairly symmetrical surge pattern. The alongshore wind component plays an important role in strengthening and weakening the positive and negative surges, generating an asymmetry in the magnitude and spatial scale of storm surges. Depending on the direction of the coastal alongshore flow, the alongshore advection affects the magnitude of the positive and negative surges differently. Coriolis force also comes into play by deflecting the coastal alongshore flow to increase or decrease the positive and negative surges. For the positive surge, the coastal SSH response to the alongshore advection and Coriolis deflection oppose each other and the positive surge is altered by a smaller extent compared to the negative surge. For the negative surge, the effects of the alongshore advection and Coriolis deflection complement

each other and the negative surge is affected by a larger extent than the positive surge. In the second case, the effect of the Coriolis force is isolated by translating the simulation domain northwards. As the cyclone approaches the coastline, the direction of the coastal alongshore flow changes. When the coastline is located to the right of the alongshore flow, the increased Coriolis deflection increases the sea level at the coast. The asymmetry in the positive and negative surges weakens. When the coastline is located to the left of the alongshore wind component, the increased Coriolis deflection decreases the sea level at the coast, enhancing the asymmetry in the positive and negative surges. The third case investigates the SSH response in a deeper, sloping ocean floor. The overall SSH response for this case is weaker than the shallower cases and the surge asymmetry decreases, demonstrating the effect of the deeper waters in weakening the SSH response to wind stress. While the significance of the cross-shore winds have been widely known to generate positive and negative surges, the importance of the alongshore winds in generating the asymmetry between the positive and negative surges has been shown here. Simplified storm surge models that only incorporate cross-shore winds to analyse the positive and negative surges would not capture the large asymmetry that exist due to the presence of the alongshore winds.

5 Effect of precipitation on storm surges: Cyclone Monica

5.1 Introduction

Storm surge models typically only incorporate the contributions of the wind-driven effect and the inverted barometer effect [*Roden and Rossby*, 1999], neglecting the contribution from precipitation. As discussed in Chapter 1, ocean circulation models such as ROMS and FVCOM do not incorporate the effect of rain mass, while storm surge models such as ADCIRC and SLOSH do not include the effects of rain at all. For highly precipitating storm systems such as tropical cyclones, the contribution of rainfall to the sea surface elevation may be significant. In Chapter 2, the effects of rain mass have been incorporated into ROMS. Its effect on sea surface elevation was studied using an idealized basin. The effect of rain stress was also investigated, uncovering an oversight in the existing implementation of ROMS which introduced errors to the magnitude and direction of rain stress. This error has since been corrected. In this chapter, the effect of rain mass and rain stress are applied to a real case study to deepen the understanding. The mass and momentum contributions of rainfall to storm surges are compared against the wind and pressure effects to establish their relative significance.

Tropical Cyclone Monica [*Durden*, 2010] has been chosen as a case study here for her high wind speed, low system pressure and high rainfall, which are the key storm surge effects investigated here. Monica is a very intense tropical cyclone, reported as a Category 5 storm on both the Australian Tropical Cyclone Intensity Scale and the Saffir-Simpson Hurricane Wind Scale. According to the cyclone reports from the Australian Bureau of Meteorology

(BOM, http://www.bom.gov.au/cyclone/history/monica.shtml), wind speeds of up to 148 km/h and rainfall of up to 340 mm/day were observed during this event. The minimum sea level pressure of the storm at its peak intensity was estimated by *Durden* [2010] to be between 900 and 920 hPa, although land observations provided by BOM range between 970 hPa and 987 hPa. There has been much debates on the intensity of Monica, with the Cooperative Institute for Meteorological Satellite Studies (CIMSS) Tropical Cyclone Team of the University of Wisconsin-Madison estimating the minimum sea level pressure to be 868.5 hPa (http://tropic.ssec.wisc.edu/real-time/adt/archive2006/23P-list.txt) based on the Advanced Dvorak Technique [*Olander and Velden*, 2007]. This estimation places Monica as more intense than the current world record holder for intensity, Typhoon Tip [*Dunnavan and Diercks*, 1980] at 870 hPa. However, *Durden* [2010] has refuted this claim in his investigation on the intensity of Monica.

Monica first developed as a tropical low in the Coral Sea (Figure 5.1) on 16 April 2006 and moved south-westward. On 17 April 2006, she reached cyclone intensity and moved westward towards Cape York Peninsula. On 19 April 2006 Monica intensified into a Category 2 storm, and made landfall south of Lockhart River. On 20 April 2006 the storm weakened over land and started moving into the Gulf of Carpentaria. Picking up energy from the gulf, the storm quickly intensified into a Category 5 cyclone, reaching wind speeds of 56 m/s and forming a 37 km wide eye in the cyclone centre by 22 April 2006. The cyclone attained its peak intensity on 23 April 2006 as it passed the Wessel Islands with wind speeds of 69 m/s. The weakening of the mid-level ridge to the south of Monica favoured the storm to turn in the south-westward direction on 24 April 2006, making landfall at Junction Bay, west of Maningrida. Upon making landfall, the storm weakened quickly, passing the north of Darwin on 25 April 2006. On 28 April 2006, Monica finally dissipated over central Australia.

Monica crossed Cape York Peninsula at a remote location, avoiding inhabited regions such as Lockhart River and Coen. The coastal crossing points of the cyclone saw severe vegetation damage and there was evidence of 5-6 m storm surge in Junction Bay. The Maningrida community suffered substantial damage in infrastructure, but no casualties were reported. The event inflicted significant and widespread damage across the savannah ecosystems of the Northern Territory [*Cook and Goyens*, 2008].



Figure 5.1: Map of northern Australia showing the geographical landmarks referred to in this case study (Map reproduced with permission from Geoscience Australia http://www.australia.gov.au/topics/science-and-technology/maps-and-mapping).

In this case study, WRF is used to generate a well-validated atmospheric state. This is prescribed onto ROMS to investigate how it affects SSH. The effects of wind stress, inverse barometer effect and the transfer of momentum from rain are already incorporated in ROMS, but corrections have been made to the existing implementation of rain stress as elaborated in Chapter 3. The effect of precipitation mass addition to ROMS has been implemented as described in Chapter 2. The significance of rain mass and rain stress is compared with two

established storm surge processes: the inverse barometer effect and the effect of surface wind. Each of these physical effects is investigated based on their isolated contribution to the total SSH and storm surge patterns.

5.2 Model validation

The atmospheric state is simulated for the period between 20 April 2006 and 24 April 2006. The set-up is discussed in Section 2.3.2. Minimum sea level pressure from WRF is used to generate the cyclone path for comparison as shown in Figure 5.2. This cyclone path is validated using the track provided by BOM, which is based on land radar data. On 20 April 2006, both the modelled cyclone and the observed cyclone are located at the western coast of Cape York Peninsula. The modelled path is largely similar to the observed path, but has a northward offset of up to 1°. The modelled cyclone also travels faster than the observed cyclone by up to a day.

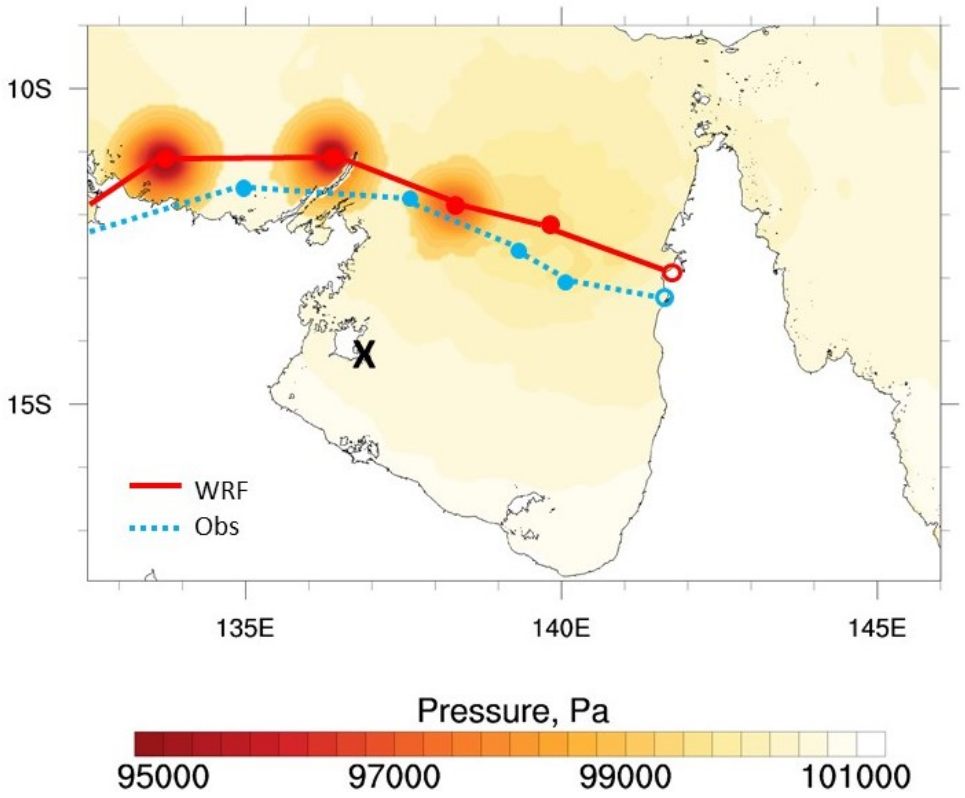


Figure 5.2: Cyclone path of WRF (solid line) and observations from BOM cyclone report (dashed line). Filled circles are positions every 24 hours from 0000 UTC 20 April 2006 (open circle). Location of the Groote Elyandt weather station is indicated with an 'X'.

Precipitation for this event has been compared with the multi-satellite rainfall estimates from the Tropical Rainfall Measuring Mission (TRMM) 3B42 version 6 [*Huffman et al.*, 2007] (Figure 5.3). The modelled rainfall pattern is largely in line with the observed rainfall pattern but the rainfall is more intense within the Gulf of Carpentaria than the area outside the Gulf. WRF has often been reported to overestimate the simulated rainfall. *Marteau et al.* [2015] modelled the rainfall in Burgundy using WRF and the same Kain-Frisch cumulus scheme used in this study. They found that there is an overestimation in rainfall of up to 15% especially during spring and summer when convective rain prevails. WRF performs better in autumn and winter when stratiform rainfall is prevalent. For a tropical cyclone in this case

study, an overestimation in the rainfall simulated using WRF is expected. However, this is not a major concern in this case study since the main objectives are to simulate and compare various processes in a realistic environment and not to closely replicate the exact storm event.

(a) (b)

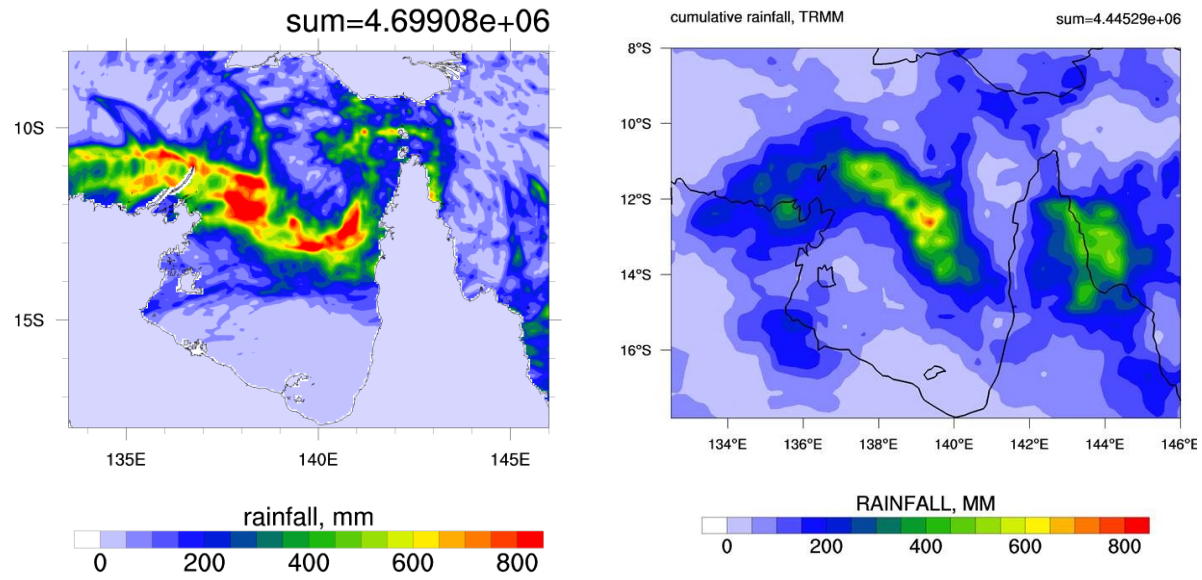


Figure 5.3: 5-Day cumulative rainfall output from 20 April 2006 for (a) WRF and (b) TRMM.

To check that there is still a comparable amount of rainfall introduced to the ocean, the cumulative rainfall is summed spatially for comparison. The total domain cumulative rainfall simulated using WRF is 4.7 x 10^6 mm while that observed in TRMM is 4.4 x 10^6 mm over 5 days. The domain cumulative rainfall in WRF is 6% more than that observed by TRMM, although this percentage is expected to be higher since the WRF rainfall is summed with the land mask applied, while TRMM rainfall is summed over every cell in the domain. The precipitation rates modelled here are not uncommonly high among tropical cyclones in Australia and similar storm systems in other parts of the world. From the BOM reports on historical tropical cyclones, the highest observed precipitation rates of Monica was 340

mm/day, Laurence (December 2009) at 402 mm/day, Paul (March 2010) at 443 mm/day and Yasi (January 2011) at 471 mm/day. The estimated maximum rainfall of Hurricane Katrina (August 2005) was 300 mm/day [*Dodla et al.*, 2011] and Typhoon Morakot (August 2009) was 741 mm/day [*Wu*, 2013]. Hence, the rainfall produced by Monica is not an extreme case compared to other tropical cyclones and the overestimation in the rainfall simulated here does not lead to an unrealistic scenario.

The ocean state is modelled using ROMS, with the set-up described in Section 2.2.3. The configuration of ROMS used for validation incorporating the effects of rain mass, rain stress, the inverse barometer effect and all atmospheric forcings including wind. The storm surge (Figure 5.4) is validated against the tidal gauge measurements taken from Milner Bay in Groote Elyandt. The tidal gauge data is obtained from the Australian Baseline Sea Level Monitoring Project (ABSLMP) [*Watson*, 2011]. To compare the storm surge, the tidal components are detided using the tidal package by *Codiga* [2011]. The tidal range is very large and there remains a residual tidal-like signal after de-tiding eleven tidal components that were introduced into ROMS in the tidal forcing set-up. At this location, the surge simulated in ROMS (23 April 2006) is earlier than the observed data (24 April 2006) by a day. However, the magnitude of the surge is very well captured. The difference in model and observed time of peak surge is also consistent with the different translation speed and track of the WRF cyclone. The modelled cyclone is located north of the Groote Elyandt station around 1200 UTC 22 April 2006, while the observed cyclone reaches north of the Groote Elyandt station around 0000 UTC 24 April 2006. However, the modelled cyclone path is situated more north compared to the observed cyclone path and a longer time is expected for the storm surge to be picked up at Groote Elyandt. Hence, an overall difference of a day can be expected between the modelled and observed storm surge. There is another tidal measurement station available at the Wessel Islands, but the measurements were not available

during the storm event and the week following the event. It is possible that the station was damaged during this storm event.

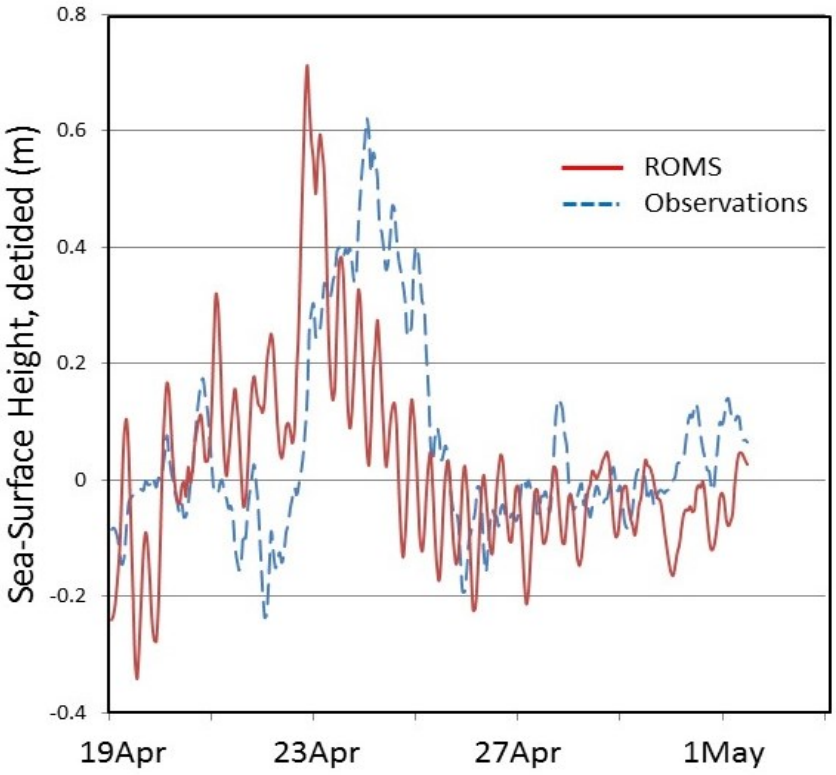


Figure 5.4: Comparison between the storm surge generated in ROMS with tidal gauge measurements (detided) at Groote Elyandt weather station obtained from ABSLMP, with the location indicated with an 'X' on Figure 5.1.

5.3 Results

In this study, a control simulation run is performed using the typical configuration of ROMS: without precipitation mass source, with rain stress, with inverse barometer correction and with wind forcing. The rainfall output from WRF has been reformatted to introduce rain mass as point sources to ROMS. This has been discussed in Chapter 2. The existing implementation of rain stress in ROMS using equations (4.1) and (4.2) are corrected to

equations (4.3) and (4.4). The isolated effects of including precipitation mass source, rain stress, inverse barometer effect and surface wind forcing are individually investigated by comparing with four separate configurations that are simulated with precipitation mass source, without rain stress, without the inverted barometer correction and without surface wind forcing respectively. The five experiments conducted are tabulated in Table 5.1. Spatial plots of SSH are differenced from the control simulation Case A to illustrate the isolated effects of each process. This is explained further in Table 5.2

Cases	***Wind Conditions***	***Inverse barometer effect***	***Rain stress effect***	***New rain mass scheme***
Case A	WRF wind conditions supplied to ROMS	Turned ON in ROMS	Turned ON in ROMS	NOT in use
Case B	No wind supplied to ROMS	Turned ON in ROMS	Turned ON in ROMS	NOT in use
Case C	WRF wind conditions supplied to ROMS	Turned OFF in ROMS	Turned ON in ROMS	NOT in use
Case D	WRF wind conditions supplied to ROMS	Turned ON in ROMS	Turned OFF in ROMS	NOT in use
Case E	WRF wind conditions supplied to ROMS	Turned ON in ROMS	Turned ON in ROMS	In use

Table 5.1: Cases set up with different wind and ROMS model options.

Effect	*Shown in Figure:*	*Obtained by differencing cases:*
Wind	Figure 5.8	Case B – Case A
Inverse barometer	Figure 5.9	Case C – Case A
Rain stress	Figure 5.10	Case D – Case A
Rain mass	Figure 5.11	Case E – Case A

Table 5.2: SSH plots isolating different effects, obtained by differencing plots from different cases.

5.3.1 Wind and ocean currents

Figure 5.5 shows the wind speed at 2 m, with Monica moving westward across the Gulf of Carpentaria towards Darwin. The winds rotate clockwise, gaining speed as the cyclone progresses across the Gulf. Along the coastline around the Gulf, the wind is offshore to the east, alongshore to the south and onshore to the west. The wind is offshore at the northern coast of Arnhem Land.

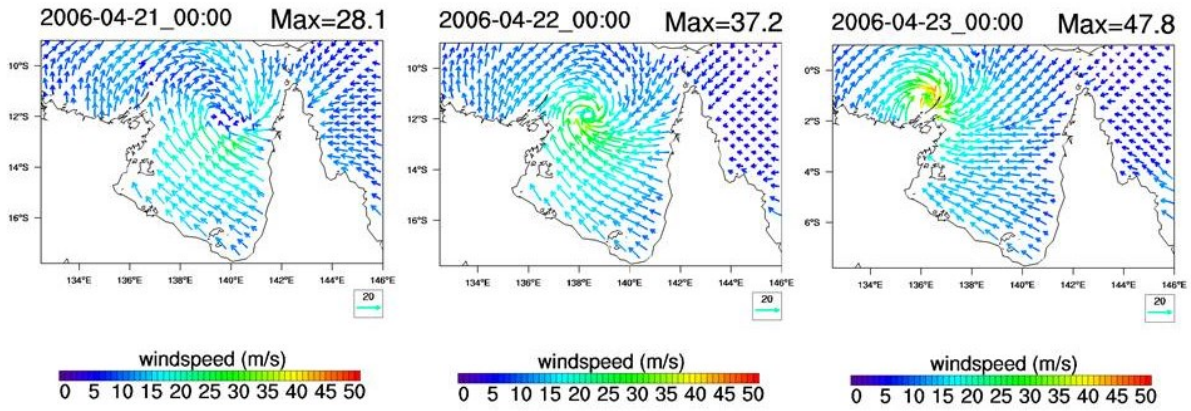


Figure 5.5: 2-m winds from 21 April 2006 to 23 April 2006.

Figure 5.6 shows the sea surface currents rapidly gaining momentum over the 3 days shown, increasing from speeds of 0.1 m/s to as high as 1.5 m/s. Water is being advected into the Gulf from Arafura Sea and the currents converge at the Torres Strait. On 21 April 2006, a clockwise gyre starts forming within the Gulf of Carpentaria. The currents to the north of the Gulf are much stronger than the currents to the south of the Gulf. On 22 April 2006, Monica treks across the Gulf and the clockwise gyre is fully formed in the centre of the Gulf. On 23 April 2006, the cyclone reaches the Wessel Islands and the gyre breaks up into a pair of clockwise gyres on the western and eastern sides of the islands. The main gyre in the middle of the Gulf begins to dissipate as the cyclone tracks across the western boundary. The surface currents along the eastern and southern boundaries of the Gulf weaken, but still follow a general clockwise direction.

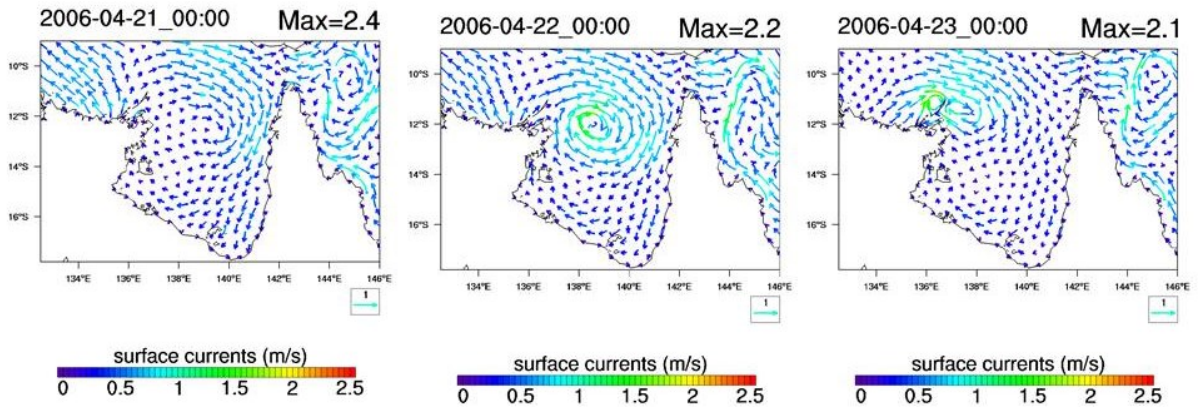


Figure 5.6: Ocean surface currents from 21 April 2006 to 23 April 2006.

The bottom currents in the Gulf of Carpentaria (Figure 5.7) are similar to the surface currents in direction but weaker in magnitude (up to 0.7 m/s). The bottom currents in the Coral Sea remain calm at magnitudes of less than 0.1 m/s. On 21 April 2006, the formation of a clockwise gyre starts within the Gulf with stronger currents at the north compared to the south of the Gulf. On 22 April 2006, a distinct clockwise gyre is formed in the centre of the Gulf. On 23 April 2006, the gyre pair observed at the ocean surface near the Wessel Islands can also be observed at the bottom depths, but are much slower in speed. At this time, the currents to the south of the Gulf quickly revert to a near-stagnant state as they were before the storm hits.

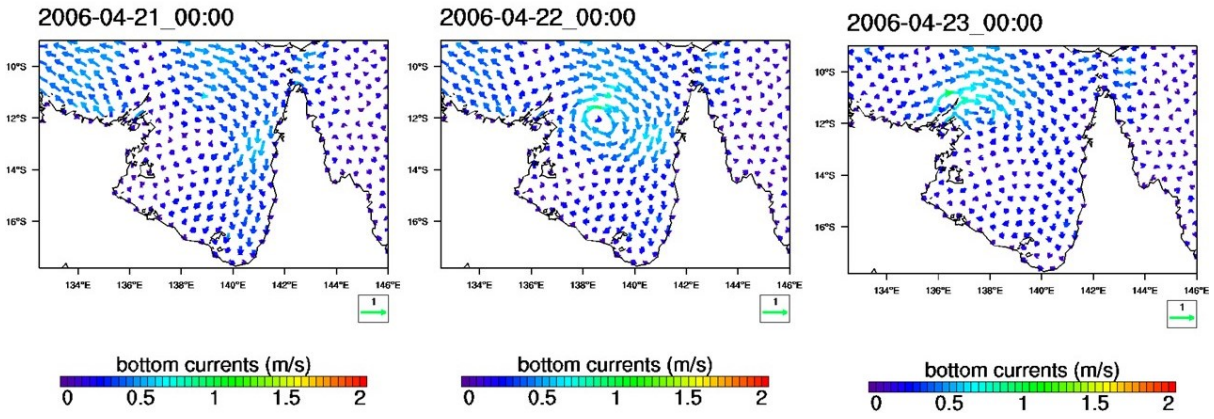


Figure 5.7: Bottom currents from 21 April 2006 to 23 April 2006.

5.3.2 Sea surface height response

The SSH response to the effect of wind (Figure 5.8) is the largest compared to the other effects. On 21 April 2006, the negative surge is up to -58 cm at the eastern boundary of the Gulf of Carpentaria and the positive surge is up to 61 cm on the western boundary. On 22 April 2006, the negative surge at the eastern boundary of the Gulf and the positive surge at the western boundary still persist. There is a region of negative SSH located at the centre of the Gulf. The minimum SSH response is -57 cm and the maximum response SSH is 60 cm. On 23 April 2006, the cyclone reaches the Wessel Islands and the SSH rises up to 171 cm in Buckingham Bay (12°S 136°E). The positive surge at the western boundary of the Gulf is still present at this time, but the negative surge at the eastern boundary has reverted to its nominal levels. At the northern coast of the Arnhem Land, the negative surge is up to -111 cm.

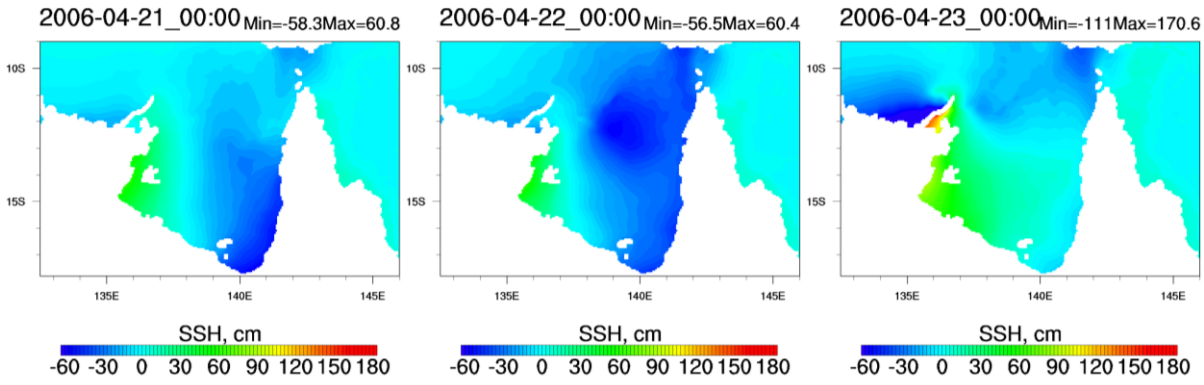


Figure 5.8: SSH response to the effect of wind, from 21 April 2006 to 23 April 2006.

Figure 5.9 shows the SSH change due to the inverted barometer effect. The SSH increase is localized to the position of the cyclone and increases as the cyclone intensifies through the event. The scalar field of the SSH response is similar to atmospheric pressure, with the highest SSH at the centre of the cyclone, gradually decreasing with distance from the cyclone centre. The maximum SSH response increases from 13 cm on 21 April 2006 to 61.5 cm on 23 April 2006 as the cyclone intensifies.

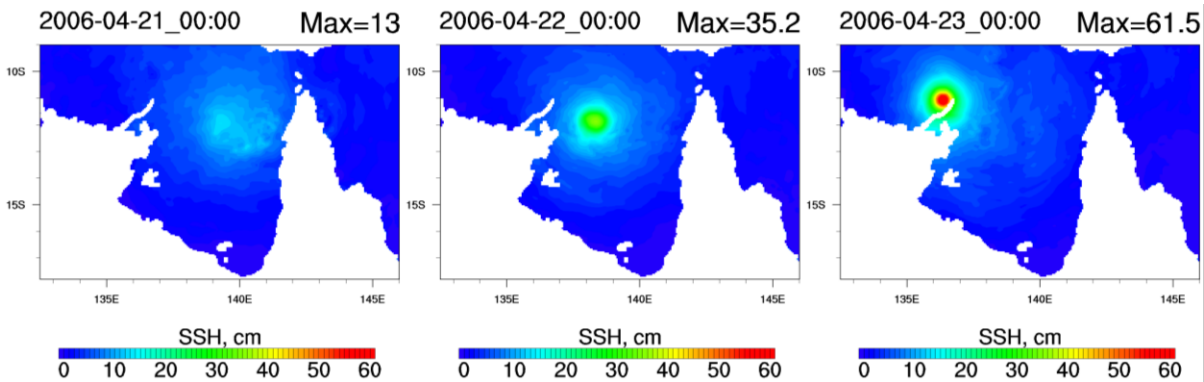


Figure 5.9: SSH response to the inverted barometer effect, from 21 April 2006 to 23 April 2006.

Figure 5.10 shows the additional SSH response due to the effect of rain stress. On 21 April 2006, the negative surge is up to -2.4 cm on west coast of Cape York Peninsula. There is a positive SSH response of up to 0.9 cm near the position of the cyclone centre. On 22 April 2006, when Monica is at the centre of the Gulf of Carpentaria, there is a positive SSH response of up to 0.7 cm ahead of the cyclone and a negative SSH response of up to -1.1 cm behind the cyclone. On 23 April 2006, there is a positive surge of up to 7.5 cm to the east of the Wessel islands and a negative surge of up to -2.9 cm to the west of the islands.

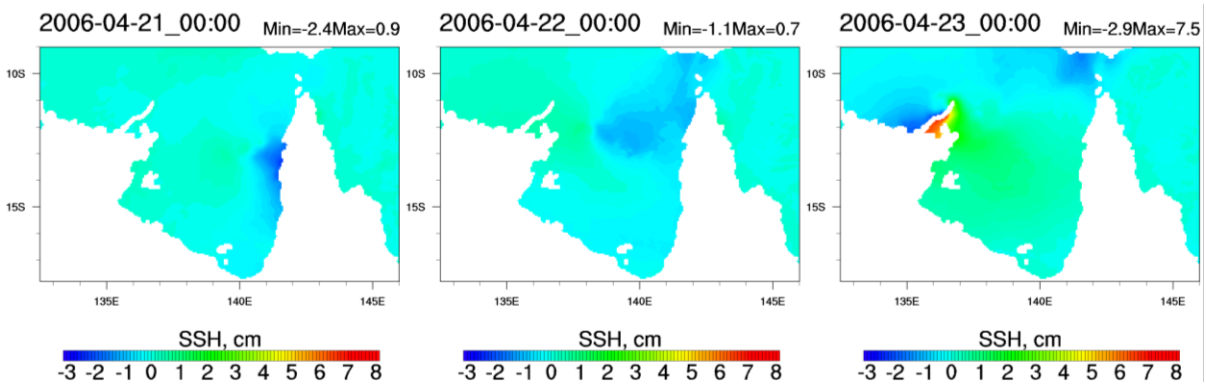


Figure 5.10: Additional SSH response to the effect of rain stress, from 21 April 2006 to 23 April 2006.

Figure 5.11 shows the additional SSH response due to the addition of rain mass, increasing as the cyclone tracks across the Gulf of Carpentaria and decreasing when the cyclone passes. On 21 April 2006, Monica is situated at the western coast of Cape York Peninsula and the SSH rises by up to 3.7 cm at the coast. On 22 April 2006, Monica is centred in the Gulf and the SSH increases up to 4.6 cm, spreading out to the rest of the Gulf. The sea level at the southern boundary of the Gulf increases by up to 3.5 cm. On 23 April 2006, the cyclone reaches the Wessel Islands and the SSH rises by up to 6.4 cm. The sea level change at the southern boundary of the Gulf decreases to 2 cm.

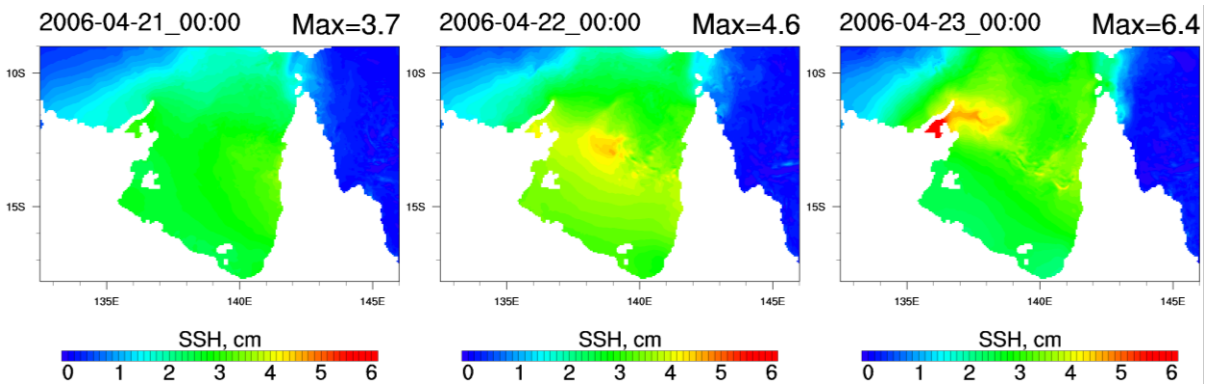


Figure 5.11: Additional SSH response due to rain mass addition, from 21 April 2006 to 23 April 2006.

5.4 Discussion

As Cyclone Monica makes its way across the Gulf of Carpentaria, it draws energy from the Gulf and the wind speed increases as it becomes more intense (Figure 5.5). A clockwise gyre is formed within the Gulf (Figure 5.6) driven by Ekman transfer of momentum from the surface winds to the ocean surface. In the Southern hemisphere, the surface currents are deflected to the left relative to the wind direction. The Gulf of Carpentaria is relatively shallow with an average depth of about 50 m. Certain locations within the Gulf are only as deep as 100 m (Figure 5.12). The coastal regions around the Gulf are as shallow as 10 m. The Ekman depth (d_E) can be estimated as follows [*Stewart*, 2009]:

$$d_E = \frac{0.76U_{10}}{\sqrt{sin|\varphi|}} \qquad (6.1)$$

where U_{10} is the wind speed at 10 m, φ is the latitude and the constant 0.76 is computed using ρ_w = 1027 kg/m^3, ρ_{air} = 1.25 kg/m^3, and $C_D = 2.6\times10^{-3}$. Based on the wind speed and

latitude, the Ekman depth is expected to be deeper than the depth of the Gulf. Hence, the effect of wind stress is expected to be significant throughout the depths of the Gulf, with a balance between the pressure gradient, Coriolis force and turbulent drag.

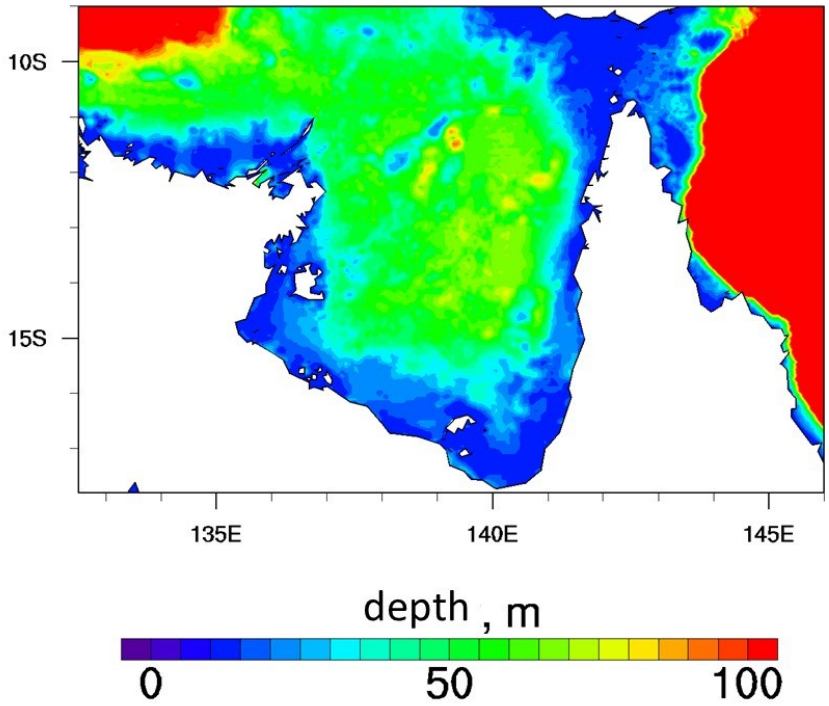


Figure 5.12: Bathymetry at the Gulf of Carpentaria.

Torres Strait is a narrow and shallow channel that connects the Pacific Ocean and Indian Ocean. The two oceans have different mean sea levels, oceanic circulation patterns and tidal regimes. The difference in mean sea levels creates a westward current flowing from the Coral Sea through the Torres Strait, Gulf of Carpentaria and into the Arafura Sea. During this storm event, the clockwise gyre in the Gulf creates an eastward current to the north of the Gulf and the two flows converge at the strait. The Coral Sea is adjacent to the Sahul continental shelf and is up to 3000 m deep in the domain. There is a semi-permanent clockwise gyre at the Coral Sea that can be traced back to the South Equatorial Current [*Kessler and Cravatte*, 2013]. This gyre is only a surface flow and is absent at the ocean bottom (Figure 5.7).

The effect of wind is larger than the effect of precipitation and the inverse barometer effect. It drives the SSH positively and negatively based on the wind direction and the geometry of the coastline. On 21 April 2006, the strong easterly wind to the south of the domain generates a positive surge at the western boundary of the Gulf of Carpentaria due to the onshore wind. A negative surge is generated at the eastern boundary of the Gulf due to the offshore wind. On 22 April 2006, the easterly wind to the south of the domain continues to generate a positive and negative surge at the western and eastern boundaries of the Gulf respectively. There is a SSH depression in the middle of the Gulf due to Ekman pumping (Section 1.2.1). This SSH depression is present in all the 6-hourly output from 1800 UTC 21 April 2006 to 1800 UTC 22 April 2006 when Monica is trekking across the Gulf of Carpentaria. The SSH depression is absent on 21 April 2006 and 23 April 2006 in Figure 5.8 when the cyclone is near Cape York Peninsula and the Wessel Islands respectively. On 23 April 2006, the cyclone is relatively far from the eastern boundary of the Gulf and the offshore winds here weaken from approximately 15 m/s (21 April 2006) to 10 m/s (Figure 5.8). The negative surge at the eastern boundary of the Gulf weakens correspondingly. On the other hand, the positive surge at the western boundary of the Gulf strengthens with the strong onshore winds. At this time, the strong winds blowing into Buckingham Bay create a funnelling effect, channelling water into the bay and generating a positive surge of up to 171 cm.

The SSH response to the inverse barometer effect is spatially influenced by the location of the cyclone's low pressure centre and varies in magnitude based on the storm intensity (Figure 5.9). As discussed in Section 1.2.2, SSH is expected to increase by 1 cm for every 1 mbar drop in atmospheric pressure. The inverse barometer effect contributes substantially to the storm surge when the low pressure centre of the cyclone coincides with the coastline. When the cyclone is away from the coastline and over the open sea, the inverse barometer effect raises the SSH but does not contribute significantly to the storm surge. On 21 April

2006, Monica crosses the west coast of Cape York Peninsula but due to its low intensity at this time, the contribution to the storm surge is only up to 13 cm. On 22 April 2006, the storm intensifies as it crosses the Gulf of Carpentaria but due to its distance from the coast, the contribution to the storm surge is only around 10 cm, despite raising the SSH up to 35.2 cm in the centre of the Gulf. On 23 April 2006, Monica intensifies further, crossing the Wessel Islands and increasing the storm surge by up to 61.5 cm.

A region is subjected to rain stress when rainfall coincides with the winds. On 21 April 2006, the location of intense rain is situated just off the west coast of Cape York Peninsula. The cyclone is traversing westward due to the overall westward wind direction. Rain stress perturbation on the sea surface creates a positive front ahead of the perturbation and a negative front behind it as shown in Figure 3.14. The offshore winds and high rainfall at the eastern boundary of the Gulf generates a SSH response to rain stress, enhancing the negative surge here. As the rainfall is significantly lower at the locations where the wind stress created the positive and negative surges at the western and eastern boundaries of the Gulf of Carpentaria, these surges are absent in the rain stress effect shown here. On 22 April 2006, the cyclone is in the middle of the Gulf trekking westwards. This creates a similar effect with the positive SSH response ahead of the cyclone and a negative SSH response behind it. The positive and negative surges at the western and eastern boundary of the Gulf are similarly absent here, due to the light rainfall in these areas. On 23 April 2006 when the cyclone crosses the Wessel Islands, the effect of rain stress is very similar to that of the wind stress due to the intense rain falling in the vicinity of these islands, coinciding with the strong winds. There is an additional positive surge of up to 7.5 cm in Buckingham Bay due to the rain stress channelling water into the bay in a similar manner as the SSH response to wind stress. At the northern coast of the Arnhem Land west of the Wessel Islands, the offshore

winds coincide with the high rainfall from the storm to generate an offshore rain stress and a negative surge of up to -2.9 cm.

Figure 5.11 shows the SSH response to precipitation mass addition. The areas of SSH change are not solely confined to the precipitation footprint as traced out in Figure 5.3, but spreads out, advecting to the south of the Gulf of Carpentaria. On 21 April 2006, the cyclone is located just off the western coast of Cape York Peninsula and the effect of rain mass is predominantly along the cyclone track, towards the centre of the Gulf. On 22 April 2006, the clockwise gyre fully develops and continues to advect the additional mass southwards into the Gulf. On 23 April 2006, the cyclone crosses the Wessel Islands and the rain mass is trapped in Buckingham Bay, slowly advecting outwards in the northeast-ward direction and generating an additional local SSH increase of 6.4 cm. The effect of precipitation is essentially an in-situ addition of mass, and inlets and semi-enclosed basins serve to enhance this effect by trapping the rain. Buckingham Bay is fairly well resolved in this 6 km resolution model, spanning 13 x 14 grid cells, so the size of the effect is unlikely to be just numerical. The geometry of the Gulf itself is an important contributing factor towards the effect of precipitation seen here. From Figure 5.11, it can be seen that the SSH response is generally higher in the southern half of the Gulf than the north. If the Gulf was entirely enclosed, the additional mass will be expected to be distributed evenly by the clockwise gyre in both the northern and southern regions. The constrained southern boundary of the Gulf enhances the build-up of SSH within the Gulf, since the north-western section of the Gulf opens up to the Arafura Sea. Typical remote enhancements are of the order of 2 cm.

The systematic bias from the effect of rainfall can be placed in context with other sources of error that has been previously quantified. *Lewis et al*. [2014] investigated how natural variability of cyclone parameters can translate into large uncertainties for the peak storm

surge height and coastal inundation. Using a series of idealized simulations, different cyclone parameters are varied, namely the location of cyclone genesis, the location of landfall, the angle that the cyclone makes landfall, cyclone development parameters (δP·δt and δRMAX·δt), the mean cyclone track speed and the peak cyclone pressure change. The peak storm surge difference resulting from this variation is summarized in Table 5.3 together with the peak storm surge difference resulting from the effect of wind speed, atmospheric pressure, rain stress and rain mass presented in this Chapter. The study by *Lewis et al*. [2014] has perturbed various cyclone parameters to look at the uncertainties this will bring to the peak storm surge simulated. This is not a direct comparison to the results in this Chapter, which shows the extent that the storm surge can be affected by the presence/absence of a particular effect. However, it does provide context to the magnitude of the effect shown here. When the peak cyclone pressure drop is varied between 56.2 hPa and 81.2 hPa, the peak storm surge difference amounted to 277 cm. Decreasing the peak cyclone pressure drop increases the wind speed of the cyclone, which can cause a change in the peak storm surge difference due to the wind and inverse barometer effect. Varying the cyclone landfall location is expected to lead to significant differences in the peak storm surge generated (89 cm) since this is subjecting the cyclone to an entirely different coastal geometry and bathymetry. Varying the angle that the cyclone makes landfall generated a peak storm surge difference of 7 cm while perturbing the cyclone development parameters (δP·δt and δRMAX·δt) does not make a significant change to the peak storm surge. In the case study of Cyclone Monica, the effect of rainfall (rain stress and rain mass) generated a peak storm surge difference of 13.9 cm, which is significant compared to the uncertainties quantified by *Lewis et al*. [2014]. On top of this, the effect of rain mass is not an uncertainty, but a systematic bias that will be under-estimated if this effect is not considered.

	Parameter	Ranges from	Ranges to	Peak storm surge difference (cm)
1.	Cyclone location of genesis	93.2°E 9.6°N	87.5°E 10°N	51
2.	Landfall location	±26 km from standard landfall position (89.76°E 21.75°N)		89
3.	Angle that cyclone makes landfall	291°N	43°N	7
4.	Cyclone development parameter, δP·δt (pre-landfall and post-landfall)	0.67 and -3.00 hPa h^{-1}	0.33 and -0.34 hPa h^{-1}	0
5.	Cyclone development parameter, δRMAX·δt (pre-landfall and post-landfall)	-0.34 and 2.00 km h^{-1}	0 and 0.34 km h^{-1}	0
6.	Mean cyclone track speed (pre-landfall, post-landfall)	4.8 and 9.8 m s^{-1}	2.8 and 3.6 m s^{-1}	139
7.	Peak ΔP	56.2 hPa	81.2 hPa	277
8.	Effect of windspeed	-	-	171.0
9.	Effect of atmospheric pressure	-	-	61.5
10.	Effect of rain stress	-	-	7.5
11.	Effect of rain mass	-	-	6.4

Table 5.3: Broad comparison of the error in the peak storm surge differences, associated with various parameters affecting storm surges. Parameters 1 to 7 are from the case study of Cyclone Sidr [*Lewis et al*., 2014], parameters 8 – 11 are from the case study of Cyclone Monica in Chapter 5 within this thesis.

The Gulf of Carpentaria is not an isolated case of a semi-enclosed basin that is prone to severe storms and many other cases have been studied. *Zhong et al.* [2010] used ROMS to study the storm surge predictions during the passage of Hurricane Isabel in Chesapeake Bay and found that the hurricane translation speed and the resolution of the horizontal wind field are important factors affecting storm surges. *Rego and Li* [2010] used FVCOM to simulate Hurricane Ike at Galveston Bay and found that shown that the Bolivar Peninsula provided a significant surge barrier in protecting the bay. By reducing the height of the Bolivar Peninsula by 45%, the bay was exposed to surge levels similar to a case where the height of the peninsula was set to 0.05 m above mean sea level. *Westerink et al.* [2008] developed a model of south Louisiana (which included many inlets, bays and channels) using ADCIRC to simulate the effect of storm surges during Hurricane Betsy and Andrew. *Weisberg and Zheng* [2006] used FVCOM to simulate the storm surge produced from several idealized hurricanes crossing Tampa Bay and found that the hurricanes with slow transitional speeds produced larger surges within the bay. However, none of these studies or models include the effect of rain mass. The semi-enclosed bay comprising Buckingham Bay, extending to the Wessel Islands and Gove Peninsula (12°2'S 136°5'E) consists of about 250 model cells, which is equivalent to an area of 9000 km^2. The areas investigated in literature, such as Tampa Bay (5700 km^2), Galveston Bay (1600 km^2) and Chesapeake Bay (11600 km^2) are all of similar sizes or smaller. Not including the effect of rain mass in the models used in these studies will introduce a systematic error in the modelled storm surge levels.

To further compare how each of the physical effects contribute to coastal impacts in a worst case scenario, the SSH at the coast starting from the Wessel Islands and ending at the northern tip of Cape York Peninsula (highlighted in red in Figure 5.13) is investigated. The coastal points can be attributed to different locations along the coastline as follows: the

Wessel Islands (points 1 – 120), the western boundary of the Gulf of Carpentaria (points 121 – 180), the southern boundary of the Gulf (points 181 – 280) and the eastern boundary of the Gulf (points 281 – 450).



Figure 5.13: Map of northern Australia (from Figure 5.1) showing the coastline (in red) analysed for coastal impact.

The maximum storm surge (for the duration of the storm) due to each physical effect is shown against the coastal locations (Figure 5.14) to illustrate the worst case scenario that can arise from each effect during this event. Considering the maximum storm surge response to the different processes at each coastal point, the effect of rain mass ranges from 1.3 cm to 6.4 cm, the effect of rain stress is from 0.4 cm to 7.5 cm, the inverse barometer effect is from 0.2 cm to 45.4 cm and the effect of wind stress is from 20.5 cm to 170.6 cm. While the maximum surge levels due to the effect of rain stress are higher than the effect of rain mass, Figure 5.14 shows that the effect of rain mass is larger than the effect of rain stress at most of the coastal points. ROMS (and many ocean models) include the effect of rain stress but not the rain mass even when the effect of rain mass can be larger as shown here. Ocean models that consider

the effect of rain stress to be sufficiently substantial to include its effect should not neglect the effect of rain mass. While the coastal SSH response to the inverse barometer is large, it falls below the SSH response to rain mass at the southern boundary of the Gulf (coastal points 180 – 330) when the cyclone is located away from the coastline. This shows that the effect of rain mass has a stronger remote presence.

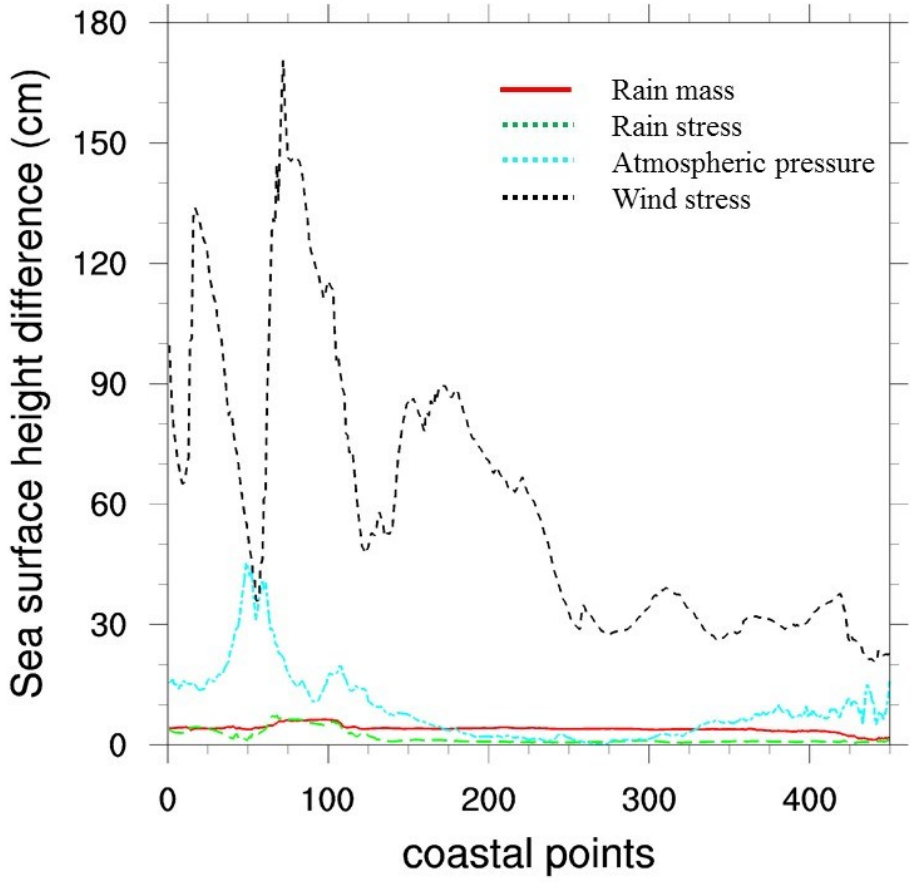


Figure 5.14: Comparison of the SSH change due to various physical effects, along the coastline highlighted in red in Figure 5.13.

Finally, the different processes are compared against wind stress, since the effect of wind stress on storm surges has the largest and most significant impact. At each location, the maximum surge response of each process is expressed as a percentage of the maximum surge response to wind stress. The storm surge generated by the inverse barometer effect, can be up

to 100% that of wind stress. This occurs at the northern section of the Wessel Islands where the storm surge generated by the wind stress drops substantially due to the narrow coastline at this area. In the situation where the geometry of the coastline does not favour the increase in storm surge due to wind stress but the cyclone is in close proximity of the coastline, the effect of the inverse barometer effect can hence be as large as the effect of wind stress. The storm surge generated by the effect of rain stress can be up to 8% of wind stress. Similarly in the northern section of the Wessel Islands, the storm surge generated by the wind stress drops substantially while rain stress is increased due to the high rainfall and wind speed here. The storm surge generated by the effect of rain mass can be up to 15% of wind stress. This is located at the eastern boundary of the Gulf of Carpentaria, where the wind is largely offshore and the storm surge due to the winds is not high (coastal point 340).

5.5 Conclusion

In this concluding chapter, four processes contributing to storm surges are compared and contrasted, namely the wind-driven effect, inverse barometer effect, momentum transfer from rainfall and the effect of adding rain mass. These processes are studied in a real case study based on the tropical cyclone Monica. WRF is used to simulate this event, prescribing a well-validated and high resolution tropical cyclone to ROMS.

The wind effect is the largest, driving the SSH positively and negatively based on the locations of the onshore and offshore winds. The inverse barometer effect is localised to the low pressure of the cyclone and varies in magnitude and location based on the intensity and the path of the cyclone. While the effect of the inverse barometer effect on storm surges is large (after the effect of winds), its contribution to coastal surges can be diminished when the storm is located away from the coast. The effect of rain stress is similar to the wind effect in

generating positive and negative surges through onshore and offshore rain stresses. However, its effect is only substantial in locations with high wind speeds and intense rainfall. The effect of precipitation mass is shown to be the result of in-situ addition of mass. Coastal inlets are significant in enhancing the effects of precipitation mass on SSH as illustrated when the tropical cyclone passes Buckingham Bay and intense rain is introduced. The effect of rain mass has a strong remote presence, especially in semi-enclosed areas. It can systematically contribute to the storm surge even when the storm is considerably far from the coast that the inverse barometer effect and the effect of rain stress are no longer substantial. Many ocean models include the effect of rain stress but neglect the effect of rain mass. However, the effect of rain mass on coastal surge levels is generally larger than the effect of rain stress in this case study. Hence, the effect of rain mass should not be neglected especially in studies and models that find the effect of rain stress substantial enough to be included.

Using the effect of wind as a benchmark, each process is compared at locations along the coastline. In the worst case scenario, the inverse barometer effect can be as large as the wind effect, the effect of rain stress can be up to 8% that of the wind effect and the effect of rain mass can be up to 15% that of the effect of wind. More importantly, each effect has shown to have different spatial extent and influences. The implications of the different spatial response is that the precipitation effect cannot simply be accounted for in surge models through, for example, increasing the model wind field to recalibrate against surge observations. Coastal protection solely based on the effects of wind can run into worst case scenarios where the effect of wind is low and the neglected processes become significant. In these cases, the storm surge predicted can be substantially underestimated.

This case study is not a unique and extreme example. Cyclone Monica produces a maximum rain rate that is similar to Hurricane Katrina and only half of Typhoon Morakot. For tropical

cyclones with a more intense rainfall, this effect may be larger. Buckingham Bay has similar characteristics to many well-studied regions in the world that are prone to storm surges, such as Chesapeake Bay, Galveston Bay and Tampa Bay. These bays are shallow, have a semi-enclosed structure and often find themselves in the path of tropical cyclones. By ignoring the effect of rain, modelling studies of these regions are likely to have a systematic bias in the storm surge height estimated.

6 Summary and final conclusions

Precipitation is often thought to be insignificant when compared to the vast ocean body. Yet many studies in the past decades have shown how the cooler and fresher rainwater can substantially affect processes in the ocean by altering its temperature and salinity. However, studies on the contribution of rainfall are sparse and its effect continues to be neglected. Severe storms such as tropical and extratropical cyclones can produce large amounts of rainfall but it is not known how substantial its contribution to sea surface heights may be. Modelling of severe storms and storm surges is critical due to the devastation and fatalities these events can cause. Historical storm surge events show that a difference of mere centimetres in the storm surge levels can make or break coastal protection. Yet, ocean circulation models such as ROMS and FVCOM do not include the effects of rain mass and storm surge models such as SLOSH and ADCIRC do not include the effects of rain at all. Internationally, the choice of storm surge modelling system is very varied, spanning from models with a simplified physics representation, to ensemble methods based on full hydrodynamic models. While each model has their own strengths and shortfalls, common challenges faced by many storm surge modelling systems include the need for accurate prediction of cyclone parameters, high resolution coastal data and to incorporate a more comprehensive physics representation.

Whether the incorporation of more physics necessarily improves model skill has been widely discussed. The complexity of storm surge prediction techniques can range from empirical relationships involving little or no physics (e.g. *Jan et. al*. [2006]), to simple storm surge models with basic physics representation and fast computation time (e.g. SLOSH), to full hydrodynamic models (e.g. ROMS) requiring substantially more time and computational

power. While increasing the complexity of the models improves the representation of the physical processes involved, it does increase the uncertainties. For instance, incorporating a rainfall scheme does subject the model to the need for accurate and reliable rainfall forcing. However, this is not unlike the need for storm surge models to require accurate and reliable input parameters such as wind field or atmospheric pressure. If there is high confidence in the predicted atmospheric state, raising the complexity of the surge model can provide a better representation of the storm surge. Conversely, if the predicted atmospheric state is likely to generate high levels of uncertainties, selecting a simpler approach may be more suitable. The onus is on the forecaster to employ a suitable model based on the objectives, limitations in time, requirements in the quality of physics representation in the model, reliability of input parameters, uncertainties involved, etc. While this thesis does not aim to advise on the suitability of different surge models and how incorporating any type of physics representation necessarily improves the model skill, it does address the gap that there is no existing rainfall scheme that incorporates the mass of rainfall, and report the amount of bias a model can have in the absence of such a rainfall scheme.

In Chapter 2, the atmospheric model WRF and the ocean model ROMS employed in this study are introduced. Rain mass is incorporated into a new scheme for ROMS that adds rain mass as point sources. This is similar to how river sources are added to the model, but in this case, vertical fluxes are introduced instead of horizontal fluxes. Chapter 3 shows the effect of precipitation mass and momentum on the sea surface. An idealized tropical cyclone with a maximum cumulative rainfall of 32 cm is simulated using WRF and used as an atmospheric forcing for ROMS. When rain mass is added to the sea surface, it spreads rapidly outwards from the point sources as surface gravity waves. The surface gravity waves have a propagation speed that is proportional to the square root of water depth. The surface winds

are removed from the idealized set-up to study the spread of the rain mass introduced to system. Here, the SSH increases by up to 5.8 cm after 170 hours in a closed basin with a dimension 30° by 40° and 100 m in depth. Increasing the ocean depth to 1000 m increases the propagation speed of the surface gravity waves and reduces the maximum SSH response to 3.2 cm. With the increased spreading in the deep ocean, the minimum SSH response increases to 2.3 cm, from 1.3 cm in the shallow case. At the time scale of several days, the SSH rise due to the added rain mass created an outward-directing pressure gradient from the source of the rain mass. With geostrophic adjustment, the pressure gradient is balanced by Coriolis force that is opposite in direction. In the Northern Hemisphere, the geostrophic currents generated rotate in the clockwise direction. As the cyclone treks westwards and making landfall, the added rain mass diverges from the coastline and is deflected to the right by Coriolis force. This increases the SSH to the left of the cyclone's path more than its right. For a tropical cyclone making landfall in the Northern hemisphere, the onshore and offshore winds create positive and negative surges respectively. The added rain mass contributes to this effect by decreasing the magnitude of negative surge more than it increases the positive surge.

The existing implementation of rainfall in ROMS considers the temperature and salinity effects of rainfall but not its mass. On the other hand, the new rainfall scheme considers the mass effect of rainfall, but not the temperature and salinity effects. These two implementations are investigated separately to understand their individual response. When forced by the rainfall of an idealized tropical cyclone for 7 days, the existing ROMS set-up responds to the rainfall with a cooling of the SST of up to 1.22°C and a freshening of the SSS of up to 1.85 psu from the ambient conditions. The SSH increase is minimal. The ROMS set-up using the new rainfall scheme responds to the same rainfall forcing with a SSH increase of

up to 5.8 cm, and no substantial response in temperature and salinity. The point source implementation of rainfall serves to complement the existing ROMS code by incorporating the sea surface response to rain mass without interfering with the existing response to temperature and salinity. This new rainfall scheme should be implemented together with the existing set-up of ROMS to incorporate the temperature, salinity and mass effects of rainfall.

Next, the momentum transfer from rainfall to the ocean surface is investigated. *Caldwell and Elliott* [1970] parameterized rain stress as a function of rain rate and wind speed and it is widely adopted by many models including ROMS. However, the isolated effect of this parameterization has never been investigated in the models it was incorporated into. Here, an idealized set-up of ROMS is used to study the effects of rain stress. A single-point rain stress perturbation to the free surface generates a surface gravity wave that propagates radially outwards from the point of perturbation. A positive front propagated in the direction of the surface wind, while a negative front propagated in the opposite direction. Through this idealized study, an oversight in the existing implementation of rain stress in the ROMS code is uncovered. Using the existing implementation, a single-point rain stress perturbation generated a surface gravity wave that propagates at an angle of 45° to the wind direction. This error yields a systematic overestimation of 41% in magnitude and up to 45° in direction. With this error corrected, the isolated effect of rain stress on storm surges is by forcing an idealized set-up of ROMS with an idealized tropical cyclone generated by WRF. The response of SSH and sea surface currents to rain stress is very similar to wind stress. Ekman pumping is generated from the anticlockwise rotating rain stress in the Northern Hemisphere. When the cyclone makes landfall, the onshore and offshore rain stress generate positive and negative surges respectively. There is an asymmetry generated between the magnitudes of the positive and negative surges. This asymmetry is further examined in Chapter 4.

In Chapter 4, the asymmetry in positive and negative surges is investigated. Wind stress is widely known to be the main driver of storm surges. Simplistically, the onshore and offshore winds generate positive and negative surges respectively. However, studies reported an asymmetry between the magnitudes of the positive and negative surges despite having a relatively symmetrical wind field. An idealized set-up of ROMS is forced by an axisymmetric rotating wind to investigate this asymmetry. When the ocean is forced only by the cross-shore winds, the asymmetry decreases from a factor of 2.5 to 1.2, showing the importance of the alongshore winds in contributing to the asymmetry. This is due to Coriolis force deflecting the alongshore stresses as shown when the asymmetry increases from a factor of 2.5 to 3.2 when the ocean domain is translated northwards by 10°. On top of this, the alongshore winds advect water along the coastline, further enhancing or reducing the asymmetry depending on its direction. For the positive surge, the effect of Coriolis force deflecting the alongshore flow and the effect of the alongshore advection opposes each other, affecting the positive surge by a smaller extent compared to the negative surge. For the negative surge, the two effects complement each other to enhance the negative surge by a larger extent compared to the positive surge, creating the asymmetry. In a sloping bathymetry scenario, the asymmetry lowers from a factor of 2.5 to 1.7. This shows the effect of the deeper waters in weakening the sea surface height response to wind stress.

Chapter 5 compares the different processes that affect storm surges in a realistic case study of tropical cyclone Monica making landfall in Northern Australia in 2006. The WRF model is used to simulate and prescribe a well-validated and high resolution tropical cyclone to the ocean model ROMS. The SSH response to the effects of precipitation mass source, momentum transfer from rain, inverse barometer correction and the surface wind forcing is isolated and compared with. The effect of wind stress is the largest, generating positive and

negative surges based on the coastal geometry. In this case, the wind effect generated a positive surge of up to 170.6 cm when the strong winds converges the currents into Buckingham Bay. A negative surge of up to -111 cm is generated to the north of Arnhem Land where the winds are blowing offshore. The SSH response to the inverse barometer effect is localised to the low pressure of the cyclone and affect the storm surge when the cyclone is near the coastline. As the cyclone treks across the Gulf of Carpentaria, it draws energy and intensifying as it reaches the Wessel Islands. Here, the SSH response to the inverse barometer effect is the largest at 61.5 cm. The SSH respond strongly to rain stress at locations where intense winds coincide with heavy rain. The maximum SSH increase due to rain stress is 7.5 cm, occurring at Buckingham Bay. The effect of rain mass on SSH is an in-situ addition of mass, influenced by advection and convergence. The geometry of the coastline can affect the SSH response to rain mass, enhancing the mass build-up in semi-enclosed bays such as Buckingham Bay. In this case study, the effect of rain mass increases the SSH up to 6.4 cm in Buckingham Bay. The effect of rain mass has a stronger remote presence compared to the effect of rain stress and the inverse barometer effect. Especially in semi-enclosed areas, the effect of rain mass can contribute to the storm surge substantially even when the storm is relatively far from the coastline, and the effect of rain stress and inverse barometer effect are no longer significant.

Lastly, the different processes are compared with the effect of wind as a benchmark. Considering the worst case scenario at each coastal point, the inverse barometer effect can be as large as the wind effect, the effect of rain stress is up to 8% of the effect of wind and the effect of rain mass is up to 15% of the effect of wind. Each process shows different spatial influence and cannot be accounted for by simply scaling up a certain effect, for example, recalibrating the surge model by scaling the wind field. Cyclone Monica is not an extreme rainfall case, generating a maximum rain rate similar to Hurricane Katrina and only half of

Typhoon Morakot. For tropical cyclones with a more intense rainfall, the effect of rain on SSH may be larger than that illustrated here. Buckingham Bay share similar characteristics as regions in the world that are widely studied for storm surges. Chesapeake Bay, Galveston Bay and Tampa Bay are all shallow, semi-enclosed bays that were in the path of tropical cyclones historically. By ignoring the effect of rain mass, storm surge studies of these regions are likely to have a systematic negative bias in the storm surge height investigated.

This piece of work fills the research gap where the effect of rain mass on sea surface elevation was previously unquantified. A new rainfall scheme is set up in the ocean model ROMS to include the mass effect of rain. The parameterization of rain stress is in many studies but its isolated effect on sea surface height has not been shown until now. It is not surprising then, that an oversight in the existing implementation of rain stress in ROMS has not been uncovered. While the asymmetry in positive and negative surges is noted in several studies, the importance of the alongshore winds and the significance of Coriolis force in creating this asymmetry has not been demonstrated. In addition to understanding the effects of rain mass, it is shown that it can be a non-negligible process in the context of storm surges when compared to other established storm surge processes such as wind stress, atmospheric pressure effect and rain stress. In the case study examined here, the effect of rain mass can contribute to the storm surge by up to 6.4 cm and in the worst-case scenario, has an effect on storm surges that is up to 15% of the wind effect. Where mere centimetres can make or break the protection against storm surges, the effect of rain mass should always be incorporated. With 44% of the world's population living within 150 km from the coast [*Resio and Westerink*, 2008] and increasing, storm surges are becoming an increasing threat. In a warming climate, tropical cyclones are expected to increase in rainfall rates of the order of 20% within 100 km of the cyclone centre [*Knutson et al.*, 2010]. If storm surge models

continue to ignore the contribution of rainfall, a substantial component of storm surges will not be accounted for.

In this thesis, the effect of wind, atmospheric pressure and rainfall on storm surges has been compared and quantified. On top of these effects, *Harris* [1963] identified the effect of waves to be one of the important processes contributing to storm surges. The background on the effect of surface waves has been discussed in Section 1.4.3. In the case of severe storms with high speed winds, *Moon et al*. [2003] have shown there is a spatial variability in the drag coefficient by coupling the ocean model with a wave model. Additional studies on the effect of radiation stress [*Mastenbroek et al.,* 1993] and wave set-up [*Kim et al.,* 2010] have also been discussed. These various wave effects can be incorporated in future comparisons to enhance the comprehensiveness of this study. The modelling system used in this thesis, COAWST, is capable of coupling WRF, ROMS and SWAN and will provide an integrated platform for this work.

7 Biblography

Andreas, E. L. (2004), Spray stress revisited, *J Phys Oceanogr*, *34*(6), 1429-1440, Doi 10.1175/1520-0485(2004)034<1429:Ssr>2.0.Co;2.

Arakawa, A., and V. R. Lamb (1977), Methods of computational physics, *Academic Press*, 174-265.

AsSalek, J. A. (1997), Negative surges in the Meghna estuary in Bangladesh, *Mon Weather Rev*, *125*(7), 1638-1648, Doi 10.1175/1520-0493(1997)125<1638:Nsitme>2.0.Co;2.

Bao, S. W., L. Xie, and S. Raman (2004), A numerical study of a TOGA-COARE squall-line using a coupled mesoscale atmosphere-ocean model, *Advances in Atmospheric Sciences*, *21*(5), 708-716, Doi 10.1007/Bf02916368.

Baxter, P. J. (2005), The east coast Big Flood, 31 January-1 February 1953: a summary of the human disaster, *Philos T Roy Soc A*, *363*(1831), 1293-1312, DOI 10.1098/rsta.2005.1569.

Berliand, M. E., and T. G. Berliand (1952), Measurement of the effective radiation of the Earth with varying cloud amounts, *Izv. Akad. Nauk SSSR Ser. Geofiz*, *1*.

Blake, E. S., C. W. Landsea, and E. J. Gibney (2011), The deadliest, costliest, and most intense united states hurricanes from 1851 to 2004, *NOAA Technical Memorandum NWS TPC-4*.

Bleck, R., and D. B. Boudra (1981), Initial Testing of a Numerical Ocean Circulation Model Using a Hybrid (Quasi-Isopycnic) Vertical Coordinate, *J Phys Oceanogr*, *11*(6), 755-770, Doi 10.1175/1520-0485(1981)011<0755:Itoano>2.0.Co;2.

Booij, N., R. C. Ris, and L. H. Holthuijsen (1999), A third-generation wave model for coastal regions - 1. Model description and validation, *J Geophys Res-Oceans*, *104*(C4), 7649-7666, <Go to ISI>://000079784700004.

Bowler, N. E., Arribas, A., Mylne, K. R., Robertson, K. B. and Beare, S. E. (2008), The MOGREPS short-range ensemble prediction system. Q.J.R. Meteorol. Soc., 134: 703–722. doi:10.1002/qj.234

Brown, J. M. (2010), A case study of combined wave and water levels under storm conditions using WAM and SWAN in a shallow water application, *Ocean Model*, *35*(3), 215-229, DOI 10.1016/j.ocemod.2010.07.009.

Caldwell, D. R., and W. P. Elliott (1970), Surface stresses produced by rainfall, *J. Phys. Oceanography*, *1*, 145-148.

Cataneo, R., and G. E. Stout (1968), Raindrop size distribution in humid continental climates, *Journal of Applied Meteorology and Climatology*, *7*, 901-918.

Chan, J. C. L., and R. T. Williams (1987), Analytical and Numerical-Studies of the Beta-Effect in Tropical Cyclone Motion .1. Zero Mean Flow, *Journal of the Atmospheric Sciences*, *44*(9), 1257-1265, Doi 10.1175/1520-0469(1987)044<1257:Aansot>2.0.Co;2.

Chapman, D. C. (1985), Numerical treatment of cross-shelf open boundaries in a barotropic coastal ocean model, *J Phys Oceanogr*, *15*(8), 1060-1075, 10.1175/1520-0485(1985)015<1060:ntocso>2.0.co;2.

Charnock, H. (1955), Wind stress on a water surface. *Quart. J. Roy. Meteor. Soc.,* **81,** 639–640.

Chen, C. S., J. H. Qi, C. Y. Li, R. C. Beardsley, H. C. Lin, R. Walker, and K. Gates (2008), Complexity of the flooding/drying process in an estuarine tidal-creek salt-marsh system: An application of FVCOM, *J Geophys Res-Oceans*, *113*(C7)Artn C07052 Doi 10.1029/2007jc004328.

Chen, S. H., and W. Y. Sun (2002), A one-dimensional time dependent cloud model, *J Meteorol Soc Jpn*, *80*(1), 99-118, Doi 10.2151/Jmsj.80.99.

Chou, M., and a. M. J. Suarez (1994), An efficient thermal infrared radiation parameterization for use in general circulation models, *NASA Tech. Memo.*, *104606*(3), 85pp.

Clayson, C. A., and L. H. Kantha (1999), Turbulent kinetic energy and its dissipation rate in the equatorial mixed layer, *J Phys Oceanogr*, *29*(9), 2146-2166, Doi 10.1175/1520-0485(1999)029<2146:Tkeaid>2.0.Co;2.

Codiga, D. L. (2011), Unified Tidal Analysis and Prediction Using the UTide Matlab Functions, *Technical Report 2011-01 Graduate School of Oceanography, University of Rhode Island, Narragansett, RI. 59pp*

Colling, A. (2001), Ocean Circulation, *Butterworth-Heinemann*, p64.

Collins, S. N., R. S. James, P. Ray, K. Chen, A. Lassman, and J. Brownlee (2013), Grids in Numerical Weather and Climate Models, Climate Change and Regional/Local Responses, 10.5772/5592210.5772/55922.

Cook, G. D., and C. M. A. C. Goyens (2008), The impact of wind on trees in Australian tropical savannas: lessons from Cyclone Monica, *Austral Ecology*, *33*(4), 462-470, DOI 10.1111/j.1442-9993.2008.01901.x.

Cummings, J. A. (2005), Operational multivariate ocean data assimilation, *Q J Roy Meteor Soc*, *131*(613), 3583-3604, 10.1256/qj.05.105.

Davidson N. E. and H. C. Weber (2000), The BMRC High-Resolution Tropical Cyclone Prediction System: TC-LAPS. *Mon. Wea. Rev.*, **128**, 1245–1265. doi: http://dx.doi.org/10.1175/1520-0493(2000)128<1245:TBHRTC>2.0.CO;2

Dean, R. G., and C. J. Bender (2006), Static wave setup with emphasis on damping effects by vegetation and bottom friction, *Coast Eng*, *53*(2-3), 149-156, DOI 10.1016/j.coastaleng.2005.10.005.

Dinniman, M. S., J. M. Klinck, and W. O. Smith (2007), Influence of sea ice cover and icebergs on circulation and water mass formation in a numerical circulation model of the Ross Sea, Antarctica, *J Geophys Res-Oceans*, *112*(C11)Artn C11013 Doi 10.1029/2006jc004036.

Dodla, V. B., S. Desamsetti, and A. Yerramilli (2011), A Comparison of HWRF, ARW and NMM Models in Hurricane Katrina (2005) Simulation, *International Journal of Environmental Research and Public Health*, *8*(6), 2447-2469, DOI 10.3390/ijerph8062447.

Dube, S. K., P. C. Sinha and G. D. Roy (1986), The effect of continuously deforming coastline on the numerical simulation of storm surges in Bangladesh, Math. *Comput. Simul*., 28, 41-56

Dube, S.K., A.D. Rao, P.C. Sinha, T.S. Murty and N. Bahulayan (1997), Storm surge in the Bay of Bengal and Arabian Sea: The problem and its prediction. *Mausam*, 48:283–304

Dudhia, J. (1989), Numerical Study of Convection Observed during the Winter Monsoon Experiment Using a Mesoscale Two-Dimensional Model, *Journal of the Atmospheric Sciences*, *46*(20), 3077-3107, Doi 10.1175/1520-0469(1989)046<3077:Nsocod>2.0.Co;2.

Dudhia, J. (1996), A multi-layer soil temperature model for MM5, *Sixth PSU/NCAR Mesoscale Model Users' Workshop*.

Dunnavan, G. M., and J. W. Diercks (1980), An Analysis of Super Typhoon Tip (October 1979), *Mon Weather Rev*, *108*(11), 1915-1923, Doi 10.1175/1520-0493(1980)108<1915:Aaostt>2.0.Co;2.

Durden, S. L. (2010), Remote Sensing and Modeling of Cyclone Monica near Peak Intensity, *Atmosphere*, *1*(1), 15-33, Doi 10.3390/Atmos1010015.

Dvorak, V. (1984), Tropical cyclone intensity analysis using satellite data. NOAA Tech. Rep. NESDIS11, 47 pp. [Available from NOAA/NESDIS, 5200 Auth Rd., Washington, DC 20233.]

Egbert, G. D., and S. Y. Erofeeva (2002), Efficient inverse Modeling of barotropic ocean tides, *Journal of Atmospheric and Oceanic Technology*, *19*(2), 183-204, 10.1175/1520-0426(2002)019<0183:eimobo>2.0.co;2.

Fairall, C. W., and A. B. White (1994), A ship-based system for direct surface flux and remote boundary-layer measurements over the ocean, in The Air-Sea Interface.

Fairall, C. W., E. F. Bradley, D. P. Rogers, J. B. Edson, and G. S. Young (1996), Bulk parameterization of air-sea fluxes for Tropical Ocean Global Atmosphere Coupled Ocean Atmosphere Response Experiment, *J Geophys Res-Oceans*, *101*(C2), 3747-3764, Doi 10.1029/95jc03205.

Fiore M.E.M., E. E. D'Onofrio, J. L. Pousa, E. J. Schnack, G. R. Bértola (2009), Storm surges and coastal impacts at Mar del Plata, Argentina, *Continental Shelf Research*, Volume 29, Issue 14, Pages 1643-1649, ISSN 0278-4343, http://dx.doi.org/10.1016/j.csr.2009.05.004.

Flather, R. A. (1976), A tidal model of the northwest European continental shelf, in *Mémoires de la Société Royale de Sciences de Liege*, edited, pp. 141-164.

Flowerdew, J., Horsburgh, K., Wilson, C., Mylne, K. (2010), Development and evaluation of an ensemble forecasting system for coastal storm surges, **136**, 1444-1456. *Q. J. R. Meteorol. Soc*. DOI:10.1002/qj.648

Fritz, H. M., C. Blount, R. Sokoloski, J. Singleton, A. Fuggle, B. G. McAdoo, A. Moore, C. Grass, and B. Tate (2007), Hurricane Katrina storm surge distribution and field observations on the Mississippi Barrier Islands, *Estuar Coast Shelf S*, *74*(1-2), 12-20, DOI 10.1016/j.ecss.2007.03.015.

Froude L. S. R., Bengtsson L., Hodges K. I. (2007), The prediction of extratropical storm tracks by the ECMWF and NCEP ensemble prediction systems. *Mon Wea Rev* 135:2545 DOI: 10.1175/MWR3422.1

Gönnert, G., Murty, T., and Siefert, W. (2001), Global Storm Surges: Theory Observation and Application – vol. 63

Griffies, S. M., and R. W. Hallberg (2000), Biharmonic friction with a Smagorinsky-like viscosity for use in large-scale eddy-permitting ocean models, *Mon Weather Rev*, *128*(8), 2935-2946, <Go to ISI>://000088849800004.

Harper B. A., R. J. Sobey and K. P. Stark (1978), Sensitivity analysis of a tropical cyclone surge model. In: *Proceedings of Numerical Simulation of Fluid Motion: International Conference on Numerical Simulation of Fluid Dynamic Systems*,

Melbourne, Australia, 1976 (B.J. Noye, ed.). Monash University, Amsterdam/New York, North-Holland Publishers

Harris, D. L. (1963), Characteristics of the Hurricane Storm Surge, *US Department of Commerce Weather Service Technical Paper No. 48*, *Rockville, MD*.

Henderson-Sellers, A., et al. (1998), Tropical cyclones and global climate change: A post-IPCC assessment, *B Am Meteorol Soc*, *79*(1), 19-38, Doi 10.1175/1520-0477(1998)079<0019:Tcagcc>2.0.Co;2.

Hetland, R. D. (2005), Relating river plume structure to vertical mixing, *J Phys Oceanogr*, *35*(9), 1667-1688, Doi 10.1175/Jpo2774.1.

Hill, K. A., and G. M. Lackmann (2009), Influence of Environmental Humidity on Tropical Cyclone Size, *Mon Weather Rev*, *137*(10), 3294-3315, Doi 10.1175/2009mwr2679.1.

Hofmann, H., A. Lorke, and F. Peeters (2011), Wind and ship wave-induced resuspension in the littoral zone of a large lake, *Water Resources Research*, *47*Artn W09505 Doi 10.1029/2010wr010012.

Hong, S. Y., Y. Noh, and J. Dudhia (2006), A new vertical diffusion package with an explicit treatment of entrainment processes, *Mon Weather Rev*, *134*(9), 2318-2341, Doi 10.1175/Mwr3199.1.

Horsburgh, K., J.W. de Vries, M.P. Etala, T.S. Murty, J.W. Seo, S.K. Dube, I. Lavrenov, M. Holt, P. Daniel, M. Higaki, G. Warren, R. Cabrera, N. Nirupama, D. Paradis and P. Dandin (2011), *WMO publication 1076: Guide to Storm Surge Forecasting*, 2011 edition, Genève, CH, WMO, ISBN 978-92-63-11076-3, 120p.

Hubbert, G.D., L.M. Leslie and M.J. Manton (1990), A storm surge model for the Australian region. *Q. J. R. Meteorol. Soc.*, 116:1005–1020, DOI:10.1002/j.49711649411

Huffman, G. J., R. F. Adler, D. T. Bolvin, G. J. Gu, E. J. Nelkin, K. P. Bowman, Y. Hong, E. F. Stocker, and D. B. Wolff (2007), The TRMM multisatellite precipitation analysis (TMPA): Quasi-global, multiyear, combined-sensor precipitation estimates at fine scales, *Journal of Hydrometeorology*, *8*(1), 38-55, Doi 10.1175/Jhm560.1.

Irish, J. L., D. T. Resio, and J. J. Ratcliff (2008), The influence of storm size on hurricane surge, *J Phys Oceanogr*, *38*(9), 2003-2013, Doi 10.1175/2008jpo3727.1.

Jacob, S. D., and C. J. Koblinsky (2007), Effects of precipitation on the upper-ocean response to a hurricane, *Mon Weather Rev*, *135*(6), 2207-2225, Doi 10.1175/Mwr3366.1.

Jan, C. D., C. M. Tseng, J. S. Wang and Y. H. Cheng (2006), Empirical relation between the typhoon surge deviation and the corresponding typhoon characteristics: a case study in Taiwan, *Journal of Marine Science and Technology*, Vol.11(3), p.193-200

Janjic, Z. I. (1994), The Step-Mountain Eta Coordinate Model - Further Developments of the Convection, Viscous Sublayer, and Turbulence Closure Schemes, *Mon Weather Rev*, *122*(5), 927-945, Doi 10.1175/1520-493(1994)122<0927:Tsmecm>2.0.Co;2.

Jarvinen, B. R., and M. B. Lawrence (1985), An Evaluation of the Slosh Storm-Surge Model, *B Am Meteorol Soc*, *66*(11), 1408-1411, <Go to ISI>://WOS:A1985AWE6700005.

Jones, P. W. (1998), A Users Guide for SCRIP: A Spherical Coordinate Remapping and Interpolation Package. V 1.4, *Los Alamos National Laboratory*, *http://climate.lanl.gov/Software/SCRIP/*

Jordan, C. (1958), Mean soundings for the West Indies area, *Journal of Meteorology*, *15*, 91-97.

Kain, J. S. (2004), The Kain-Fritsch convective parameterization: An update, *Journal of Applied Meteorology*, *43*(1), 170-181, Doi 10.1175/1520-0450(2004)043<0170:Tkcpau>2.0.Co;2.

Kessler, W. S., and S. Cravatte (2013), Mean circulation of the Coral Sea, *J Geophys Res-Oceans*, *118*(12), 6385-6410, Doi 10.1002/2013jc009117.

Kim, S. Y., T. Yasuda, and H. Mase (2010), Wave set-up in the storm surge along open coasts during Typhoon Anita, *Coast Eng*, *57*(7), 631-642, DOI 10.1016/j.coastaleng.2010.02.004.

Knutson, T. R., John L. McBride, Johnny Chan, Kerry Emanuel, Greg Holland, Chris Landsea, Isaac Held, James P. Kossin, A. K. Srivastava, and M. Sugi (2010), Tropical Cyclones and Climate Change, *Nature Geosci 3.3* 10.1038/ngeo779, 157-163, 10.1038/ngeo779.

Kwok, J. H. Y., and J. C. L. Chan (2005), The influence of uniform flow on tropical cyclone intensity change, *Journal of the Atmospheric Sciences*, *62*(9), 3193-3212, Doi 10.1175/Jas3531.1.

Lamb, S. H. (1895), Hydrodynamics, *Cambridge University Press*.

Larson, J., R. Jacob, and E. Ong (2005), The Model Coupling Toolkit: A new fortran90 toolkit for building multiphysics parallel coupled models, *International Journal*

of High Performance Computing Applications, *19*(3), 277-292, Doi 10.1177/1094342005056115.

Lewis, M., Horsburgh, K.J., and Bates, P. (2014), Bay of Bengal cyclone extreme water level estimate uncertainty, *Natural Hazards*, January 2014, doi: 10.1007/s11069-014-1046-2

Li, M., L. J. Zhong, W. C. Boicourt, S. L. Zhang, and D. L. Zhang (2006), Hurricane-induced storm surges, currents and destratification in a semi-enclosed bay, *Geophys Res Lett*, *33*(2)Artn 02604 Doi 10.1029/2005gl024992.

Lin, N., K. A. Emanuel, J. A. Smith, and E. Vanmarcke (2010), Risk assessment of hurricane storm surge for New York City, *Journal of Geophysical Research*, Vol. 115, D18121, doi:10.1029/2009JD013630

Lin, Y. L., R. D. Farley, and H. D. Orville (1983), Bulk Parameterization of the Snow Field in a Cloud Model, *Journal of Climate and Applied Meteorology*, *22*(6), 1065-1092, Doi 10.1175/1520-0450(1983)022<1065:Bpotsf>2.0.Co;2.

Liu, W. T., K. B. Katsaros, and J. A. Businger (1979), Bulk parameterization of air-sea exchanges of heat and water-vapor including the molecular constraints at the interface, *Journal of the Atmospheric Sciences*, *36*(9), 1722-1735, 10.1175/1520-0469(1979)036<1722:bpoase>2.0.co;2.

Marchesiello, P., J. C. McWilliams, and A. F. Shchepetkin (2001), Open boundary conditions for long-term integration of regional ocean models, *Ocean Model*, *3*, 1-20.

Mastenbroek C., G. Burgers, and P. A. E. M. Janssen (1993), The Dynamical Coupling of a Wave Model and a Storm Surge Model through the Atmospheric Boundary

Layer. *J. Phys. Oceanogr.*, **23**, 1856–1866. doi: http://dx.doi.org/10.1175/1520-0485(1993)023<1856:TDCOAW>2.0.CO;2

Marteau, R., Y. Richard, B. Pohl, C. C. Smith, and T. Castel (2015), High-resolution rainfall variability simulated by the WRF RCM: application to eastern France, *Clim Dynam*, *44*(3-4), 1093-1107, DOI 10.1007/s00382-014-2125-5.

Mlawer, E. J., S. J. Taubman, P. D. Brown, M. J. Iacono, and S. A. Clough (1997), Radiative transfer for inhomogeneous atmospheres: RRTM, a validated correlated-k model for the longwave, *Journal of Geophysical Research-Atmospheres*, *102*(D14), 16663-16682, Doi 10.1029/97jd00237.

Monin, A. S., and A. M. Obukhov (1954), Basic laws of turbulent mixing in the surface layer of the atmosphere. *Tr. Geofiz. Inst., Akad. Navk SSSR,* **24,** 163–187.

Moon I.-J,, I. Ginis, T. Hara, H. Tolman, C. W. Wright, and E. J. Walsh (2003), Numerical simulation of sea surface directional wave spectra under hurricane wind forcing. *J. Phys. Oceanogr.,* **33,** 1680–1706.

Moon I.-J, T. Hara, I. Ginis, S. E. Belcher, and H. Tolman, (2004), Effect of surface waves on air–sea momentum exchange. Part II: Behavior of Drag Coefficient under Tropical Cyclones. *J. Atmos. Sci.,* **61,** 2334–2348

Murty, T.S., R.A. Flather and R.F. Henry (1986), The storm surge problem in the Bay of Bengal. *Prog. Oceanogr.*, 16:195–233.

Olander, T. L., and C. S. Velden (2007), The advanced Dvorak technique: Continued development of an objective scheme to estimate tropical cyclone intensity using

geostationary infrared satellite imagery, *Weather Forecast*, *22*(2), 287-298, Doi 10.1175/Waf975.1.

Orlanski, I. (1976), A simple boundary condition for unbounded hyperbolic flows, *Journal of Computational Physics*, *21*(3), 251-269.

Parker, J. A., and D. Foden (2009), High-resolution Measurement of a North Sea Storm Surge, *J Coastal Res*, <Go to ISI>://WOS:000266722400153, 1656-1660.

Paulson, C. A. (1970), The mathematical representation of wind speed and temperature profiles in the unstable atmospheric surface layer, *J. Appl. Meteor.*, *9*, 857–861.

Peng, M. C., L. Xie, and L. J. Pietrafesa (2004), A numerical study of storm surge and inundation in the Croatan-Albemarle-Pamlico Estuary System, *Estuar Coast Shelf S*, *59*(1), 121-137, DOI 10.1016/j.ecss.2003.07.010.

Peng, M. C., L. Xie, and L. J. Pietrafesa (2006), Tropical cyclone induced asymmetry of sea level surge and fall and its presentation in a storm surge model with parametric wind fields, *Ocean Model*, *14*(1-2), 81-101, DOI 10.1016/j.ocemod.2006.03.004.

Ponte, R. M. (2006), Oceanic response to surface loading effects neglected in volume-conserving models, *J Phys Oceanogr*, *36*(3), 426-434, Doi 10.1175/Jpo2843.1.

Pousa, J. L., E. E. D' Onofrio, M. M. E. Fiore, and E. E. Kruse (2013), Environmental impacts and simultaneity of positive and negative storm surges on the coast of the Province of Buenos Aires, Argentina, *Environmental Earth Sciences*, *68*(8), 2325-2335, DOI 10.1007/s12665-012-1911-9.

Pugh, D. T. (1987), *Tides, surges and mean sea-level*, John Wiley and Sons, Chichester.

Raymond, W. H., and H. L. Kuo (1984), A radiation boundary-condition for multi-dimensional flows, *Q J Roy Meteor Soc*, *110*(464), 535-551, 10.1002/qj.49711046414.

Rego, J. L., and C. Y. Li (2010), Storm surge propagation in Galveston Bay during Hurricane Ike, *J Marine Syst*, *82*(4), 265-279, DOI 10.1016/j.jmarsys.2010.06.001.

Resio, D. T., and J. J. Westerink (2008), Modeling the physics of storm surges, *Physics Today*, *61*(9), 33-38, Doi 10.1063/1.2982120.

Robertson, I. N., H. R. Riggs, S. C. S. Yim, and Y. L. Young (2007), Lessons from Hurricane Katrina storm surge on bridges and buildings, *J Waterw Port C-Asce*, *133*(6), 463-483, Doi 10.1061/(Asce)0733-950x(2007)133:6(463).

Roden, G. I., and H. T. Rossby (1999), Early Swedish contribution to oceanography: Nils Gissler (1715-71) and the inverted barometer effect, *B Am Meteorol Soc*, *80*(4), 675-682, Doi 10.1175/1520-0477(1999)080<0675:Escton>2.0.Co;2.

Rodi, W. (1987), Examples of Calculation Methods for Flow and Mixing in Stratified Fluids, *J Geophys Res-Oceans*, *92*(C5), 5305-5328, Doi 10.1029/Jc092ic05p05305.

Rogers, E., T. B. , B. F. , Y. L. , D. P. , and a. G. D. (2001), National Oceanic and Atmospheric Administration Changes to the NCEP Meso Eta Analysis and Forecast System: Increase in resolution, new cloud microphysics, modified precipitation assimilation, modified 3DVAR analysis, *NOAA*.

Rotunno, R., and K. A. Emanuel (1987), An Air-Sea Interaction Theory for Tropical Cyclones .2. Evolutionary Study Using a Nonhydrostatic Axisymmetrical Numerical-Model, *Journal of the Atmospheric Sciences*, *44*(3), 542-561, Doi 10.1175/1520-0469(1987)044<0542:Aaitft>2.0.Co;2.

Saha, S., et al. (2010), The Ncep Climate Forecast System Reanalysis, *B Am Meteorol Soc*, *91*(8), 1015-1057, Doi 10.1175/2010bams3001.1.

Schiller, R. V., V. H. Kourafalou, P. Hogan, and N. D. Walker (2011), The dynamics of the Mississippi River plume: Impact of topography, wind and offshore forcing on the fate of plume waters, *J Geophys Res-Oceans*, *116*10.1029/2010jc006883.

Seeliger U., B. Kjerfve (2001), *Coastal Marine Ecosystems of Latin America*, Springer, ISBN: 9783662044827, 9783642086571, doi: 10.1007/978-3-662-04482-7

Shchepetkin, A. F., and J. C. McWilliams (2005), The regional oceanic modeling system (ROMS): a split-explicit, free-surface, topography-following-coordinate oceanic model, *Ocean Model*, *9*(4), 347-404, DOI 10.1016/j.ocemod.2004.08.002.

Sheng, Y. P., V. Alymov, and V. A. Paramygin (2010), Simulation of storm surge, wave, currents, and inundation in the Outer Banks and Chesapeake Bay during Hurricane Isabel in 2003: The importance of waves, *J Geophys Res-Oceans*, *115*Artn C04008 Doi 10.1029/2009jc005402.

Skamarock, W. C., J. B. Klemp, J. Dudhia, D. O. Gill, D. M. Baker, M. G. Duda, H. XYu., W. W., and P. JG. (2008), A Description of the Advanced Research WRF Version 3. , *NCAR/TN-475+STR*.

Smith, W. H. F., and Sandwell D. T. (1997), Global seafloor topography from satellite altimetry and ship depth soundings, *Science*, *277*, 1957-1962.

Smolarkiewicz, P. K. (1983), A Simple Positive Definite Advection Scheme with Small Implicit Diffusion, *Mon Weather Rev*, *111*(3), 479-486, Doi 10.1175/1520-0493(1983)111<0479:Aspdas>2.0.Co;2.

Stewart, R. H. (2009), Introduction to Physical Oceanography, *University Press of Florida*.

Tablazon, J., et al. (2015), Probabilistic storm surge inundation maps for Metro Manila based on Philippine public storm warning signals, *Nat Hazard Earth Sys*, *15*(3), 557-570, DOI 10.5194/nhess-15-557-2015.

Umlauf, L., and H. Burchard (2003), A generic length-scale equation for geophysical turbulence models, *Journal of Marine Research*, *61*(2), 235-265, 10.1357/002224003322005087.

Van Dorn, W. G. (1953), Wind stress on an artificial pond, *Journal of marine research*, *12*, 249-276.

van Heerden, I., G. Kemp, and H. Mashriqui (2007), Use of the ADCIRC Storm Surge Model for Hurricane Katrina Surge Predictions and Levee Forensic Studies. Embankments, Dams, and Slopes, *GeoDenver*, (doi: 10.1061/40905(224)12), 1-9.

Wang, S. Y., R. McGrath, J. Hanafin, P. Lynch, T. Semmler, and P. Nolan (2008), The impact of climate change on storm surges over Irish waters, *Ocean Model*, *25*(1-2), 83-94, DOI 10.1016/j.ocemod.2008.06.009.

Warner, J. C., W. R. Geyer, and J. A. Lerczak (2005), Numerical modeling of an estuary: A comprehensive skill assessment, *J Geophys Res-Oceans*, *110*(C5)Artn C05001, Doi 10.1029/2004jc002691.

Warner, J. C., B. Armstrong, R. Y. He, and J. B. Zambon (2010), Development of a Coupled Ocean-Atmosphere-Wave-Sediment Transport (COAWST) Modeling System, *Ocean Model*, *35*(3), 230-244, DOI 10.1016/j.ocemod.2010.07.010.

Warner, J. C., C. R. Sherwood, R. P. Signell, C. K. Harris, and H. G. Arango (2008), Development of a three-dimensional, regional, coupled wave, current, and

sediment-transport model, *Computers & Geosciences*, *34*(10), 1284-1306, DOI 10.1016/j.cageo.2008.02.012.

Watson, P. J. (2011), Is There Evidence Yet of Acceleration in Mean Sea Level Rise around Mainland Australia?, *J Coastal Res*, *27*(2), 368-377, Doi 10.2112/Jcoastres-D-10-00141.1.

Weisberg, R. H., and L. Y. Zheng (2006), Hurricane storm surge simulations for Tampa Bay, *Estuar Coast*, *29*(6A), 899-913, <Go to ISI>://WOS:000244009800004.

Westerink, J. J., R. A. Luettich, A. M. Baptista, N. W. Scheffner, and P. Farrar (1992), Tide and Storm-Surge Predictions Using Finite-Element Model, *Journal of Hydraulic Engineering-Asce*, *118*(10), 1373-1390, Doi 10.1061/(Asce)0733-9429(1992)118:10(1373).

Westerink, J. J., R. A. Luettich, J. C. Feyen, J. H. Atkinson, C. Dawson, H. J. Roberts, M. D. Powell, J. P. Dunion, E. J. Kubatko, and H. Pourtaheri (2008), A basin- to channel-scale unstructured grid hurricane storm surge model applied to southern Louisiana, *Mon Weather Rev*, *136*(3), 833-864, Doi 10.1175/2007mwr1946.1.

Wijesekera, H. W., C. A. Paulson, and E. D. Skyllingstad (2003), Modeling the evolution of a fresh sea surface anomaly produced by tropical rainfall, *J Geophys Res-Oceans*, *108*(C11)Artn 3338, Doi 10.1029/2002jc001408.

Wilcox, D. C. (1988), Reassessment of the scaling-determining equation for advanced turbulence models, *AIAA Journal*, *26*, 1299–1310.

Wu, C. C. (2013), TYPHOON MORAKOT Key Findings from the Journal TAO for Improving Prediction of Extreme Rains at Landfall, *B Am Meteorol Soc*, *94*(2), 155-160, Doi 10.1175/Bams-D-11-00155.1.

Zachry, B. C., W. J. Booth, J. R. Rhome, and T. M. Sharon (2015), A National View of Storm Surge Risk and Inundation, *Weather Clim Soc*, *7*(2), 109-117, Doi 10.1175/Wcas-D-14-00049.1.

Zhong, L. J., M. Li, and D. L. Zhang (2010), How do uncertainties in hurricane model forecasts affect storm surge predictions in a semi-enclosed bay?, *Estuar Coast Shelf S*, *90*(2), 61-72, DOI 10.1016/j.ecss.2010.07.001.